



**UNIVERSITY OF WEST BOHEMIA IN PLZEŇ**  
**FACULTY OF MECHANICAL ENGINEERING**  
**DEPARTMENT OF MATERIALS SCIENCE AND TECHNOLOGY**

**A dissertation**

**by**

**Saleem Ayaz Khan**

**submitted in partial fulfillment of the requirements for the degree of**

**Doctor of Philosophy**

**Doctoral study programme P 2301**

**Study programme details: Materials Engineering and Engineering  
Metallurgy**

**Electronic structure calculations as an aid to study  
structure and magnetism of layered materials**

**Supervisor: RNDr. Ondřej Šipr, CSc.**



*Dedicated*  
*to*  
*my family*

for their endless love, support and encouragement

A special dedication to  
my late grandfather

and . . .

To whom it may concern



# DECLARATION

I hereby declare that the work which is being presented in the thesis entitled **Electronic structure calculations as an aid to study structure and magnetism of layered materials** in partial fulfillment of the requirements for the award of the degree of DOCTOR OF PHILOSOPHY submitted to the Faculty of Mechanical Engineering, University of West Bohemia, Pilsen, is an authentic record of my own work under the supervision of **RNDr. Ondřej Šipr, CSc.** I have not submitted the matter embodied in this thesis for the award of any other degree or diploma of the university or any other institute.

9<sup>th</sup> September, 2016

**Saleem Ayaz Khan**



# Abstract

Magnetism is an important phenomena that plays a significant role in our daily life through its numerous technological applications. In this thesis we focus our attention on features which are important for one specific area of applications, namely, the memory technology. We investigate these features on the case of FePt — a layered material with potential applications in next generation ultrahigh-density perpendicular magnetic recording media.

Two aspects of FePt magnetism have a specific role in its technological applications. These are (i) magnetocrystalline anisotropy and (ii) influence of disorder on magnetic properties. Theoretical modelling can provide an insight into related processes and phenomena that can be used for more efficient targeting of the experimental and technological research aimed at exploiting and amending properties of this material. For this purpose, we employed quantum-mechanical calculations of electronic and magnetic properties based on the density functional theory (DFT). To get accurate and reliable results, we used two different computational methods: the full-potential linearized augmented plane wave (FLAPW) method and the full-potential Korringa-Kohn-Rostoker (KKR) Green function method.

Magnetocrystalline anisotropy (MCA) is a crucial property for applications of magnetic materials in design of computer memories. A good material for data storage technology (such as read-and-write heads) should possess a large MCA energy. Evaluating the MCA energy consists in determining the total energies for two magnetization directions and subtracting them. The mechanism behind the MCA is the spin-orbit coupling (SOC), i.e., a coupling between the spin of the electron and its orbital motion. This is a relativistic effect.

Quantum-mechanical MCA energy calculations are very sensitive and challenging. The reason for this is that the total energy and the MCA energy can differ by about eight or nine orders of magnitude, which means that one has to achieve a very high accuracy of the calculations. The values of the MCA energy of FePt obtained by us via both methods (FLAPW and KKR) are in a good agreement with each other. As the calculated MCA energy significantly differs from experiment, it is clear that many-body effects beyond the local density approximation to the DFT are essential in this regard.

We found that it is not really important whether relativistic effects for FePt are accounted for by solving the fully relativistic Dirac equation or whether the SOC is treated as a correction to the solution of the (scalar-relativistic) Schrödinger equation. From our analysis of the dependence of the MCA energy on the magnetization angle and on the SOC strength it follows that the main mechanism of the MCA in FePt can be described by accounting for the SOC within second order perturbation theory. However, a distinct contribution to the MCA not accountable for by second

order perturbation theory is present as well.

In real materials there is always some disorder present. This gets important especially at high temperatures. Presence of disorder influences the properties of materials — sometimes, very significantly. To gain insight into how the disorder affects especially the magnetic properties of FePt and related systems, we investigated the local aspects of magnetism of disordered FePt. We employed and compared two approaches of accounting for disorder in quantum mechanical calculations of materials properties. The first approach is the supercell technique: the disorder is simulated by considering a larger (super)cell in which the atoms occur in many different local environments. The second approach we used simulates the disorder by introducing an effective medium, i.e., it is a mean-field approach. A mean-field technique widely used in studying substitutionally disordered systems is the coherent potential approximation (CPA).

The focus of our research on disordered FePt was on the trends of the spin and orbital magnetic moments with chemical composition of the nearest neighbourhood and with the bond lengths around the Fe and Pt atoms. Small but distinct difference between average magnetic moments obtained when using the supercells and when relying on the the CPA is identified in this thesis. We are able to link this difference to the neglect of the Madelung potential in the CPA.

One of measures of short range order effects in alloys is disorder-induced broadening of core levels binding energies. A multitude of local environments leads to coexistence of several core levels of the same type. Corresponding x-ray photoelectron spectroscopy core level widths in alloys are thus larger than in single-element systems. We evaluated the disorder-induced broadening of core levels and found that this broadening is practically the same for all deep core levels. This indicates that the broadening is dominated by local variations of the Madelung potential.



# Abstrakt

Magnetismus je důležitý jev, který hraje v našich životech významnou roli prostřednictvím mnoha technologických aplikací. V této dizertaci soustředíme pozornost na vlastnosti, které jsou důležité pro aplikace v jedné konkrétní oblasti, a to počítačových pamětí. Tyto vlastnosti budeme zkoumat na případě FePt, což je vrstevnatý materiál s potenciálními aplikacemi v oblasti vysokohustotního kolmého magnetického zaznamování.

V technologických aplikacích FePt hrají zvláštní roli dva aspekty magnetismu. Jednak je to magnetokrystalická anizotropie, jednak je to neuspořádanost a její vliv na magnetické vlastnosti. Teoretické modelování může poskytnout vhled do souvisejících procesů a jevů tak, aby bylo možné lépe zacílit experimentální a technologický výzkum směřující k využívání a ovlivňování vlastností tohoto materiálu. Pro tento účel jsme využili kvantově-mechanické výpočty elektronických a magnetických vlastností opírající se o teorii funkcionálu hustoty (DFT). Abychom získali přesné a spolehlivé výsledky, využili jsme dvou výpočetních metod: linearizovanou metodu napojených vln v úplném potenciálu (FLAPW) a metodu Korringy, Kohna a Rostokera využívající Greenovy funkce v úplném potenciálu (KKR).

Magnetokrystalická anizotropie (MCA) je klíčovou vlastností z hlediska aplikací v oblasti počítačových pamětí. Materiál vhodný pro technologické použití v oblasti uchovávání dat (jako např. pro čtecí a zapisovací hlavy) by měl mít velkou MCA energii. Výpočet MCA energie spočívá ve výpočtu totálních energií pro dva různé směry magnetizace a v jejich vzájemném odečtení. Mechanismem způsobujícím MCA je spin-orbitální vazba (SOC), jež spočívá v interakci mezi spinem elektronu a jeho orbitálním pohybem. Jedná se o relativistický jev.

Kvantově-mechanické výpočty MCA energie jsou velmi citlivé a náročné. Důvodem pro to je, že totální energie a MCA energie se navzájem liší o osm až devět řádů, z čehož vyplývá nutnost provést výpočty skutečně s vysokou přesností. Hodnoty MCA energie, které jsme získali za použití obou metod (FLAPW a KKR) jsou navzájem v dobré shodě. Jelikož vypočtená hodnota MCA energie pro FePt se významně liší od hodnoty experimentální, je zřejmé, že významnou roli zde hrají mnohačasticové jevy, které již nelze v rámci DFT popsat pomocí aproximace lokální hustoty.

Zjistili jsme, že v případě FePt není důležité, zda jsou relativistické efekty započteny řešením plně relativistické Diracovy rovnice nebo zda je SOC vazba pojata jako korekce k řešení (skalárně-relativistické) Schrödingerovy rovnice. Z naší analýzy závislosti MCA energie na úhlu magnetizace a na síle SOC vazby vyplývá, že mechanismus MCA u FePt může být v zásadě popsán tím, že se SOC vazba započte v rámci druhého řádu poruchové teorie. Nicméně existuje malý leč dobře identifikovatelný příspěvek k MCA, který tímto způsobem popsat nelze.

Reálné materiály vždy obsahují určitou neuspořádanost. Její význam vzrůstá při vysokých teplotách. Přítomnost neuspořádanosti ovlivňuje vlastnosti materiálů, a to někdy velmi podstatně. Abychom získali vhled do toho, jak neuspořádanost ovlivňuje zejména magnetické vlastnosti FePt a příbuzných systémů, studovali jsme lokální aspekty magnetismu neuspořádaného FePt. Použili a porovnali jsme dva přístupy jak zahrnout neuspořádanost do kvantově-mechanických výpočtů vlastností materiálů. Za prvé je to supercelová metoda: neuspořádanost je simulována pomocí velké supercely, v níž se atomy vyskytují v mnoha různých lokálních konfiguracích. Za druhé je to metoda středního pole, kdy je zavedeno efektivní médium. Metodou tohoto typu, která je hojně využívána při studiu substitučních slitin, je aproximace koherentním potenciálem (CPA).

Při studiu neuspořádaného FePt jsme kladli důraz na to, jak spinové a orbitální magnetické momenty závisí na chemickém složení nejbližšího okolí a na vzdálenostech mezi Fe a Pt atomy. Zjistili jsme malý leč dobře patrný rozdíl mezi hodnotami průměrných magnetických momentů obdržených pomocí metody supercel a pomocí CPA. Tento rozdíl můžeme přiřadit tomu, že v CPA výpočtech je ignorován Madelungův příspěvek k potenciálu.

Jedním ze způsobů jak kvantifikovat vliv lokálního uspořádání na vlastnosti slitin je analyzovat rozšíření vnitřních hladin vlivem neuspořádanosti. Koexistence mnoha různých lokálních konfigurací totiž vede ke koexistenci vícera vnitřních hladin. Šířka odpovídajících spektroskopických čar je tudíž větší pro atomy ve slitinách než pro atomy v čistých kovech. Spočetli jsme toto rozšíření spektrálních čar pro neuspořádané FePt. Zjistili jsme, že toto rozšíření je prakticky stejné pro všechny vnitřní hladiny. To ukazuje, že rozšíření čar vlivem neuspořádanosti je zapříčiněno především lokálními fluktuacemi Madelungova potenciálu.

# Acknowledgments

First and above all, I praise Allah almighty to provide me this opportunity and grant me the capability to proceed successfully.

To complete PhD degree has been a life-changing experience for me and it was not possible to do without the support and guidance that I received from many people.

My deep gratitude goes to Dr. Ondřej Šipr who expertly guided me during my PhD study. His unwavering enthusiasm for physics keeps me constantly engaged with my research and allows me to grow as a research scientist. His advice on both research and on my career is invaluable.

Many thanks also to Dr. Jan Minár for support, guidance and encouragement he gave me, during my study.

I greatly appreciate the support received through the collaborative work undertaken with the group of Prof. Peter Blaha in Institute of Materials Chemistry, TU Vienna (Austria) and Prof Hubert Ebert in Universität München, Department Chemie (Germany).

I acknowledge the CENTEM project (CZ.1.05/2.1.00/03.0088), CENTEM PLUS (LO1402) and New Technologies Research Centre (NTC), University of West Bohemia for providing financial support to pursue my doctoral studies. I would like to thank administrative staff members of the NTC who have been kind enough to advise and help in their respective roles.

I would like to express my sincere thanks to Martin Šafránek (IT) for generously sharing his time and knowledge for technical assistance in our work.

I would like to express my special thanks to Prof. Dr. Ifikhar Ahmad (my M Phil supervisor) for being a great person and source of motivation. He always encouraged me during my study.

A special thanks to my family. Words can't express how grateful I am to my mother, father, brothers and sisters for all the sacrifices that they have made on my behalf. Their prayer for me was what sustained me thus far. I would also like to thank to my fiancée for her support and encouragement.

I would also like to say a heartfelt thanks to my friends Dr. Sikander Azam, Wilayat Khan, Dr. Anees Ahmad, Dr. Bin Amin, Dr. Gulam Murtaza, Abid-ur-Rahman, Ibrar Hussain and Asifullah for their motivation and inspiration in this challenging period.

Last but not least I would like to thank my beloved father, who always encouraged me to be a scientist and patiently waited for my long journey and to my dear uncle Habibullah Khan who supports me in all aspects of my life.

# Contents

<b>1</b>	<b>Introduction</b>	<b>1</b>
1.1	Magnetic Materials for Data Storage . . . . .	2
1.1.1	Magnetism of solids . . . . .	2
1.2	The magnetocrystalline anisotropy . . . . .	4
<b>2</b>	<b>Materials we are interested in</b>	<b>7</b>
2.1	Ordered FePt . . . . .	7
2.2	Disordered FePt alloys . . . . .	8
<b>3</b>	<b>Computational Methodology</b>	<b>9</b>
3.1	Many Body Problem . . . . .	9
3.2	Density Functional Theory . . . . .	10
3.2.1	Hohenberg and Kohn theorems . . . . .	10
3.2.2	The Kohn-Sham equations . . . . .	10
3.2.3	Local-density approximation (LDA) . . . . .	13
3.2.4	Local spin density approximation (LSDA) . . . . .	13
3.2.5	Generalized Gradient Approximations (GGA) . . . . .	14
3.3	The Dirac Kohn-Sham Equations and spin orbit interaction . . . . .	15
3.4	The Full-Potential Linearized Augmented-Plane Wave Technique . . . . .	17
3.4.1	WIEN2k code . . . . .	18
3.5	The Green function method of Korringa, Kohn and Rostoker . . . . .	19
3.5.1	SPRKKR -package . . . . .	21
3.6	Treatment of disordered system in supercell approach . . . . .	22
3.7	Treatment of disordered system in effective medium approach . . . . .	22
3.7.1	Virtual crystal approximation . . . . .	23
3.7.2	Average t-matrix approximation . . . . .	23
3.7.3	Coherent potential approximation . . . . .	23
3.8	Calculation of magnetocrystalline anisotropy energy . . . . .	24
3.8.1	Calculation of MCA energy . . . . .	24

<b>4</b>	<b>Motivation, earlier works, aim of this thesis</b>	<b>26</b>
4.1	Ordered FePt: MCA energy . . . . .	27
4.2	Disordered FePt: local environment effect . . . . .	28
<b>5</b>	<b>Computational details</b>	<b>31</b>
<b>6</b>	<b>Results and discussion</b>	<b>34</b>
6.1	Magnetocrystalline anisotropy of FePt . . . . .	34
6.1.1	Influence of relativity on magnetic moments and density of states . . . . .	35
6.1.2	MCA energy evaluated by different ways . . . . .	36
6.1.3	Dependence of the total energy on the orientation of the magnetization axis . . . . .	40
6.1.4	Scaling of the MCA energy with spin orbit coupling strength . . . . .	42
6.1.5	Dependence of the MCA energy on the LDA exchange-correlation functional . . . . .	45
6.2	Disordered FePt: Local environment effects . . . . .	47
6.2.1	Average magnetic moments: comparison between supercell and CPA approach . . . . .	48
6.2.2	Dependence of local magnetic moments on the chemical composition of nearest neighbourhood . . . . .	48
6.2.3	Influence of the Madelung potential . . . . .	54
6.2.4	Dependence of local magnetic moments on bond lengths . . . . .	58
6.2.5	Density of states . . . . .	59
6.2.6	Broadening of the core level energies due to disorder . . . . .	62
<b>7</b>	<b>Conclusions</b>	<b>65</b>
<b>A</b>	<b>Convergence tests</b>	<b>67</b>
A.1	Convergence of SPRKKR calculations with $\ell_{\max}^{(\text{KKR})}$ . . . . .	68
A.2	Convergence of WIEN2k calculations with $R_{\text{MT}}K_{\max}$ . . . . .	69
A.3	Stability of WIEN2k calculations with respect to $R_{\text{MT}}$ variations . . . . .	69
A.4	Convergence of SPRKKR and WIEN2k calculations with the number of <b>k</b> -points . . . . .	70
A.5	Convergence of WIEN2k calculations with $E_{\max}$ . . . . .	72
<b>B</b>	<b>Curriculum vitae</b>	<b>85</b>
<b>C</b>	<b>List of publications</b>	<b>88</b>

# List of Figures

1.1	Areal density growth curve of stored informations since the first commercialization [6]. . . . .	3
1.2	Bit areal density progress in magnetic hard disk drives. [7]. . . . .	3
1.3	Magnetization curves of a single HCP Co crystal measured in different directions [8]. . . . .	5
1.4	(a) Magnetic dipole-dipole interaction of the single magnetic moments (b) Spin-orbit coupling [11]. . . . .	6
3.1	Scheme for achieving a self-consistent solution of Kohn-Sham equation	12
3.2	Left figure: Partitioning of unit cell into two parts; spherical atomic region with gist of (I) and the space among atoms called interstitial region shown as (II). Right figure: Actual self-consistent effective potential as obtained from an FLAPW calculation[33]. . . . .	17
3.3	Contour integration of the Green function [45]. . . . .	21
3.4	Schematic digram of the CPA condition for a binary alloy. The label "A" and "B" are occupied by impurity potentials. . . . .	24
6.1	Relation between tP2 cell and tP4 cell for the L1 <sub>0</sub> -phases . . . . .	34
6.2	Partial spin-resolved density of states for Fe and Pt sites calculated within a non-relativistic, a scalar-relativistic and a fully-relativistic framework. . . . .	37
6.3	Dependence of the total energy on the magnetization angle $\theta$ (circles) and its fit either as $K_1 \sin^2 \theta$ (dashed line) or as $K_1 \sin^2 \theta + K_2 \sin^4 \theta$ (dash-dotted line). An overall view is in the left panel, a detailed view on the region close to $\theta=90^\circ$ is in the right panel. . . . .	41
6.4	Dependence of $E_{\text{MCA}}$ on the SOC scaling factor $\lambda$ . . . . .	43
6.5	Dependence of $E_{\text{MCA}}$ on the SOC scaling factor at the Fe sites $\lambda^{(\text{Fe})}$ . . . . .	44
6.6	Dependence of $E_{\text{MCA}}$ on the SOC scaling factor at the Pt sites $\lambda^{(\text{Pt})}$ . . . . .	45
6.7	Packing structure of SQS- $N$ . . . . .	47

6.8	Spin and orbital magnetic moments for Fe sites in various SQS's shown as functions of the number of Fe atoms in their first coordination spheres. The CPA results are shown for comparison. The data were obtained via the SPRKKR code. . . . .	50
6.9	As Fig. 6.8 but for Pt sites. . . . .	50
6.10	Electronic charge for Fe sites in various SQS's shown as a function of the number of Fe atoms in their first coordination spheres. The CPA result is shown for comparison. The data were obtained via the SPRKKR code. . . . .	51
6.11	Spin magnetic moment for Fe sites in various SQS's shown as functions of the charge. The CPA result is shown for comparison. The data were obtained via the SPRKKR code. . . . .	54
6.12	Charge at Fe and Pt sites as function of $N_{\text{Fe}}$ for SQS-4, 8, 16 and 32 obtained with the Madelung potential either included or ignored. The result obtained within the CPA is also shown. These calculations were done by SPRKKR within the full potential mode. . . . .	55
6.13	As figure 6.12 but within the ASA. . . . .	55
6.14	spin magnetic moments at Fe and Pt sites as function of $N_{\text{Fe}}$ for SQS-4, 8, 16 and 32 obtained with the Madelung potential either included or ignored. The result obtained within the CPA is also shown. These calculations were done by SPRKKR within the full potential mode. . . . .	56
6.15	As figure 6.14 but within the ASA. . . . .	56
6.16	Optimized interatomic distances for the first coordination shell in SQS-4, 8, 16, and 32. Average values are shown by horizontal lines. Results were obtained via WIEN2k with the exchange-correlation potential parametrized within the LDA (left panel) and within the GGA (right panel). . . . .	58
6.17	Change of the spin magnetic moment $\Delta\mu_{spin}$ for an Fe atom (left graph) and for a Pt atom (right graph) plotted as a function of change of the average bond length $\Delta\bar{d}_{\text{Fe-Fe}}$ or $\Delta\bar{d}_{\text{Pt-Fe}}$ . The calculations were done by WIEN2k. . . . .	59
6.18	Spin-polarised density of states for Fe and Pt sites. The DOS for supercells was averaged over all sites of the SQS-4, over all sites of the SQS-4 and SQS-8, over all sites of the SQS-4, SQS-8 and SQS-16 and over all sites of the SQS-4, SQS-8, SQS-16 and SQS-32. The CPA results are shown for comparison. The calculations were performed by the SPRKKR. . . . .	60
6.19	Local spin-resolved DOS for inequivalent Fe and Pt sites in SQS-4, 8, and 16. More detailed specification of the inequivalent sites is given in table 6.6. . . . .	61

# List of Tables

6.1	Spin magnetic moments (in $\mu_B$ ) related either to a FePt unit cell or just to the Fe site, for different ways of including the relativistic effects. . . . .	35
6.2	Orbital magnetic moments (in $\mu_B$ ) related to the Fe and Pt atoms in FePt for magnetization either parallel to the $z$ axis ( $\mu_{\text{orb}}^{(\mathbf{M}  z)}$ ) or perpendicular to the $z$ axis ( $\mu_{\text{orb}}^{(\mathbf{M}  x)}$ ). . . . .	35
6.3	MCA energy $E_{\text{max}}$ of FePt (in meV) calculated by three different approaches. . . . .	38
6.4	The MCA energy of FePt (in meV) calculated by subtracting total energies for different exchange and correlation functionals. . . . .	46
6.5	Average spin and orbital magnetic moments (in $\mu_B$ per formula unit) for Fe and Pt atoms in two ordered FePt systems and in four SQS's simulating disordered FePt alloy. Average values over all sites in all SQS's are also shown. The CPA results are presented at the bottom. The data were obtained using the SPRKKR code. . . . .	49
6.6	Local $\mu_{\text{spin}}$ and $\mu_{\text{orb}}$ for inequivalent sites in SQS-(4,8,16) systems. The number of nearest Fe atoms and the multiplicity (how many times the site occurs in appropriate SQS) are also shown for each site. These results were obtained for non-relaxed structures using SPRKKR . L1 <sub>0</sub> structure with the $c/a$ ratio modified so that an fcc geometry is obtained. . . . .	52
6.7	As table 6.6 but in SQS-32 system. . . . .	53
6.8	Comparison of spin magnetic moment (in $\mu_B$ ) and charge Q (in electron) obtain by averaging over supercell with CPA result. The upper part of the table contains ASA and lower part contains full potential results. . . . .	57
6.9	Core level widths (in eV) of Fe SQS-N in K-M3 Levels. . . . .	63
6.10	Core level widths (in eV) of Pt SQS-N in K-M3 Levels. . . . .	64
A.1	Convergence of $E_{\text{MCA}}$ obtained via the SPRKKR code with the angular momentum cutoff $\ell_{\text{max}}^{(\text{KKR})}$ . $E_{\text{MCA}}$ was evaluated by subtracting total energies. . . . .	68



A.2	Convergence of $E_{MCA}$ obtained via the WIEN2k code with $R_{MT}K_{max}$ . $E_{MCA}$ was evaluated by means of the magnetic force theorem. . . . .	69
A.3	Dependence of $E_{MCA}$ obtained via the WIEN2k code on muffin-tin radii $R_{MT}$ . $E_{MCA}$ was evaluated by subtracting total energies. . . . .	70
A.4	Convergence of $E_{MCA}$ calculated by the SPRKKR and WIEN2k codes with the number of $\mathbf{k}$ -points in the full BZ. $E_{MCA}$ (in meV) was evaluated by subtracting total energies. . . . .	71
A.5	Convergence of $E_{MCA}$ obtained via the WIEN2k code with $E_{max}$ . $E_{MCA}$ was evaluated either by subtracting total energies (the second column) or by means of the magnetic force theorem (the third column). . . . .	72

# Chapter 1

## Introduction

The theoretical prediction of crystal structure and properties are very important for getting information on its structure stability, electronic structure, spectroscopic and magnetic properties. There are many program packages which calculate these properties via ab initio calculations. Many physical properties of the material are determined from the electronic structure. The electronic structure can be investigated by ab initio calculations, that means starting from fundamental quantum theory. The input data in the form of structural information is employed and the calculations are performed within the framework of the density functional theory in which the complex many-body interaction of all electrons is replaced by an equivalent but simpler problem of a single electron moving in an effective potential [1, 2, 3]. These calculations are typically performed for zero temperature (0 K), but the obtained results establish the basis for understanding the finite-temperature properties as well [4].

Magnetism is a very interesting and dynamic field. Current society uses many applications based on this phenomena. The areas of its application are broad. It ranges from power generation to communication, transportation, security, information storage and many other aspects of our day-to-day life. For example electric motors and generators are made from the combination of electromagnet and a permanent magnet: a generator converts mechanical energy into electric energy by moving a conductor through a magnetic field. The electromagnet in cathode ray tube is used to guide electrons to the screen of televisions and computer monitors. Magnetic strip is also used in credit, debit, and automatic teller machine (ATM) cards. High field superconducting magnets provide the magnetic field in magnetic resonance imaging (MRI) devices that are now used extensively in hospitals and medical centers.

Another area of applications of magnetism include magnetic recording and storage devices in computers, and in audio and video systems. Magnetic storage devices

work on the principle of two stable magnetic states represented by the 0 and 1 in the binary number system. Floppy disks have dozens of tracks on which data can be digitally written in or stored by means of a write-head and then accessed or read by means of a read-head. A write-head provides a strong local magnetic field to the region through which the storage track of the disk is passed. The read-head senses stray magnetic flux from the storage track of the disk as it passes over the head. Another example of digital magnetic storage and reading is the magnetic strip on the back of plastic debit and credit cards. The magnetic strip contains identification data which can be accessed through, for example, an ATM. In this thesis we deal with specific aspects of the memory technology.

In recent years, the growth in the subsequent data storage requirements and production of digital data have grown considerably (as demonstrated by the graph in Fig. 1.1). In 2002, up to 92.0 percent of all latest digital information was stored on magnetic media [5]. New technologies have been introduced by the data storage industry to meet growing demands for greater than ever data volumes. Recordable CDs and DVDs, digital video tapes and high volume solid state flash memories are competent to store digital data of high quality. Hard disks permit novel data storage techniques that were not obtainable, presenting at the same time new challenges in research world. The magnetic hard disk drive (HDD) is a keynote component in computer (PC). Although new technology has made other data storage devices possible, magnetic recording is still dominating among the data storage devices due to fast speed and high recording density. Today, the HDD industries ability to increase recording density is important because the requirements of large storage capacity of HDD continue to grow in the consumer electronics markets. However, continued growth in recording density not only challenges implementing new recording techniques to reduce the bit size on the disk surface but also requires application of advanced materials for reading and writing information. Since the magnetic properties of the recording media are strongly influenced by various features of their microstructure, optimization of the magnetic properties through understanding structure-property relations is of importance for developing high-density recording media.

## 1.1 Magnetic Materials for Data Storage

### 1.1.1 Magnetism of solids

Magnetism in solids originates from electrons in atom. The electron exhibits spin and as well as orbital motion. Electrons in most of the atoms exist in pairs. The magnetic moment associated with spin and orbital motion of a single electron in Hydrogen

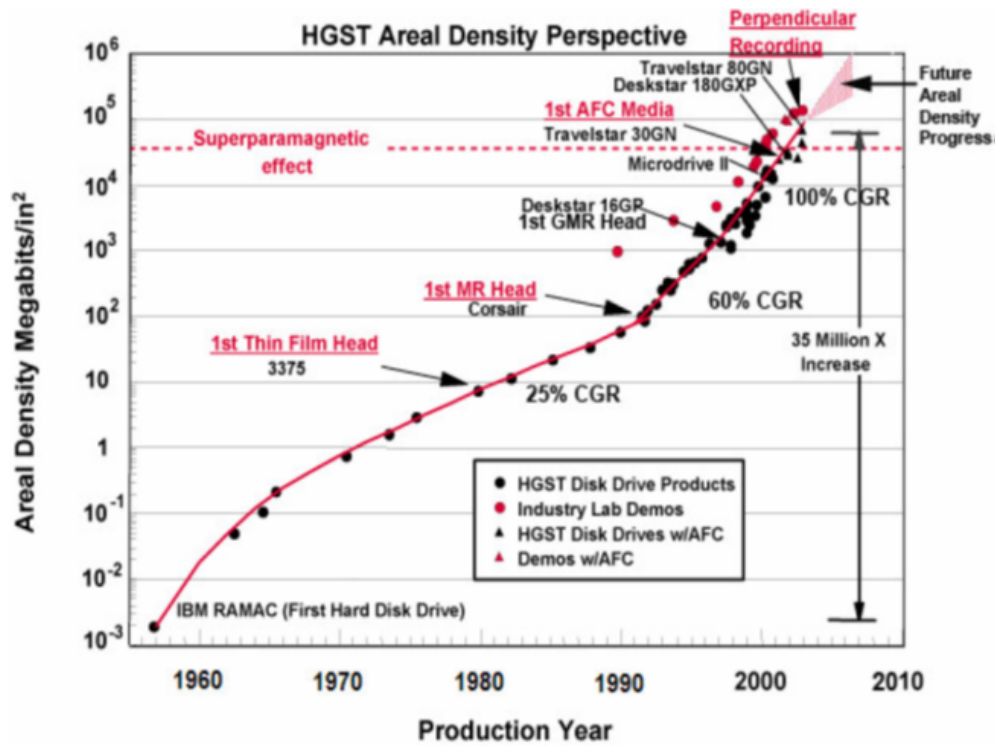


Figure 1.1: Areal density growth curve of stored informations since the first commercialization [6].

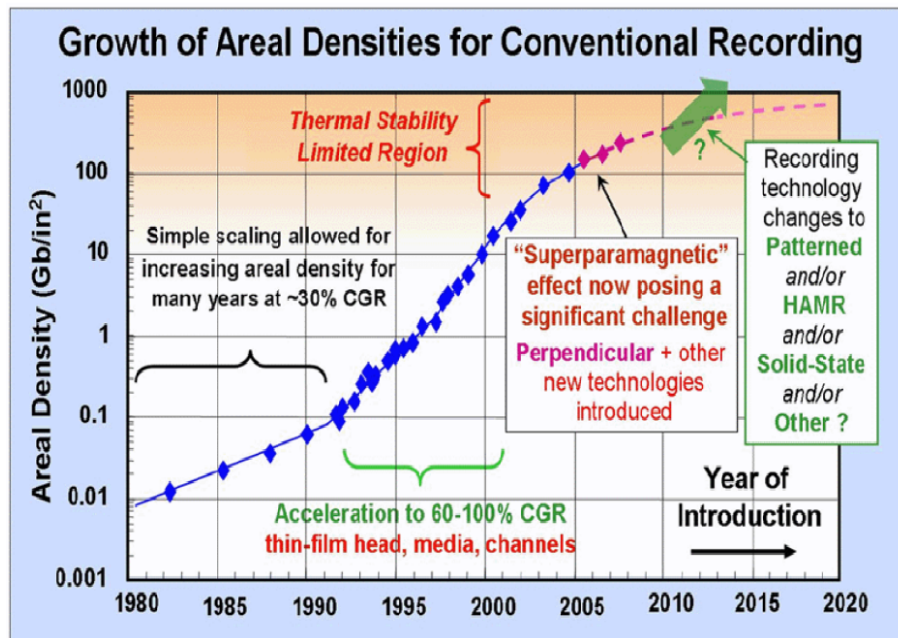


Figure 1.2: Bit areal density progress in magnetic hard disk drives. [7].

(H) atom is known as Bohr magneton, which can be considered as standard unit of magnetic moment of solids. According to Pauli exclusion principle only two electrons can occupy one orbit, spinning in an opposite direction. So in most of the cases the magnetic moments due to spin motion cancel the effect of each other and show no contribution to magnetic moment of a solid. In most of the transition elements the d-orbitals are not fully occupied. Likewise, in rare earth elements the f-orbitals are also not fully occupied. According to the Hund's rule, the spin magnetic moment is originated from electrons in partially occupied orbitals. Isolated atoms are usually magnetic due to Hund's rule. In solids magnetic order appears only for some systems, typically either containing 3d atoms Fe, Co, Ni or containing rare earth elements.

As discussed above that magnetism is caused by the spin of electrons and their orbital motion about their nuclei. Due to different electronic structures, materials can have different responses to an external applied magnetic field and thereby can be generally classified as diamagnetic, paramagnetic, ferromagnetic (FM) and anti-ferromagnetic (AFM) materials. Among these, ferromagnetic materials are the most important for data storage due to their unique magnetic properties. As compared to other magnetic materials, ferromagnetic materials have a large positive magnetic susceptibility. With such large susceptibilities, these materials can be easily magnetized. This is because FM materials atomic level show long-range spin ordering, cause the unpaired electron spins to be lined up parallel with each other in a region called magnetic domain. Normally, these magnetic domains are randomly oriented with respect to one another at room temperature, resulting in no magnetism shown in the bulk materials. However, once exposed to a magnetic field, FM materials can be easily magnetized by lining up the magnetic domains to the applied field. In addition, FM materials tend to maintain their initial magnetization to some extent after the external field is removed. This extraordinary property of maintaining the magnetic states has enabled a variety of applications of FM materials in magnetic data storage. Usually, Fe, Co, Ni and some of their alloys are FM materials since then spins of the unpaired 3d electrons prefer to be aligned in the same direction by the magnetic exchange effect. Presently most of the magnetic recording components, such as the writing heads are composed of these materials.

## 1.2 The magnetocrystalline anisotropy

Many magnetic materials generally show different magnetic properties when an external field is applied in different directions. If the internal energy of the material depends on the magnetization direction with respect to the crystallographic axis, the material is said to have magnetic anisotropy. There are many different types

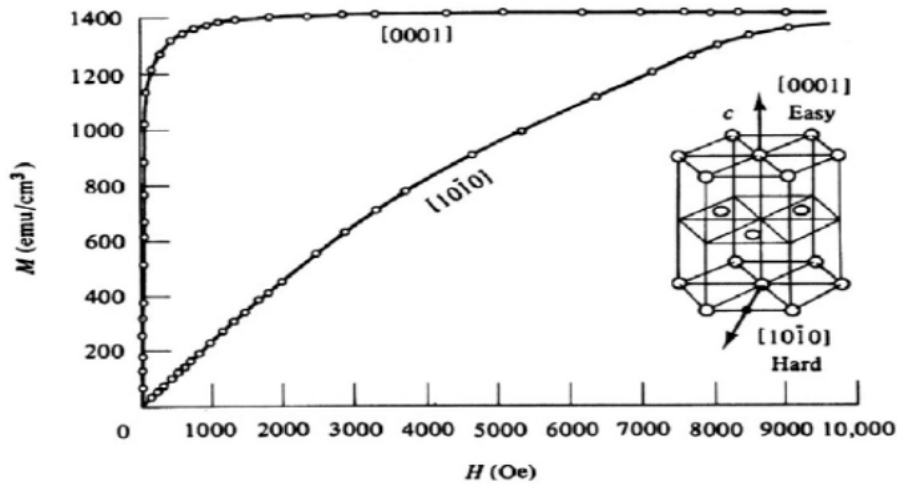


Figure 1.3: Magnetization curves of a single HCP Co crystal measured in different directions [8].

of anisotropy which are related to the crystal structure, the residual stress and the grain shape. Among all these types of anisotropy, only the crystal anisotropy, which is generally called magnetocrystalline anisotropy (MCA), is intrinsic property of the material. The MCA is found to be practically important in the design of magnetic recording media. By measuring the magnetization curves of a material along different crystallographic directions, one can easily observe the MCA. For example cobalt (Co), which is commonly used in magnetic recording media and has a hexagonal closed packed (HCP) structure, the magnetization curves in Fig. 1.3 shows that the magnetic saturation can be easily achieved by applying a small field in the  $[0001]$  direction while in the  $[1010]$  direction, a large field is required. Therefore, the magnetic easy axis of HCP Co is the  $c$ -axis, in which less energy is required to line up the magnetic moments. In the material which has MCA, the magnetization vector tends to point along the direction of the easy axis when there is no external magnetic field. Against the anisotropy force, an applied field must do work to deflect the magnetization from the easy axis. Therefore, when the magnetization points to a non-easy direction, there must be energy stored in the crystal [8]. This stored energy is called MCA energy. MCA energy is much larger for layered and low dimensional materials than for the bulk systems. One part of the magnetic anisotropy energy is in its spin-orbit coupling (SOC). Generally one can obtain the SOC induced part through relativistic ab initio calculations using spin density functional theory.

Another important part of the magnetic anisotropy comes from magnetic dipole-dipole interaction of the individual magnetic moments and thus depends on the shape of the magnetic sample as shown in Fig. 1.4. The shape dependent anisotropy is caused by Breit interaction [9, 10] between individual electrons. The dipolar interaction or shape anisotropy can be calculated usually using classical electromagnetic

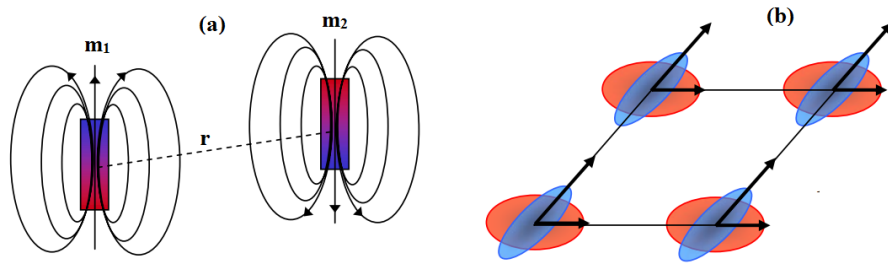


Figure 1.4: (a) Magnetic dipole-dipole interaction of the single magnetic moments  
 (b) Spin-orbit coupling [11].

(Maxwell) theory.

$$E_{dip} = \frac{1}{4\pi} \left[ \frac{\mathbf{m}_1 \cdot \mathbf{m}_2}{r^2} - 3 \frac{(\mathbf{m}_1 \cdot \mathbf{r})(\mathbf{m}_2 \cdot \mathbf{r})}{r^5} \right], \quad (1.1)$$

where  $\mathbf{m}_1$  and  $\mathbf{m}_2$  are dipolar magnetic moments and  $r$  is distance between them. In the present work we don't deal with it. We will not deal shape anisotropy in this thesis. It can be treated classically, its analysis does not require quantum mechanical calculations.

# Chapter 2

## Materials we are interested in

In recent decade the layered materials got considerable attention on scientific and technological point of view. These materials play main role in energy conversion and storage, CO<sub>2</sub> capture and conversion, catalysis, biomass, wastewater treatment, air pollution control, optoelectronic, magneto electronic devices chemical sensors etc. This class of materials are also used as precursors for novel multifunctional materials. In the present work we are interested in FePt layered materials.

The FePt system is one of the robust contestant for an efficient material for recording data. Therefore it is necessary to study this system in detail. In order to understand the microscopic origin of its magnetic properties, it is necessary to study the hybridization of 3d-5d states and role of interface in FePt magnetic system.

In 3d-5d systems, the large magnetic moments of the 3d electrons are intermixed with large spin-orbit interaction ( $\zeta$ ) of the 5d electrons. The spin-orbit interaction of Pt 5d is about one order of magnitude higher ( $\zeta_{Pt} = 712$  meV) in comparison to Fe 3d element ( $\zeta_{Fe} = 65$  meV) [12]. This leads to increase of the magnetic anisotropy of the system [11]. The situation concerning the dependence of magnetic anisotropy on orbital moment of the 3d electrons is also very important and needs to be studied in more elaborated way.

### 2.1 Ordered FePt

High anisotropic magnetic materials are in demand in the field of information technologies. Another important application for this class of materials are permanent magnet or bias layer for spin electronic devices [13]. The ordered FePt (bulk-L1<sub>0</sub>) has large MCA energy of  $7 \times 10^7$  ergs/cm<sup>3</sup>. Therefore it is a suitable candidate for next generation ultrahigh-density perpendicular magnetic recording media [14].



The high-temperature stable phase of FePt are face-centered tetragonal (fct or L1<sub>0</sub>) ordered phase and face-centered cubic (fcc or A1) disordered phase [15].

## 2.2 Disordered FePt alloys

The importance of the disordered compounds can't be ignored in fundamental science and technological applications. Many exclusive properties of solid-state materials appear only in a disordered phase. Some important components the disordered state of the materials are local atomic impurities, substitutions and vacancies which are responsible for unique properties in semiconductors, high temperature superconductors, ceramics, zeolite catalysts, metallic alloys and many other materials that are technologically important [16]. The crystal structure of ordered FePt fcc (A1) have lattice parameter of  $a=3.807 \text{ \AA}$ [17].

# Chapter 3

## Computational Methodology

Computational materials science and material engineering based on ab initio (first principle) calculations has become a substantial partner to experiment. The link between applied engineering and theoretical research has been made and is now an important motivation for researchers developing new computational methodologies. Engineers are using these capabilities to solve technological problems [18]. One of the most important example of computational methodology is the pioneering first principles or ab initio calculations. Ab initio methods are based on quantum mechanics.

For simple single particle systems, the Schrödinger equation can be solved analytically (as for hydrogen atom). However it is not possible to solve Schrödinger equation analytically for many electron system. To overcome is difficulty certain finite basis sets are used to represent the electronic wavefunction which transform the Schrödinger equation into an algebraic equation. Then the algebraic equation can be solved using numerical methods. This transformation includes two classes of approximations. First we reduce many body electron system to one-electron system, then we solve the basis set for a single electron system.

### 3.1 Many Body Problem

State of the system in quantum mechanics is described by the wave function. The wave function provides full information about the state of the system. Schrödinger equation can be solved for single body problem. However this task becomes more difficult when the number of the particles contained in a system is large and the problem transforms from a simpler one particle to the many body complex one. Owing to their large number, the corresponding number of degree of freedom or di-

mensions increase rapidly, and it becomes difficult to describe the related mechanics of the system by solving the Schrödinger equation for the wave function.

## 3.2 Density Functional Theory

A remarkable achievement in development of DFT was made by Hohenberg and Kohn in 1964. Solution of Schrödinger equation for many electron systems and complex system can be obtained by treating many-electron wave function as functional of electron density containing only three variables, instead of  $3N$  variables ( $N$  stands for number of electrons, each electron has 3 spatial variables). It is easier to deal with the complex system in this way instead of using large number of  $3N$  variables which is too much difficult. This transformation introduce exchange correlation potential which is not known exactly and has to be approximated.

### 3.2.1 Hohenberg and Kohn theorems

**Theorem I:** For any system of interacting particles in an external potential  $V_{\text{ext}}(\mathbf{r})$ , the potential  $V_{\text{ext}}(\mathbf{r})$  is determined uniquely, except for a constant, by the ground state particle density  $n_0(\mathbf{r})$ . Since  $n_0(\mathbf{r})$  determines the number of electrons in the system, it follows that  $n_0(\mathbf{r})$  also determines the ground state wavefunctions and all other electronic properties.

**Theorem II:** An Universal functional for energy  $E[n]$  in terms of the density  $n(\mathbf{r})$  can be defined, valid for any external potential  $V_{\text{ext}}(\mathbf{r})$ . For any particular  $V_{\text{ext}}(\mathbf{r})$ , the exact ground state energy of the system is the global minimum value of this functional, and the density  $n(\mathbf{r})$  that minimizes the functional is the exact ground state density  $n_0(\mathbf{r})$ .

The first theorem states that the ground state energy is a functional of electron density. The second theorem states that ground state energy can be obtained to minimize energy of the system according to the electron density. Both Hohenberg-Kohn theorems establish the one-to-one mapping between the potential and density. The potential determines the wave function and there is one to one correspondence between the density and wave function. However Hohenberg-Kohn theorems don't give a practical guide how to do the calculations.

### 3.2.2 The Kohn-Sham equations

The Kohn-Sham method is a formulation of DFT that introduces a set of eigen value equation within the framework of DFT. As mentioned above, DFT tries to

transform problem of finding many body wave function  $\psi_0(\mathbf{r}_1\mathbf{r}_2, \dots, \mathbf{r}_N)$  into a problem of finding the electron density  $n(\mathbf{r})$ . In that way we have only 3 variables instead of  $3N$  variables. This is achieved via the Hohenberg-Kohn theorms [1]. The total energy  $E$  of the system with charge density  $n(\mathbf{r})$  can be expressed as:

$$E(n) = T(n) + \int V_{\text{ext}}(\mathbf{r}) n(\mathbf{r}) d\mathbf{r} + V_H[n] + E_{\text{xc}}[n]. \quad (3.1)$$

$$V_H = \frac{e^2}{2} \int \frac{n(\mathbf{r}) n(\mathbf{r}')}{|\mathbf{r} - \mathbf{r}'|} d\mathbf{r} d\mathbf{r}', \quad (3.2)$$

where  $V_H$  is the Hartree columbic potential energy part and  $E_{\text{xc}}$  is the exchange and correlation energy. The straightforward application of this formula has two barriers: First, the exchange-correlation energy  $E_{\text{xc}}$  is not known precisely and second, the kinetic term must be expressed in terms of the charge density. As was first suggested by Kohn and Sham, the charge density  $n(\mathbf{r})$  can be written as the sum of the squares of a set of orthonormal wave functions  $\phi_i(\mathbf{r})$ :

$$n(\mathbf{r}) = \sum_i^N |\phi_i(\mathbf{r})|^2. \quad (3.3)$$

Equation (3.3) represents the solution to the Schrödinger equation for  $N$  non-interacting electrons moving in an effective potential  $V_{\text{eff}}(\mathbf{r})$

$$\left[ -\frac{\hbar^2}{2m} \nabla_i^2 + V_{\text{eff}}(\mathbf{r}_i) \right] \phi_i(\mathbf{r}) = E_i \phi_i(\mathbf{r}), \quad (3.4)$$

where the effective potential is defined as

$$V_{\text{eff}}(\mathbf{r}) = V_{\text{ext}}(\mathbf{r}) + e^2 \int \frac{n(\mathbf{r}')}{|\mathbf{r} - \mathbf{r}'|} d\mathbf{r}' + \frac{\delta E_{\text{xc}}[n]}{\delta n}. \quad (3.5)$$

These three equations form the Kohn-Sham equations in their standard form. This system is then solved iteratively, until self-consistency between  $V_{\text{eff}}(\mathbf{r})$  and  $n(\mathbf{r})$  is approached. Note that the eigen values  $E_i$  have no physical meaning, only the total sum, which matches the energy of the entire system  $E$  through the equation [3]:

$$E = \sum_i^N E_i - V_H[n] + E_{\text{xc}}[n] - \int \frac{\delta E_{\text{xc}}[n]}{\delta n(\mathbf{r})} n(\mathbf{r}) d\mathbf{r}. \quad (3.6)$$

The equation above portrays the schematic representation of the self consistent iterative loop for the solution of the Kohn-Sham equations.

Practically, there are several distinct ways in which Kohn-Sham theory can be applied on the system under examination. In the density functional solid state computations, local-density approximation to the exchange correlation (XC) energy is still frequently used. The detail about local-density approximation is found in Sec 3.2.3.

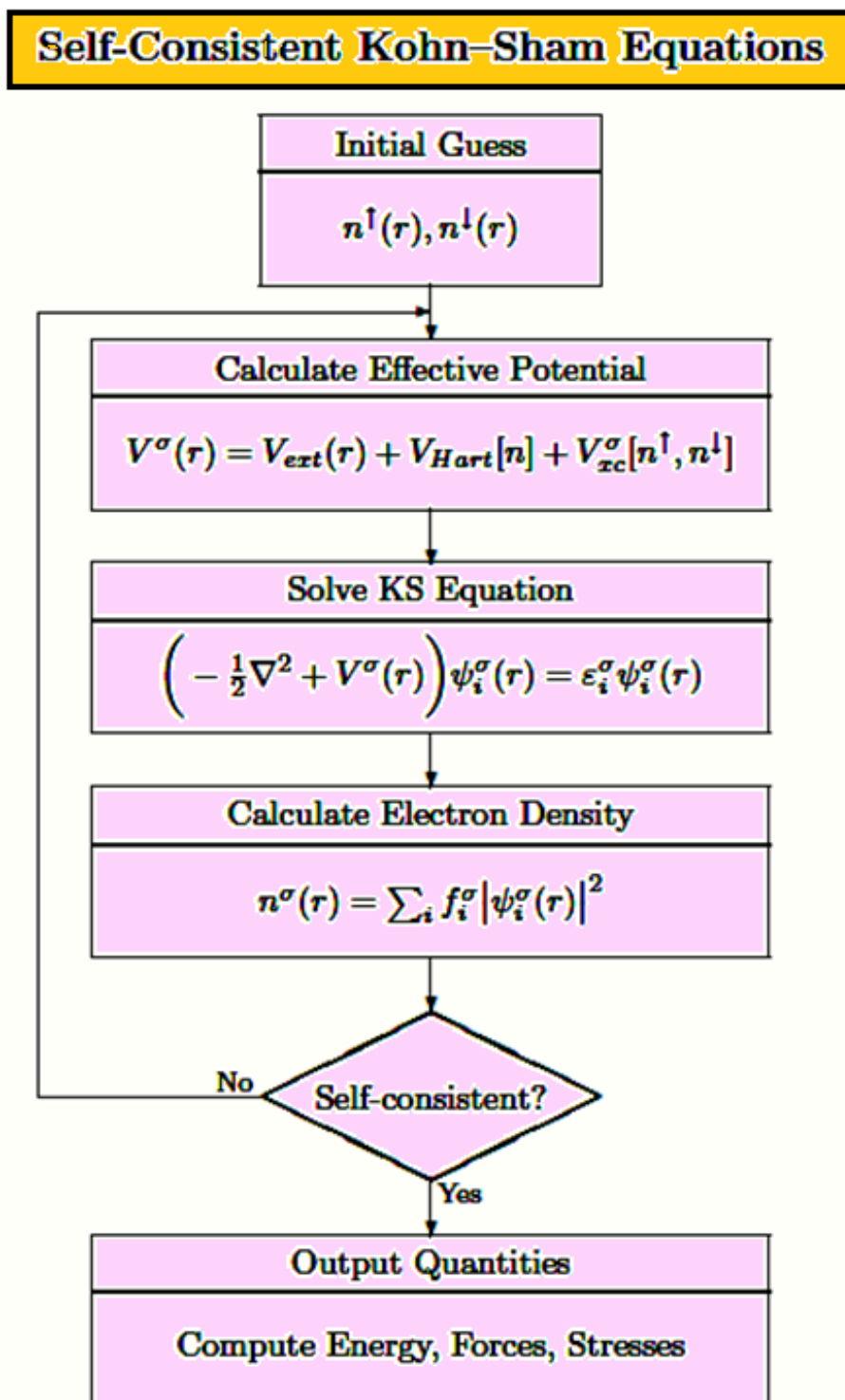


Figure 3.1: Scheme for achieving a self-consistent solution of Kohn-Sham equation

### 3.2.3 Local-density approximation (LDA)

In this approximation we imagine that the whole interacting and inhomogeneous particle system is a set of large number of boxes, with each having homogeneous and interacting electronic gas. In simple words the approximated energy correction in local-density approximation (LDA) is represented as exchange correlation energy  $E_{xc}(r)$  of the homogeneous electron system. This significantly simplifies the solution, requiring less computational capabilities in comparison to formal individual electron wave functions with large number of dimensions. Of course, that is possible only if the exchange-correlation term can be portrayed as local-density functional. The mathematical expression may be seen as a sum of the all contribution from each of the boxes

$$E_{xc}[n(\mathbf{r})] = \int \epsilon_{xc}[n(\mathbf{r})]n(\mathbf{r})dr, \quad (3.7)$$

so that the exchange and correlation potential shapes as

$$\mu_{xc}(\mathbf{r}) = \frac{\delta[n(\mathbf{r})\epsilon_{xc}[n(\mathbf{r})]]}{\delta n(\mathbf{r})}. \quad (3.8)$$

$$\epsilon_{xc}[n(\mathbf{r})] = \epsilon_{xc}^{homo}[n(\mathbf{r})], \quad (3.9)$$

where  $\epsilon_{xc}^{homo}$  represents exchange-correlation energy per particle of a homogeneous electronic system. On theoretical aspect, for useful calculations such data can be parameterized. For this purpose number of parameterizations exists, where the Perdew and Zunger [19] approach may be the most commonly used parameterization. In this parameterization, Perdew and Zunger use Monte-Carlo calculations of Ceperley and Alder [20] for various densities of a homogeneous electron system. This parameterization uses interpolation-schemes to track these precise outcomes for the exchange-correlation energy functional at various electrons densities. LDA, although a rough approximation, has proven to be a surprisingly fruitful in a sense that properties like structure, phase stability, vibrational frequencies and elastic nature are rendered reliable for many samples.

### 3.2.4 Local spin density approximation (LSDA)

The spin flavor of the usual local density approximation (LSDA) has been the basis to the electronic-structure calculations in solid-state physics and chemistry for many years. For spin polarized calculation equation (3.7) can be written as

$$E_{xc}^{LSD}(n_{\uparrow}, n_{\downarrow}) = \int d^3r n(\mathbf{r})\epsilon_{xc}^{homo}[n_{\uparrow}(\mathbf{r}), n_{\downarrow}(\mathbf{r})], \quad (3.10)$$

where  $n_{\uparrow}(\mathbf{r}), n_{\downarrow}(\mathbf{r})$  are the spin densities of many body system,  $\epsilon_{xc}^{homo}(n_{\uparrow}, n_{\downarrow})$  represents the exchange and correlation energy for each entity of the homogeneous electron system.

In this thesis we used various LSDA for the correlation functionals, including

- Vosko and Wilk and Nusair [21].
- Perdew and Wang [22].
- von Barth and Hedin [23].
- Moruzzi, Janak and Williams [24].

### 3.2.5 Generalized Gradient Approximations (GGA)

The LSDA was found to be a tool with reasonable accuracy in many of the solid state targets, it's level is adequate. However, it fails in many chemical applications that need high precision in determining the energies with substantial accuracy. This decreased the interest of quantum-chemist community towards DFT until a new scheme has been suggested [21]. This new scheme uses also called gradient of density and expressed the energy functional as

$$E_{xc}^{GGA}[n_{\uparrow}, n_{\downarrow}] = \int d^3r f(n_{\uparrow}(\mathbf{r}), n_{\downarrow}(\mathbf{r}), \nabla n_{\uparrow}, \nabla n_{\downarrow}), \quad (3.11)$$

These functionals has divided into two categories, functionals that are constructed from the homogeneous electron gas and semi empirical functionals [25]. The generalized gradient approximation (GGA) has attracted much attention for its abstract simplicity and moderate computational workloads. At present it is grasping an increasing attention as an improvement of the LDA [26]. The improvement of GGA over the usual LDA consist mainly the following points:

1. *Prediction of more precise binding energies in molecules and solids, correcting the trend of the LDA to over binding* [27].
2. *GGA significantly improves the cohesive energies and lattice parameters and screening properties. On the other hand it decrease the energies of the corresponding atoms in comparison to LDA* [28].
3. *The correct equilibrium volume with calculated by GGA significantly improve the accuracy of the elastic properties* [29].

In bulk, the crystal structural qualities don't get improved by the GGA. Generally, lattice parameters obtained via GGA are always larger in comparison to LDA. Improved agreement with experimental measurements is registered in case of alkali-metals, 3d-metals, and some 4d-metals. However, for 5d-metals along with some common semiconductors, overestimation of lattice parameters up to some percents

has been reported by GGA [30], The LDA slightly underestimates the lattice parameters of the 5d-metals. The smaller binding energy and larger bond length of the GGA in comparison to LDA is due to the fact that GGA favors inhomogeneity in density. Finally it is concluded that LDA is better for systems with slowly varying density and GGA is good for inhomogeneous systems such as isolated atoms and molecules.

Hence choice of the approximation depends on the nature of the material selected and the property that needs to be calculated. For metallic system such as FePt one uses LDA. On the other hand LDA overestimate the magnetocrystalline anisotropy therefore GGA is also used to check whether one can overcome this difficulty or not.

### 3.3 The Dirac Kohn-Sham Equations and spin-orbit interaction

Spin-orbit coupling is the interaction of the electron spin with its own orbital motion. It manifests itself in lifting the degeneracy of one-electron energy levels in atoms, molecules, and solids. In solid-state physics, the nonrelativistic Schrödinger equation is frequently used as a first approximation, e.g. in electron band-structure calculations. Without relativistic corrections, it leads to doubly-degenerated bands, spin-up and spin-down, which can be split by a spin-dependent term in the Hamiltonian. In this approach, spin-orbit interaction can be included as a relativistic correction to the Schrödinger equation. For this purpose one has to consider the Dirac equation, which is the basic equation for electronic systems, including the electron spin and its relativistic behavior. One obtains the Dirac equation by linearizing the relativistic generalization of the Schrödinger equation. It is Lorentz-invariant and describes the electron spin and spin-orbit coupling from first principles.

It is essential for heavy atoms to include the relativistic effect. Instead of the ordinary Schrödinger equation, the Dirac Kohn-Sham equations are used for the appropriate description of relativistic effects in the materials possessing the heavy ions. Here we illustrate different approximations to the full Dirac KS scheme, its consequences and eliminating a few of the approximations. In several books, we can find the Dirac equation applications for electronic structure of atoms. We will follow the analysis of J. Kubler and V. Eyert [31, 32].

Dirac Hamiltonian can be written as (energies are measured relative to the rest energy):

$$H_D = c\boldsymbol{\alpha}\mathbf{p} + (\beta - 1)mc^2 + V(\mathbf{r}), \quad (3.12)$$

where  $\boldsymbol{\alpha}$  and  $\beta$  are the 4x4 matrices:



$$\boldsymbol{\alpha} = \begin{pmatrix} 0 & \boldsymbol{\sigma} \\ \boldsymbol{\sigma} & 0 \end{pmatrix}, \quad \boldsymbol{\beta} = \begin{pmatrix} I & 0 \\ 0 & -I \end{pmatrix}, \quad I = \begin{pmatrix} 1 & 0 \\ 0 & 1 \end{pmatrix}, \quad (3.13)$$

where  $\boldsymbol{\sigma}$  denotes the Pauli-spin matrices. Eigenvectors of (3.12) are four-component functions which are written in terms of two-component functions as  $\phi$  and  $\chi$ :

$$\psi_n = \begin{pmatrix} \psi_1 \\ \psi_2 \\ \psi_3 \\ \psi_4 \end{pmatrix} = \begin{pmatrix} \phi \\ \chi \end{pmatrix}, \quad (3.14)$$

Here the time independent two component spinors  $\phi$  and  $\chi$  describe the Spatial and spin degrees of freedom, leads to set of couple of equations

$$c(\boldsymbol{\alpha}\mathbf{p})\chi = (E - V)\phi. \quad (3.15)$$

$$c(\boldsymbol{\alpha}\mathbf{p})\phi = (E - V + 2mc^2)\chi. \quad (3.16)$$

These equations lead to differential equation for  $\phi$  which resolve the relativistic effects in an approximative way:

$$\left[ \left(1 - \frac{E-V}{2mc^2}\right) \frac{p^2}{2m} + V \right] \phi - \frac{\hbar^2}{4m^2c^2} (\boldsymbol{\nabla}V\boldsymbol{\nabla}\phi) + \frac{\hbar^2}{4m^2c^2} (\boldsymbol{\sigma}[\boldsymbol{\nabla}V \times \mathbf{p}]\phi) = E\phi. \quad (3.17)$$

Radial equations promptly illustrate the difference in the relativistic treatments. Presuming the spherically symmetric potential, the Eq. (3.17) becomes

$$\left[ \frac{p^2}{2m} + V - \frac{p^4}{8m^2c^2} - \frac{p^2}{8m^2c^2} \frac{dV}{dr} \frac{\partial}{\partial \mathbf{r}} + \frac{1}{2m^2c^2} \frac{1}{r} \frac{dV(\mathbf{r})}{dr} (\mathbf{l}\mathbf{s}) \right] \phi = E\phi. \quad (3.18)$$

In the above Eq. (3.18) the first two terms on the left side are represent non relativistic Schrödinger equation, the third and forth terms on the left sides are called the mass and Darwin correction while, the fifth term shows the spin-orbit coupling. One can write the last term in elaborated way

$$H_{SO} = \frac{1}{r} \frac{dV(\mathbf{r})}{dr} (\boldsymbol{\sigma} \cdot (\mathbf{r} \times \mathbf{p})) = \frac{1}{r} \frac{dV(\mathbf{r})}{dr} (\boldsymbol{\sigma} \cdot \mathbf{L}) = \zeta(\mathbf{r})(\boldsymbol{\sigma} \cdot \mathbf{L}). \quad (3.19)$$

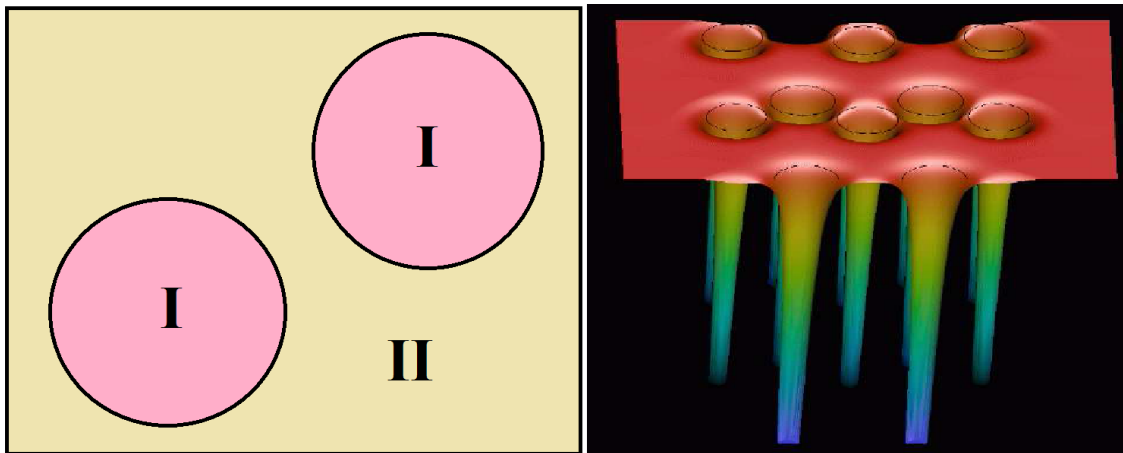


Figure 3.2: Left figure: Partitioning of unit cell into two parts; spherical atomic region with gist of (I) and the space among atoms called interstitial region shown as (II). Right figure: Actual self-consistent effective potential as obtained from an FLAPW calculation[33].

## 3.4 The Full-Potential Linearized Augmented-Plane Wave Technique

The full potential linearized augmented-plane wave (FLAPW) technique is now accepted as a tool that allows us to do the most precise ab initio calculation. The FLAPW method is an all-electron algorithm which is universally appropriate to all atoms of the periodic table, in particular to rare-earths, transition metals and multi-atomic systems with compact as well as open structures. Because of all-electron nature of this method, magnetism is included carefully and one can calculate electronic-structure and magnetic character of variety of bulk crystals, surfaces and nanosystems more accurately.

The FLAPW technique is a process for solving the Kohn Sham equations. It provides the total energy and energy bands of the system, using a basis set that is tailored according to the problem.

The choice of the basis is done so that the crystal is divided in two regions; region (I) containing non-overlapping atomic spheres and the interstitial region (II) as shown in Fig. 3.2. The mathematical treatment of the wave function inside the two regions is given in the following way:

- Inside the atomic sphere (I) of radius  $R_{Ia}$ , linear combinations of the radial

function times the spherical harmonics  $Y_l^m(\hat{r}')$  are used;

$$\phi_{\mathbf{K}}^{\mathbf{k}}(\mathbf{r}) = \sum_{l,m} [A_{l,m}^{\mathbf{K}+\mathbf{k}} u_l(r', E_{1,l}) + B_{l,m}^{\mathbf{K}+\mathbf{k}} \dot{u}_l(r', E_{1,l})] Y_l^m(\hat{r}'). \quad (3.20)$$

$u_l(r', E_{1,l})$  is the solution of radial part of the Schrödinger wave equation for the energy eigenvalue in first term while  $\dot{u}_l(r', E_{1,l})$  is the energy derivative of  $u_l(r', E_{1,l})$ . A linear mixture of these two functions include the linearization of the radial function inside the sphere.

- In second region (II) called interstitial zone, a plane wave basis of the Bloch function is applied;

$$\phi_{\mathbf{K}}^{\mathbf{k}}(\mathbf{r}) = \frac{1}{\sqrt{V}} e^{(\mathbf{K}+\mathbf{k}) \cdot \mathbf{r}}, \quad (3.21)$$

where  $\mathbf{K}$  and  $\mathbf{k}$  are the reciprocal lattice vector and wave vector inside the irreducible first Brillouin zone. The accuracy of a plane wave basis set was determined by  $K_{max}$ . In order to determine  $A_{l,m}^{\mathbf{K}+\mathbf{k}}$  and  $B_{l,m}^{\mathbf{K}+\mathbf{k}}$  it is necessary that the function in the sphere matches the plane wave both in value and in slope at the sphere boundary.

The FLAPW is all electron method, which is more accurate and flexible as compared to the pseudopotential methods. It can be applied to many kind of systems (bulk, surfaces and organic crystals etc). However this method is relatively slow and the code (WIEN2k) is complicated in which it is implemented. For structure relaxation the other approaches (plane waves) are more convenient.

### 3.4.1 WIEN2k code

The WIEN2k code [34] is frequently used computer code for various ground state properties calculations based on full potential linearized-augmented-plane-wave (FLAPW) method [35] within density functional theory (DFT). Parallel calculations can also be performed in this code. WIEN2k is portable requiring the use of FORTRAN90, MPI, BLAS, SCALAPACK etc. Friendliness use of WIEN2k is carried out by a web based graphical user interface (GUI), called w2web. Additionally, an automatic choice of default option is included in this package and may also be complemented by an extensive User's Guide.

The WIEN2K package provides the possibility to perform both non-relativistic, scalar relativistic and relativistic calculations. When running the relativistic calculations, the way in which relativity is included differs for core and valence states. The core states are assumed to be fully occupied and fully relativistic calculation is employed via solving the Dirac equation. This discussion concerns therefore the valence orbitals only. These orbitals are treated in the scalar relativistic approximation. To obtain fully relativistic calculation for the valence electrons, the SOC is included in

atomic spheres via an approximative scheme that introduces an additional term

$$H_{SOC} = \xi(\mathbf{r}) \mathbf{L} \cdot \mathbf{S} \quad (3.22)$$

to the spin-polarized Schrödinger-like scalar relativistic equation. Technically, the influence of the term (3.22) is included by starting with a scalar-relativistic FLAPW calculation without SOC. The eigenfunctions thus obtained are then used as a basis in which another diagonalization is done and this time also the SOC term Eq. (3.22) is taken into account. This procedure is often called second variational step [36].

### 3.5 The Green function method of Korringa, Kohn and Rostoker

The multiple-scattering or Korringa, Kohn and Rostoker (KKR) method for electronic structure calculation was introduced by Korringa in 1947 [37] and then by Kohn and Rostoker in 1954 [38]. For solution of Schrödinger equation, first the scattering properties of each scattering atom are determined. These properties are described by a scattering matrix. In the second step, the multiple-scattering by all atoms in the lattice is determined in such a manner that at each center the incident wave is the sum of the outgoing waves from all other centers. In KKR method one can obtain the separation between the potential and geometric properties. Further it was developed when reformulated as a KKR Green function method [39, 40, 41, 42]. The KKR method successfully calculated the electronic structure, spectroscopic properties, transport properties and magnetic properties of solids including bulk and low dimension materials [33]. The Dirac equation can be incorporated in KKR scheme, whenever relativistic effects become important [43] and were also applied to treat non-collinear magnetism [44]. The important features of KKR Green function formulation are:

- Green function provide information about the chemical identity of the atom (structure) from the scattering.
- Green function locally describe electronic properties that can be applied to disordered systems and alloys.

In density functional calculations we solve the Kohn-Sham equations for the single particle wave functions  $\phi_n$  to find the energy eigenvalues of the single particle. The basic equation is:

$$H\phi_n = E\phi_n. \quad (3.23)$$

In Green function method the wavefunction  $\phi_n$  is replaced by single particle Green function  $G(\mathbf{r}, \mathbf{r}')$  that carry all the information about the ground state. The local density of states and charge density can be directly calculated from the Green function, which is the solution of the Schrödinger equation for an energy  $E$  with a source at position  $\mathbf{r}'$  :

$$[H - E]G(\mathbf{r}, \mathbf{r}'; E) = -\delta(\mathbf{r} - \mathbf{r}'). \quad (3.24)$$

Using the identity

$$\frac{1}{x + i\epsilon} = P\frac{1}{x} - i\pi\sigma(x), \quad (3.25)$$

one can write the spectral representation for Green function

$$G(\mathbf{r}, \mathbf{r}'; E) = \sum_n \frac{\phi_n(\mathbf{r})\phi_n^*(\mathbf{r}')}{E + i\epsilon - E_n} \quad (3.26)$$

as

$$G(\mathbf{r}, \mathbf{r}'; E) = P \sum_n \frac{\phi_n(\mathbf{r})\phi_n^*(\mathbf{r}')}{E - E_n} - i\pi \sum_n \delta(E - E_n)\phi_n(\mathbf{r})\phi_n^*(\mathbf{r}'). \quad (3.27)$$

One can express the energy resolved charge density  $\rho(\mathbf{r}, E)$  using the imaginary part of the Green function:

$$\rho(\mathbf{r}, E) = \sum_n \delta(E - E_n)\phi_n(\mathbf{r})\phi_n^*(\mathbf{r}') = -\frac{1}{\pi} \text{Im}G(\mathbf{r}, \mathbf{r}; E) \quad (3.28)$$

Now one can express the charge density via one electron Green function

$$n(\mathbf{r}) = \sum_n |\phi_n(\mathbf{r})|^2. \quad (3.29)$$

$$n(\mathbf{r}) = \int_{-\infty}^{E_f} \rho(\mathbf{r}, E)dE. \quad (3.30)$$

$$n(\mathbf{r}) = -\frac{1}{\pi} \int_{-\infty}^{E_f} \text{Im}G(\mathbf{r}, \mathbf{r}; E)dE. \quad (3.31)$$

Since  $G(z)$  is analytical in the whole complex plane except the real axis, it contains poles as shown in Fig. 3.3. In order to numerically simplify our calculations one can replace the equation (3.31) by contour integral in complex energy plane

$$n(\mathbf{r}) = -\frac{1}{\pi} \int_A \text{Im}G(\mathbf{r}, \mathbf{r}; z)dz. \quad (3.32)$$

$$n(\mathbf{r}) = -\frac{1}{\pi} \int_C \text{Im}G(\mathbf{r}, \mathbf{r}; z)dz. \quad (3.33)$$

The contour integral in complex plane (see Fig. 3.3) goes along regions where  $G(z)$  is smooth function of  $z$  [45].

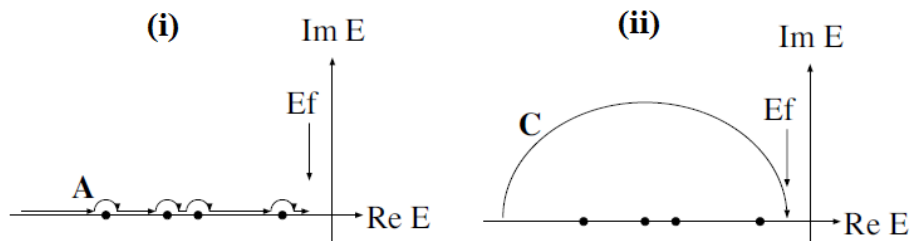


Figure 3.3: Contour integration of the Green function [45].

### 3.5.1 SPRKKR -package

This package has been developed by H. Ebert and his collaborators. This package is based on the KKR-Green function formalism using multiple scattering approximation. According to this formalism the electronic structure of a system is not expressed in terms of Bloch wave functions and eigenvalues but in term of the corresponding Green function which makes this method flexible.

In this package the electronic structure calculation of arbitrary three-dimensional (3D) periodic systems, as well as chemically disordered system can be done. The two dimensional (2D) periodic systems such as surfaces can be treated without the need for auxiliary system of 3D periodicity. One can deal with finite clusters by employing the impurity Green function formalism. The electronic structure of the system can be calculated in non-relativistic, scalar relativistic and fully relativistic mode. Atomic sphere approximation (ASA) and full potential calculation can be done in this code.

The SPRKKR code works fully relativistically, it solves a four-component Dirac equation by default [46, 47, 48, 49]. SOC is therefore implicitly fully included for all states. Nevertheless, the bare effect of the SOC can be investigated via SPRKKR if one employs an approximate two-component scheme [50] where the SOC-related term is identified by relying on a set of approximate radial Dirac equations. This scheme was used recently to investigate how the MCA energy of adatoms and monolayers on noble metals varies if SOC is selectively switched on only at some sites [51]. We employed it here for the same purpose.

Based on electronic structure calculation, a variety of properties (density of states, x-ray spectroscopy, x-ray magneto-optics and conductivity) of the ordered and disordered structures can be explored with SPRKKR package. On the other hand it is not convenient to do structure relaxation in SPRKKR code.

## 3.6 Treatment of disordered system in supercell approach

The substitutional alloys are used as a prototype where the chemical components (elements) are randomly placed on the sites of a regular lattice. More clearly the positions of the atoms are fixed, only the chemical occupation of the sites is random. The chemical disorder of substitutional alloys destroys the Bloch symmetry of the perfectly periodic lattice. In standard band structure method we can handle this situation by using the super cell. The greater the size of the supercell, the more reasonable representation of the disordered system is obtained. However increasing the size of the supercell becomes computationally very expensive. To overcome this difficulty, one can choose small size of the supercell and make the chemical occupation of all the sites as random as possible. This special case of the supercell is known as special quasi random structure (SQS).

Special quasi random structure (SQS) for the first time was proposed by Zunger *et al.* [52]. Principally, a SQS is an ordered supercell having few atoms (e.g., 4-32) that mimic the most relevant pair and multi-site correlation functions of the disordered phase. In this approximation the random alloys were described by periodic structures that clearly introduce spurious correlations beyond a certain distance that cause periodicity errors [53]. On the other hand, many physical properties of solids can be described by microscopic length scales that can be ordered according to size to form a hierarchy [52]. For example, interactions between distant neighboring element typically show small contribution to the total energy as compared to the close neighbors.

## 3.7 Treatment of disordered system in effective medium approach

Another way to model disordered systems is to use effective medium, created so that the disorder is simulated. This is the basis of so-called mean field approach. Some approximations of the mean field approach are:

### 3.7.1 Virtual crystal approximation

In random substitutional alloys all the sites are randomly occupied by either atomic species. The corresponding concentration of such atomic species in a crystal governs the probability of finding a given type of atoms in a lattice. Lets make an assumption that the site occupancies are incoherent i.e. the existence of any short range correlations or long-range correlations is overlooked. In weak scattering case the alloy potential may be considered periodic with the potential related with each site defined as averaged over different atomic types with concentrations  $c_i$  and individual potentials  $V_i$ :

$$V_C(\mathbf{r}) = \sum_i c_i V_i(\mathbf{r}). \quad (3.34)$$

This superposition set up the virtual crystal approximation (VCA).

### 3.7.2 Average t-matrix approximation

Average t-matrix approximation can be consider as the next level approximation. Suppose we have a system having localized electronic states causing large atomic potentials and hence VCA is not able to explain electronic properties of alloy. The inter-site scattering can be neglected for small concentrations and only the scattering of individual scattering centers is permitted. The scattering center described by a single-scattering t-matrix is averaged over individual single-site scattering t-matrices placed on every site of the effective ordered lattice and is given as:

$$t_{ATA}(E) = \sum_i c_i t_i(E). \quad (3.35)$$

This is called average t-matrix approximation (ATA). As at low concentrations, the small inter-site correlations are observed, the ATA leads to relatively accurate results for very diluted alloys. However, the ATA accuracy decreases with further increase in concentration, when inter-site scattering becomes more significant. The average t-matrix approximation can be considered as a non-self-consistent version of the coherent potential approximation (see below).

### 3.7.3 Coherent potential approximation

Scattering phenomena in disordered system can be described by coherent potential approximation (CPA). By applying this approximation, impurities are implanted into a specific medium having a coherent t-matrix  $t_C$  in each scattering spot.

Suppose a random alloy which contains  $n$  components  $\{A_i\}_{i=1}^n$  with concentrations  $\{x_i\}_{i=1}^n$ . Consider atom  $A_i$  is in the effective medium. The Green function for this system is given as



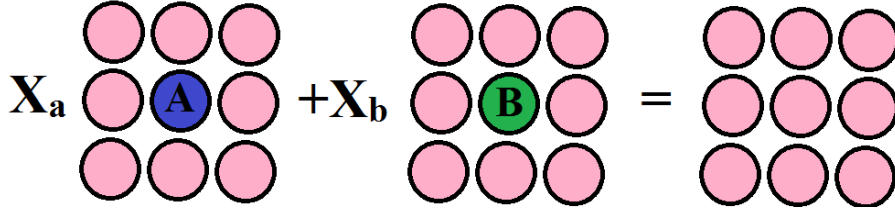


Figure 3.4: Schematic digram of the CPA condition for a binary alloy. The label "A" and "B" are occupied by impurity potentials.

$$G_{LL'}^i = \sum_{LL''} \tilde{G}_{LL''} [1 - (t_i - \tilde{t}) \tilde{G}_{L''L'}^{-1}], \quad (3.36)$$

where  $G_{LL'}^i$  is Green function of a single impurity atom in an the effective medium.  $A_i$  and  $t_i$  is the is the single site scattering  $t$  matrix of the atom  $A_i$ .  $\tilde{G}_{LL''}$  is the Green function and  $\tilde{t}_i$  is the single site scattering  $t$  matrix of the effective medium. The self consistent equation relates the Green function of the constituent atoms with the Green function of the effective (coherent) medium

$$\sum_{i=1}^n x_i G_{LL'}^i = \tilde{G}_{LL'}. \quad (3.37)$$

Equation (3.37) assumes that by taking weighted average of the Green function one can calculate the Green function of the medium. Fig. 3.4 shows schematically how the component atom is placed at the center in the effective medium.

In CPA, the disorder itself is treated very well. However, as it is a single-site method, it cannot describe the fluctuations in the local environment which exist in real alloys [54, 55]. Comparison between theory and experiment shows, nevertheless, that the CPA approach is often appropriate to describe trends of physical properties with elements concentration [56, 57, 58, 59, 60, 61, 62].

## 3.8 Calculation of magnetocrystalline anisotropy energy

### 3.8.1 Calculation of MCA energy

Magnetocrystalline anisotropy (MCA) is manifested by the fact that the energy of a magnetically ordered material depends on the direction of the magnetization  $\mathbf{M}$  with respect to the crystal lattice. It is an interesting phenomenon both for fundamental

and technological reasons, as the MCA is important among others for the design of magnetic recording media [63, 64]. In order to calculate the magnetocrystalline contribution or the MCA energy one has to determine the total electronic energy for two magnetization directions ( for example [001] and [100]) using equation (3.38) and then take the difference.

$$E_{KS} = 2 \sum_{i=1}^{N/2} \epsilon_i - \frac{1}{2} \int \frac{n(\mathbf{r}) n(\mathbf{r}')}{|\mathbf{r} - \mathbf{r}'|} d\mathbf{r} d\mathbf{r}' - \int V_{xc}(\mathbf{r}) n(\mathbf{r}) d\mathbf{r} + E_{xc}[n], \quad (3.38)$$

The first term of equation 3.38 represents summation of one-electron band energies, second term is Hartree columbic potential energy, third term is exchange-correlation potential and the fourth term is exchange-correlation energy.

The calculation of MCA energy is very sensitive and challenging. The total energies and MAE can differ by about eight or nine orders of magnitude, which requires an accurate calculation. These calculations are computationally very expensive.

In order to avoid the need for fully self-consistent calculations for the two magnetization directions and thus reduce the computational effort, one can use magnetic force theorem. In this approximation the MCA energy can be calculated by using a “frozen spin” dependent potential which does not depend on the direction of the magnetization [65], and the difference of the two energies is thus replaced by difference of band energies, i.e. only first term of equation (3.38) is considered for two magnetization directions and rest of the terms in  $E_{KS}$  are ignored.

# Chapter 4

## Motivation, earlier works, aim of this thesis

FePt is one of the important alloy system among the transition metals having large MCA energy and high Kerr rotation. These properties have been made FePt a hot contestant for next generation ultrahigh density magnetic and magneto-optical recording media [66]. Due to this FePt got much attention both experimentally and theoretically. In this thesis we investigate the two aspects of FePt that have specific role in technological applications. These are (i) magnetocrystalline anisotropy and (ii) influence of disorder on magnetic properties. For this purpose, we used ab-initio calculations to get accurate and reliable results.

The various ab-initio electronic structure codes use different approaches to solve the Schrödinger equation for a solid. Usually different codes and/or methods yield results that are similar but show sometimes important differences in the details. These details start to matter if one aims at high-precision calculations with predictive power. Therefore an effort has lately intensified to standardize ab-initio calculations and to find the conditions that have to be met so that reliable “true” quantitative values are obtained. So far the attention has been paid mostly to total energies, equilibrium lattice parameters and bulk moduli [67, 68, 69, 70]. We want to extend this effort to another numerically sensitive area, namely, to the magnetocrystalline anisotropy (MCA).

## 4.1 Ordered FePt: MCA energy

Getting an accurate value of the MCA energy  $E_{\text{MCA}}$  is quite difficult as one has to, at least in principle, subtract two very large numbers (total energies for two orientations of magnetization) to get a very small number, namely,  $E_{\text{MCA}}$ . Several conditions for getting accurate well-converged results were explored in the past. In particular, the importance of a sufficiently dense mesh in the Brillouin zone (BZ) for the  $\mathbf{k}$ -space integration was recognized [71, 72, 73]. When dealing with supported systems such as adatoms or monolayers, the semi-infinite substrate has to be properly accounted for [74, 51]. Despite all the efforts, getting accurate and reliable theoretical predictions of the MCA energy is still a problem.

We focus on MCA of bulk FePt. This compound has the largest MCA energy of all bulk materials formed by transition metals and its crystal structure is quite simple, so it is a good candidate for a reliable calculation. At the same time, the presence of Pt — a heavy element — suggests that relativistic effects should be significant, offering thus an interesting possibility to check how different methods of dealing with relativistic effects, in particular with the spin-orbit coupling, influence the results.

Previous theoretical studies on FePt based on the LDA give a large spread of the results — from 1.8 meV to 4.3 meV [75, 76, 77, 78, 79, 72, 80, 81, 66]. If one restricts to full potential methods only, one still gets a relatively large difference between various studies:  $E_{\text{MCA}}$  of FePt was determined as 2.7 meV by FP-LMTO calculation of Ravindran *et al.*[72] and FLAPW calculation of Shick and Mryasov,[80] 3.1 meV by plane-waves calculation of Kosugi *et al.*[82] and 3.9 meV by FP-LMTO calculation of Galanakis *et al.*[79]. The differences between various LDA calculations are comparable to the differences between LDA results and the experimental value of 1.3 meV [83]. Even though part of the spread of the LDA results can be attributed to the use of different LDA exchange-correlation functionals, the differences are still too large to be acceptable. Besides, they occur also for studies which use the same exchange-correlation functional (e.g., both Ravindran *et al.*[72] and Galanakis *et al.*[79] use von Barth and Hedin functional) [23]. This suggests that the accuracy of ab-initio MCA energy calculations may not be sufficient to answer a simple question such as whether the LDA itself is able to reproduce the experimental MCA energy of FePt or not.

Deciding which method gives better MCA results than the other is quite difficult, among others because different computational approaches used by different codes are intertwined with different ways of implementing relativistic effects. Recall that as the MCA is intimately related to the spin orbit coupling (SOC), which is a relativistic effect, the way the relativity is included can be an important factor. Reckoning all of this, reliable MCA energy can only be obtained if one uses two different methods

and each of them yields the same value after being properly converged. Then one can be sure that the MCA energy thus obtained is indeed “method independent” and represents the correct quantum-mechanical result.

The aim of this thesis is to perform a robust and accurate LDA calculation of the MCA energy of FePt to get a definite answer to the question whether the MCA of FePt can be described within the LDA scheme or not and to establish a benchmark against which other LDA calculations could be checked. The first computational method we employ is the full potential linearized augmented plane wave (FLAPW) method as implemented in the WIEN2k code [34]. This method was used as a reference in the recent study of the accuracy of total energies and related quantities [67, 68, 69]. As the second method we opted for a fully relativistic multiple scattering KKR (Korringa-Kohn-Rostoker) Green function formalism as implemented in the SPRKKR code [84, 85]. We will show that if both methods are properly converged, they yield same values for the MCA energy (3.4 meV). This is significantly larger than the experimental value (1.3 meV), implying conclusively that the LDA cannot properly describe the MCA of FePt.

Many aspects of the MCA of FePt were theoretically investigated in the past already. Daalderop *et al.* [75] and Ravindran *et al.* [72] studied the influence of the band-filling on  $E_{\text{MCA}}$  of FePt. Many groups studied the influence of the temperature on the MCA of FePt [86, 87]. The dependence of the Curie temperature on the FePt grain size was investigated via model Hamiltonian calculations [88]. Burkert *et al.*, [66] Lukashev *et al.* [89] and Kosugi *et al.* [82] studied how  $E_{\text{MCA}}$  depends on the strain (i.e., the  $c/a$  ratio). Cuadrado *et al.* [90] gradually substituted the Fe atom by Cr, Mn, Co, Ni, or Cu to find that the MCA energy of  $\text{Fe}_{1-y}\text{X}_y\text{Pt}$  alloys can be tuned by adjusting the content of the substituting element.

To facilitate the understanding of the MCA of FePt further, we focus on some aspects that have not been paid attention so far. In particular, we assess how different ways of dealing with relativistic effects influence magnetic moments and densities of states. We also analyze how the total energy varies with the magnetization angle and how MCA energy scales with spin-orbit coupling. Based on this we assess to what degree the mechanism leading to the MCA in FePt can be described within second order perturbation theory.

## 4.2 Disordered FePt: local environment effect

Disordered compounds are essentially important in fundamental science and as well as industrial side. In real material there is always disorder at high temperature. Several interesting properties of the solid state materials appear only in a disordered phase.

Theoretical investigation of electronic structure of disordered FePt alloys has mostly dealt with issues such as phase stability [91] and formation energies [92, 53] or with systematic dependence of properties on the concentration [93, 94]. We want to investigate magnetic properties and specifically, how magnetic moments are affected by the local environment. To get a comprehensive view, we employ both the CPA and supercell techniques.

We focus on  $\text{Fe}_{0.5}\text{Pt}_{0.5}$  substitutional alloy. This system attracted considerable attention in the past. Perlov *et al.* [95] performed a systematic study and investigated the electronic structure and the magneto-optical properties of disordered FePt alloys. Kharoubi *et al.* [96] investigated the electronic structure and the complex Kerr angle and the magnetic moments in ordered and disordered FePt multilayers and perform a complete analysis of the strong Kerr rotation with respect to photon energy.

Paudyal *et al.* [97] theoretically investigated the electronic structure and magnetic properties of FePt, CoPt and NiPt ordered and disordered alloys. They also studied the effect of short-range order in disordered phase of these alloys on magnetic moments.

Sun *et al.* [98] explored the magnetic moments and magnetic circular dichroism (MCD) of ordered and disordered  $\text{Fe}_{50}\text{Pt}_{50}$  films with full relativistic KKR code. They confirmed that the spin magnetic moment of Fe is similar for ordered and disordered films. However the orbital magnetic moments measured with MCD is greater than the calculated value.

Despite the research done so far, there are still open issues in magnetism of disordered alloys such as variation in electronic structure and magnetism of individual site with respect to local environment.

Specific aim of this thesis in this respect is to complement earlier research on FePt and other alloys by investigating local variations of electronic and magnetic structure. Specifically, we want to focus on effect of the chemical composition of the first coordination shell and on the effects of local structure relaxations. As we are interested in local effects, we will use the supercell approach and specifically the SQS's. We will also perform CPA calculations. By comparing the CPA results with results obtained via the supercell approach, we can check whether the choice of our supercells is representative enough to simulate the substitutional disorder.

The rest of thesis is arranged as follows. In chapter 5, we present the computational details. In chapter 6.1 we present magnetic moments, density of states and MCA of chemically ordered  $\text{L1}_0$  FePt. Special attention is paid to MCA. In chapter 6.2 we turn our attention to disordered FePt and present our results regarding the dependence of local magnetic moments on chemical composition of nearest neighbors. We also discuss the dependence of local magnetic moments on bonding lengths variation due to structure relaxation. Additionally we monitor broadening

of core levels by disorder and investigate how this broadening varies from one core level to another. We finally summarise our thesis in chapter 7. In Appendix A we show the convergence tests of some sensitive parameters which show the accuracy of our results.

# Chapter 5

## Computational details

We used two different computational methods, namely, the FLAPW method as implemented in the WIEN2k code [34] and the multiple scattering KKR Green function method as implemented in the SPRKKR code [84, 85]. Our calculations are based on the LDA. The values presented in chapter 6.1 were obtained using the Vosko, Wilk and Nusair (VWN) exchange-correlation functional [21]. Use of different LDA functionals leads to small but identifiable changes in  $E_{MCA}$ , as explored in Sec. 6.1.5.

The KKR Green function calculations were done mostly in the full-potential (FP) mode; sometimes the atomic spheres approximation (ASA) was employed (Sec. 6.1.4). The energy integrals were evaluated by contour integration on a semi-circular path within the complex energy plane, using a Gaussian mesh of 40 points. An important convergence parameter is the maximum angular momentum  $\ell_{\max}^{(KKR)}$  used for the multipole expansion of the Green function (see Appendix A.1). To get accurate results for MCA energy, we mostly use  $\ell_{\max}^{(KKR)}=7$ . However, if a lot of calculations with different settings has to be done (Secs. 6.1.3 and 6.1.4) we use  $\ell_{\max}^{(KKR)}=3$ , which is sufficient if the focus is on how  $E_{MCA}$  varies with the magnetization angle or with the SOC strength and not on particular values. For disordered FePt we use  $\ell_{\max}^{(KKR)}=3$ , which is sufficient for calculation of magnetic moments and density of states.

The convergence of FLAPW calculations is determined by the size of the basis. We treated Fe  $3p$ ,  $3d$ ,  $4s$  and Pt  $5p$ ,  $5d$ ,  $6s$  states as valence states and Fe  $1s$ ,  $2s$ ,  $2p$ ,  $3s$  and Pt  $1s$ ,  $2s$ ,  $2p$ ,  $3s$ ,  $3p$ ,  $3d$ ,  $4s$ ,  $4p$ ,  $4d$ ,  $4f$ ,  $5s$  states as core states. The expansion of the wave functions into plane waves is controlled by the plane wave cutoff in the interstitial region. This cutoff is specified via the product  $R_{MT}K_{\max}$ , where  $R_{MT}$  is the smallest muffin-tin (“atomic”) sphere radius and  $K_{\max}$  is the magnitude of the largest wave vector. We use  $R_{MT}K_{\max}=8$  in this study. The convergence of  $E_{MCA}$  with  $R_{MT}K_{\max}$  is investigated in Appendix A.2. The expansion of the wave functions into atomic-like functions inside the spheres is controlled by the angular-



momentum cutoff  $\ell_{\max}^{(\text{APW})}$ . We use  $\ell_{\max}^{(\text{APW})}=10$  throughout this thesis. Note that the cutoff's  $\ell_{\max}^{(\text{APW})}$  and  $\ell_{\max}^{(\text{KKR})}$  have different roles in FLAPW and KKR-Green function methods, so their values cannot be directly compared.

As concerns the muffin-tin radii in WIEN2k calculations, the atomic spheres are chosen so that they are smaller than the touching spheres for the MCA energy calculations ( $R_{\text{MT}}^{(\text{Fe})}=2.2$  a.u.,  $R_{\text{MT}}^{(\text{Pt})}=2.3$  a.u.,  $R_{\text{MT}}^{(\text{touch})}=2.527$  a.u.) because in this way the basis avoids the linearization error. On the other hand, for analyzing site-related magnetic moments we use touching muffin-tin spheres because in this way we minimize the moments associated to the interstitial region. In this way we are in a better position to compare the WIEN2k results with the SPRKKR data, where the site-related magnetic moments are determined as moments within Voronoi polyhedra. The stability of  $E_{\text{MCA}}$  with respect to  $R_{\text{MT}}$ 's variation is demonstrated in Appendix A.3.

Once the Green function components or the wave functions have been determined, the charge density is obtained via the  $\mathbf{k}$ -space integration over the BZ. The integration mesh is another important convergence parameter, common to both methods. All results presented for calculations  $E_{\text{MCA}}$  were obtained using 800000  $\mathbf{k}$ -points in the full BZ. The convergence of  $E_{\text{MCA}}$  with respect to the the number of  $\mathbf{k}$ -points is explored in Appendix A.4. Considering the convergence tests as a whole, we argue that that the numerical accuracy of our  $E_{\text{MCA}}$  values is about 0.1 meV for WIEN2k calculations and about 0.2 meV for SPRKKR calculations.

For disordered structure we only calculated the magnetic moments and density of states (see chapter 6.2) using an integration mesh of 1000  $\mathbf{k}$ -points for SQS-4 structure, 500  $\mathbf{k}$ -points for SQS-8 structure, 250  $\mathbf{k}$ -points for SQS-16 structure and 125  $\mathbf{k}$ -points for SQS-32 structure (all numbers relate to the full BZ).

Relativistic effects are implemented in the WIEN2k code in an approximative way, accounting for the SOC by a separate term (see Eq. (3.22)) which is added to the scalar-relativistic Hamiltonian. Most codes rely on this approach when they deal with SOC. The SPRKKR scheme, on the other hand, solves the Dirac equation so it does not use approximations when dealing with relativistic effects. Usually this second variational step is applied only to a subset of FLAPW eigenstates to gain a substantial speed-up. This subset is defined so that it includes all scalar-relativistic eigenstates up to energy  $E_{\max}$  above the Fermi level. The  $E_{\max}$  parameter thus plays an analogous role as  $R_{\text{MT}}K_{\max}$ . Moreover, relativistic local orbitals ( $p_{1/2}$  wavefunctions) were added to the basis [99]. To achieve the highest accuracy, we set  $E_{\max}$  as large as needed to include all FLAPW eigenfunctions in the second step (this can be achieved by setting  $E_{\max}$  of 100 Ry or higher). More details can be found in the Appendix A.5. As concerns the interstitial region, valence electrons are treated in a non-relativistic way. In this thesis “fully relativistic calculation” implies use of the Dirac equation for SPRKKR and Schrödinger equation plus separate SOC

term (3.22) in the Hamiltonian for WIEN2k, unless it is explicitly said otherwise.

# Chapter 6

## Results and discussion

### 6.1 Magnetocrystalline anisotropy of FePt

FePt is a hard magnetic alloy. Due to its high MCA energy, it is potential candidate for hard-disk drives with ultrahigh recording density.

The crystal structure of ordered FePt  $L_{10}$  is layered having tP2 unit cell ( $L_{10}$ , tP2,  $P4/mmm$ ) with Fe atom at the  $0, 0, 0$ , position and Pt atom at the  $1/2, 1/2, 1/2$  position. Lattice parameters for the tP2 unit cell are  $a=2.722 \text{ \AA}$  and  $c=3.714 \text{ \AA}$  for  $L_{10}$  FePt as shown in Fig. 6.1. Usually the large unit cell with lattice parameters  $a=3.849 \text{ \AA}$  and  $c=3.714 \text{ \AA}$ , based on tP4 unit cell with 2 Fe atoms at  $0, 0, 0$  and  $1/2, 1/2, 1/2$  positions, and Pt atoms at  $1/2, 0, 1/2$ , and  $0, 1/2, 1/2$  positions, derived from the high temperature FCC ( $A1$ , cF4,  $Fm\bar{3}m$ ) phase as shown in Fig. 6.1, is used for expediency.

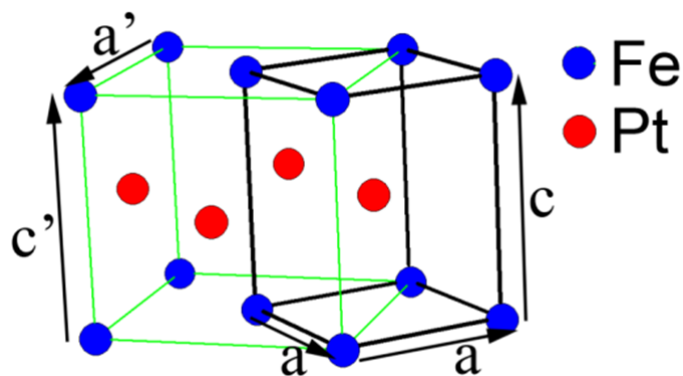


Figure 6.1: Relation between tP2 cell and tP4 cell for the  $L_{10}$ -phases

Table 6.1: Spin magnetic moments (in  $\mu_B$ ) related either to a FePt unit cell or just to the Fe site, for different ways of including the relativistic effects.

	SPRKKR		WIEN2k	
	$\mu_{\text{spin}}^{(\text{cell})}$	$\mu_{\text{spin}}^{(\text{Fe})}$	$\mu_{\text{spin}}^{(\text{cell})}$	$\mu_{\text{spin}}^{(\text{Fe})}$
non relativistic	3.17	2.86	3.15	2.86
scalar relativistic	3.21	2.86	3.21	2.87
fully relativistic	3.17	2.83	3.17	2.84

Table 6.2: Orbital magnetic moments (in  $\mu_B$ ) related to the Fe and Pt atoms in FePt for magnetization either parallel to the  $z$  axis ( $\mu_{\text{orb}}^{(\text{M}||z)}$ ) or perpendicular to the  $z$  axis ( $\mu_{\text{orb}}^{(\text{M}||x)}$ ).

	Fe		Pt	
	SPRKKR	WIEN2k	SPRKKR	WIEN2k
$\mu_{\text{orb}}^{(\text{M}  z)}$	0.065	0.065	0.044	0.042
$\mu_{\text{orb}}^{(\text{M}  x)}$	0.062	0.062	0.060	0.054

### 6.1.1 Influence of relativity on magnetic moments and density of states

The presence of Pt in FePt suggests that the way relativistic effects are treated could be important. Therefore, we calculated magnetic moments in FePt using a non-relativistic Schrödinger equation, using a scalar-relativistic approach, and using a relativistic scheme. Spin magnetic moments related either to the unit cell or only to the Fe site are shown in table 6.1. We can see that relativity has only a marginal effect on the spin magnetic moments in FePt. Orbital magnetic moments are more interesting in this respect — they would be zero in the absence of SOC. Our results in table 6.2 give the orbital magnetic moment at the Fe and Pt sites for two orientations of the magnetization.

One can see that both codes lead to very similar values for  $\mu_{\text{spin}}$  and  $\mu_{\text{orb}}$ . In

particular, the anisotropy of  $\mu_{\text{orb}}$  at Fe and at Pt sites is nearly the same. Small differences between the codes in the local magnetic moments may be due to the fact that they are defined in different regions: Wigner-Seitz cells (or more precisely Voronoi polyhedra) in SPRKKR and touching muffin-tin spheres in WIEN2k. The difference would be larger if we used “standard” setting of muffin-tin radii in WIEN2k ( $R_{\text{MT}}^{(\text{Fe})}=2.2$  a.u. and  $R_{\text{MT}}^{(\text{Pt})}=2.3$  a.u. instead of  $R_{\text{MT}}^{(\text{Fe})}=R_{\text{MT}}^{(\text{Pt})}=2.527$  a.u.): in that case, the local spin moments obtained via WIEN2k would be smaller by about 3 % and orbital moments by about 10 %.

Fig. 6.2 shows how relativity affects the density of states (DOS) resolved in angular momentum components respective to Fe and Pt sites. The data presented here were obtained using the SPRKKR code (in the FP mode); data obtained using the WIEN2k code look practically the same. Generally, there is a significant change in the DOS when going from non-relativistic to scalar-relativistic case and only a minor change when going from scalar-relativistic to the fully relativistic case. The largest difference between non-relativistic and relativistic case is for the  $s$  states. This may be due to the fact that  $s$  electrons have a large probability density near the nucleus where relativistic effects (mass-velocity and Darwin term) are stronger than at larger distances. Largest difference between scalar relativistic and fully relativistic calculations are for the Pt  $d$  states, where also the SOC is expected to be stronger than for the other cases.

For Pt  $s$  and  $d$  states one can make an interesting comparison with atomic results for Au (Ref. [100]) which are often quoted when relativistic effects in solids are discussed. It follows from Fig. 6.2 that relativistic effects shift valence Pt  $6s$  states to lower energies due to the orthogonality constraints to the more localized  $1s$  state and Pt  $5d$  states to higher energies due to a better screening of the nucleus by innermost electrons. The same happens for  $6s$  and  $5d$  atomic states of Au, respectively. So we can infer that the mechanism through which relativity affects Pt states is essentially atomic-like and common to all  $5d$  noble metals.

### 6.1.2 MCA energy evaluated by different ways

Calculating the MCA energy by subtracting total energies for two orientations of the magnetization as

$$E_{\text{MCA}} \equiv E^{(\mathbf{M}||\mathbf{x})} - E^{(\mathbf{M}||\mathbf{z})} \quad (6.1)$$

is very challenging, because the total energies and the MCA energy differ by about eight or nine orders of magnitude. We paid a lot of attention to the issues of convergence to get accurate numbers. The details can be found in the Appendix A. Here we only mention two issues which have to be given special attention.

For full-potential SPRKKR calculations, attention has to be paid to the multipole expansion of the Green function governed by the cutoff  $\ell_{\text{max}}^{(\text{KKR})}$ . KKR calculations

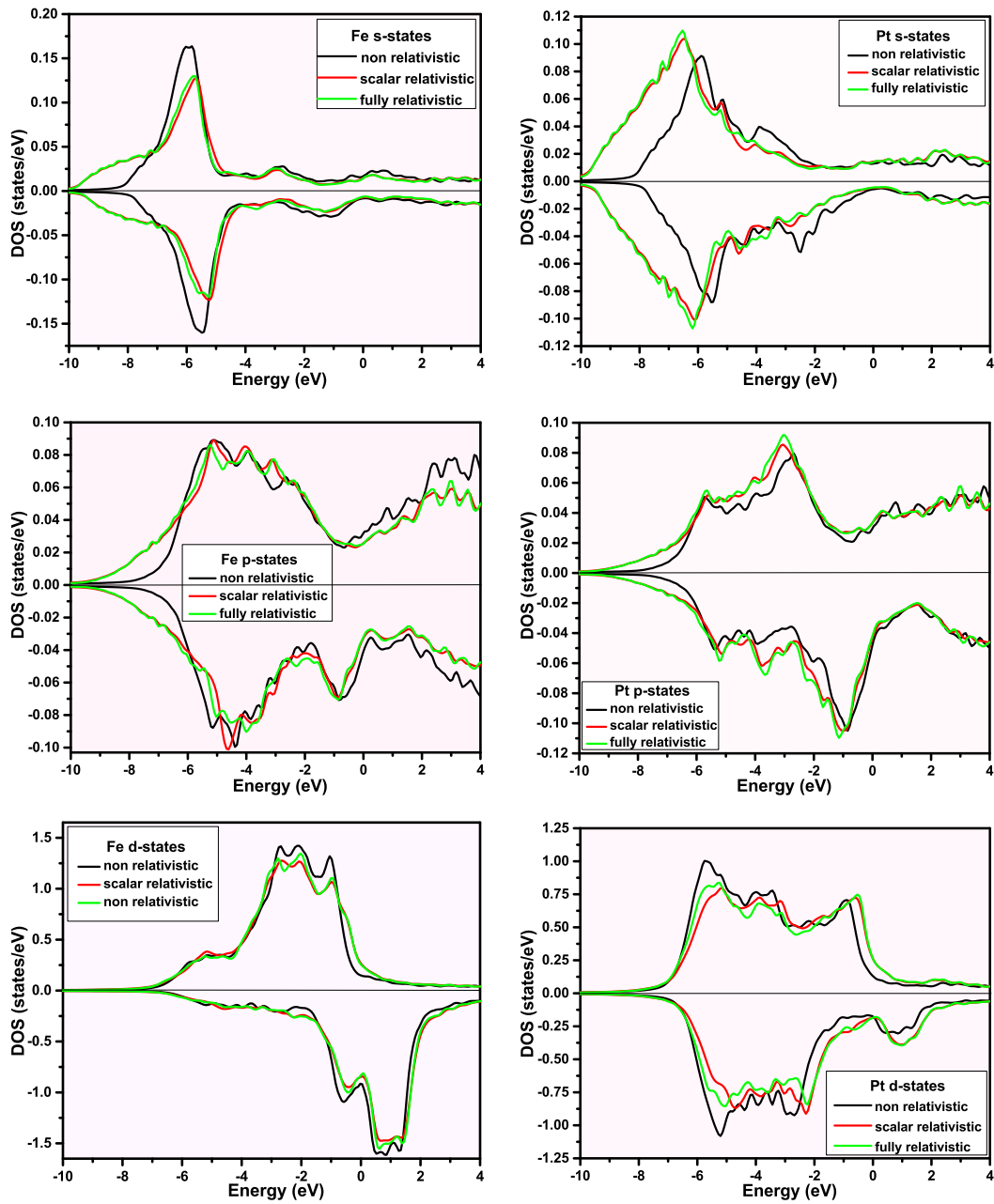


Figure 6.2: Partial spin-resolved density of states for Fe and Pt sites calculated within a non-relativistic, a scalar-relativistic and a fully-relativistic framework.

Table 6.3: MCA energy  $E_{\max}$  of FePt (in meV) calculated by three different approaches.

	SPRKKR	WIEN2k
subtracting total energies	3.04	2.99
magnetic force theorem	3.12	2.85

have known behavior concerning the  $\ell_{\max}^{(\text{KKR})}$  convergence which play role if one aims at high-accuracy total energy calculations [101, 102]. Part of the problem are numerical difficulties connected with the evaluation of the Madelung contribution to the full potential for high angular momenta [103, 104]. Note that to obtain the Green function components up to  $\ell_{\max}^{(\text{KKR})}$ , one needs potential components up to  $2\ell_{\max}^{(\text{KKR})}$  and shape functions components up to  $4\ell_{\max}^{(\text{KKR})}$ . Another difficulty is an efficient treatment of the so-called near-field corrections [103, 105]. Various ways to deal with these issues have been suggested [106, 102, 105, 107]. We performed a test of the  $\ell_{\max}^{(\text{KKR})}$  convergence (Appendix A) which indicate if that the  $\ell_{\max}^{(\text{KKR})}=7$  cutoff is used, that the numerical accuracy of the MCA energy is about 0.2 meV.

For accurate MCA energy calculations using the WIEN2k code, one has to pay special attention so that the energy parameters  $E_\ell$  used for calculating radial wave functions  $u_\ell(r, E_\ell)$  are determined very precisely and consistently. This applies, in particular, also for the relativistic local orbitals. In WIEN2k this is done by searching for the energies where  $u_\ell(R_{MT}, E)$  changes the sign to determine  $E_{\text{top}}$ , and where it has zero slope to determine  $E_{\text{bottom}}$ . The arithmetic mean of these two energies gives  $E_\ell$ . For the calculations presented here these energies had to be determined with an accuracy better than 0.1 mRy. A parameter specific for relativistic calculations via WIEN2k is  $E_{\max}$ , which controls how many scalar-relativistic eigen-states are considered when SOC is included (Appendix A.5). We used  $E_{\max}=100$  Ry, meaning that all eigen-states were included.

The MCA energy obtained by subtracting the total energies is shown in the first line of table 6.3. Values obtained via SPRKKR and WIEN2k show good agreement. Considering the convergence analysis we performed, this allows us to state that the magnetic easy axis of FePt is out-of-plane and the MCA energy is 3.0 meV within the LDA framework (for the VWN exchange-correlation functional).

Obtaining the MCA energy by subtracting the total energies is computationally very costly. The need for self-consistent calculations for two magnetization directions can be avoided if one relies on the magnetic force theorem. In this approach the MCA energy is calculated using a frozen spin-dependent potential [65, 108]. The MCA

energy is then obtained either by subtracting the band-energies or by evaluating the torque at magnetization tilt angle of  $45^\circ$  [109, 51]. As the magnetic force theorem is frequently employed, we applied it here as well. The results are shown in the second line of table 6.3. We can see that the magnetic force theorem yields very similar values as if total energies are subtracted.

Our aim was to get reliable quantitative information on the MCA of FePt, which we take as an archetypal layered system of magnetic and non-magnetic transition metals. We employed two quite different computational procedures. Both of them yield similar values for the MCA energy. Numerical stability of results is well documented by convergence tests presented in the Appendix A. Therefore the results can be trusted to represent the true LDA value of the MCA energy. Our data can be used as a benchmark for LDA calculations.

Good agreement between MCA energies obtained via the WIEN2k code and via the SPRKKR code shows that dealing with relativity by invoking the separate term Eq. (3.22) is justified in our case. As we are studying FePt, i.e., a compound containing an element with a strong SOC, it is likely that the approximative scheme associated with Eq. (3.22) is sufficiently accurate for most common situations and/or systems. One should only make sure that a sufficiently large basis for the second variation step is taken (Appendix A.5). We calculated  $E_{\text{MCA}}$  both via subtracting total energies and via the magnetic force theorem. Using the magnetic force theorem is technically much more convenient than subtracting total energies. Knowing limits of its reliability it thus vital. For pure Fe monolayers the magnetic force theorem was shown to be valid to a high accuracy [110, 111]. However, there are indications that this may no longer be true for systems with normally non-magnetic atoms with large induced moments and strong SOC [112, 113]. For such atoms one would expect rather large changes of the spin-polarized electron density upon rotation of the magnetization. This applies also for the Pt atoms in FePt. Our results indicate, nevertheless, that the magnetic force theorem yields quite accurate values for  $E_{\text{MCA}}$  for FePt (table 6.3). One can conjecture that this would be the case for similar layered systems as well.

### Relation between $E_{\text{MCA}}$ and anisotropy of $\mu_{\text{orb}}$

For the sake of completeness we checked also the Bruno formula [114], which links the MCA energy to the anisotropy of orbital magnetic moment. The Bruno formula [114] (as well as the slightly more sophisticated van der Laan formula [115]) can be derived from second order perturbation theory if some additional assumptions are made. It is often employed in the context of x-ray magnetic circular dichroism experiments that give access to the anisotropy of orbital magnetic moment via the so-called sum rules.



Even though the formula was originally derived for systems with only one atomic type, the relation between the MCA energy and the anisotropy of orbital magnetic moments has been frequently applied also for multicomponent systems [72, 116, 117, 118, 119, 120]. In such a case an estimate of  $E_{\text{MCA}}$  can be made by evaluating (cf. Ravindran *et al.* [72] and Andersson *et al.* [121])

$$E_{\text{MCA}} = \sum_i \frac{\xi_i}{4} \left( \mu_{\text{orb}}^{(i, \mathbf{M} \parallel \mathbf{z})} - \mu_{\text{orb}}^{(i, \mathbf{M} \parallel \mathbf{x})} \right), \quad (6.2)$$

where  $i$  labels the constituting atoms. This equation is valid only if off-site spin-flip terms are neglected [72, 121, 122].

We evaluated Eq. (6.2) using SOC parameters  $\xi^{(\text{Fe})}=65$  meV and  $\xi^{(\text{Pt})}=712$  meV, as obtained from ab-initio calculations for FePt relying on the method described by Davenport *et al.* [123]. We obtained  $E_{\text{MCA}} = -2.62$  meV using SPRKKR results and  $E_{\text{MCA}} = -2.09$  meV using WIEN2k results. The sign of  $E_{\text{MCA}}$  evaluated from Eq. (6.2) is wrong, indicating that this formula does not provide a suitable framework for studying the MCA of FePt. Technically, the reversal of the sign of  $E_{\text{MCA}}$  obtained via Eq. (6.2) is due to  $\mu_{\text{orb}}$  at Pt (see table 6.2): we have  $\mu_{\text{orb}}^{(\mathbf{M} \parallel \mathbf{z})} > \mu_{\text{orb}}^{(\mathbf{M} \parallel \mathbf{x})}$  at the Fe site and  $\mu_{\text{orb}}^{(\mathbf{M} \parallel \mathbf{x})} > \mu_{\text{orb}}^{(\mathbf{M} \parallel \mathbf{z})}$  at the Pt site. As  $\xi^{(\text{Pt})}$  is much larger than  $\xi^{(\text{Fe})}$ , the Pt-related term dominates in Eq. (6.2).

The Bruno formula, derived originally for single-component systems only, has recently been employed also for systems where there is more than one magnetic element [72, 116, 117, 119]. In our case the Bruno formula suggests a wrong magnetic easy axis, hence it not a suitable tool for understanding the MCA of FePt. Similar observations were made earlier for other compounds containing  $3d$  and  $5d$  elements [121, 124, 122], so we suggest that intuition based on analysis of orbital moments should not be used for these systems — despite its appeal and success in monoelemental systems.

The failure of the Bruno formula (6.2) does not automatically imply that second order perturbation theory cannot be used for describing the MCA of FePt. Namely, it is likely that additional assumptions employed in the derivation of Eq. (6.2) are not fulfilled; in particular, for Pt atoms, the exchange splitting and SOC will be of the same order of magnitude. Two more indicative tests whether second order perturbation theory itself provides a good framework for understanding the MCA of FePt are presented below.

### 6.1.3 Dependence of the total energy on the orientation of the magnetization axis

Accurate calculations can provide information on the full form of the dependence of the total energy on the angle  $\theta$  between the magnetization direction and the  $z$

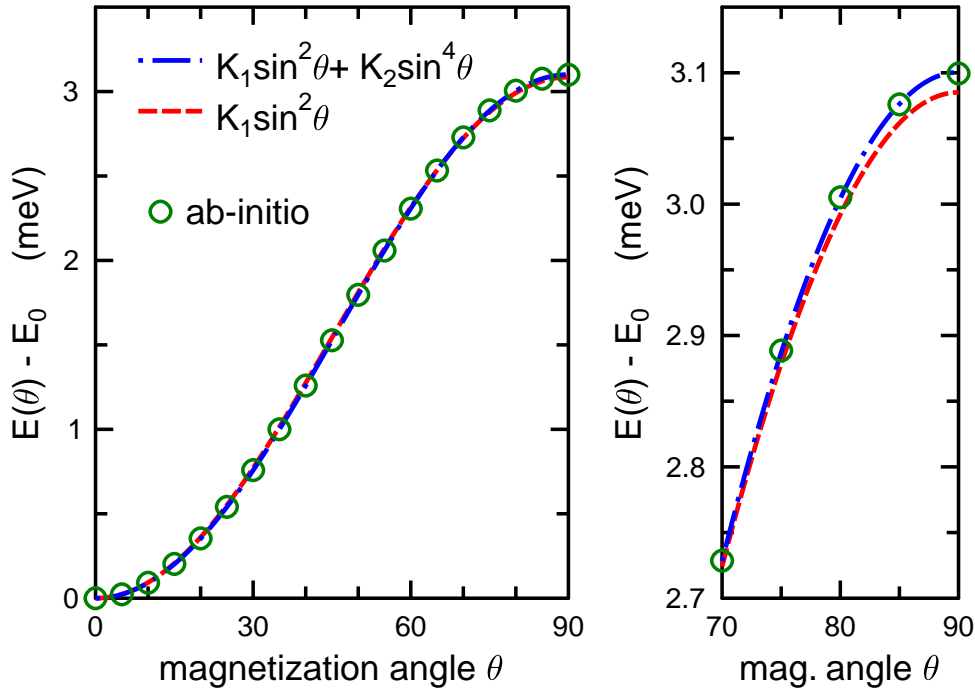


Figure 6.3: Dependence of the total energy on the magnetization angle  $\theta$  (circles) and its fit either as  $K_1 \sin^2 \theta$  (dashed line) or as  $K_1 \sin^2 \theta + K_2 \sin^4 \theta$  (dash-dotted line). An overall view is in the left panel, a detailed view on the region close to  $\theta=90^\circ$  is in the right panel.

axis. For tetragonal systems the first two terms in the directional cosines expansion of the total energy are

$$E(\theta) - E_0 = K_1 \sin^2 \theta + K_2 \sin^4 \theta . \quad (6.3)$$

Here we omit the azimuthal dependence, keeping  $\phi=0^\circ$ . If the influence of SOC is included via the explicit term Eq. (3.22), then application of second order perturbation theory leads to a simple dependence of the total energy on the angle  $\theta$  as

$$E(\theta) - E_0 = K_1 \sin^2 \theta ,$$

meaning that only the first term survives in Eq. (6.3) [114, 125]. Inspecting the full  $E(\theta)$  dependence as obtained via fully-relativistic ab-initio calculations thus provides the possibility to estimate to what degree a treatment of MCA based on second order perturbation theory is adequate: large  $K_2$  coefficient implies large deviations from second order perturbation theory.

We performed a series of calculations for different magnetization tilt angle  $\theta$ , using the SPRKKR code. The MCA energy was evaluated as a difference of total energies. The results are shown via circles in Fig. 6.3. Because we wanted to have a fine  $\theta$ -mesh, we had to perform a lot of calculations; therefore, we used  $\ell_{\max}^{(\text{KKR})}=3$  in this section. The numerical value for  $\theta=90^\circ$  thus differs a bit from table 6.3, where the  $\ell_{\max}^{(\text{KKR})}=7$  cutoff was used.

The ab-initio data were fitted via Eq. (6.3). If only the  $K_1 \sin^2 \theta$  term is employed (taking  $K_2=0$ ), we obtain  $K_1=3.085$  meV. If both terms in Eq. (6.3) are employed, we obtain  $K_1=3.008$  meV and  $K_2=0.092$  meV. Even though both fits look nearly the same in the overall view, a detailed analysis shows that the fit with both terms is significantly better (cf. the right panel in Fig. 6.3). Using even higher order terms in the fit did not lead to a significant improvement.

To summarize, our calculations show that the dependence of the total energy on the magnetization angle is fully described by Eq. (6.3). The ratio of the coefficients  $K_2/K_1$  is 0.03, thus we deduce that the MCA of FePt is dominated by the second order perturbation theory but there is also a small but identifiable contribution which cannot be described by it.

The implication coming from our analysis of the full angular dependence of the total energy is that one can indeed use the torque implementation of the magnetic force theorem: replacing the difference of energies  $E(90^\circ) - E(0^\circ)$  by the torque at  $45^\circ$  can be done only if Eq. (6.3) is valid [109, 51]. It follows from the results shown in Fig. 6.3 that this indeed is the case.

### 6.1.4 Scaling of the MCA energy with spin orbit coupling strength

For a deeper understanding we want to investigate how  $E_{\text{MCA}}$  depends on the SOC. More specifically, we are interested in how  $E_{\text{MCA}}$  varies if the SOC strength is varied at the Fe and Pt sites separately, i.e., we assume that the Hamiltonian Eq. (3.22) can be symbolically rewritten as

$$H_{\text{SOC}} = \sum_i \lambda_i \xi_i(\mathbf{r}) \mathbf{L}_i \cdot \mathbf{S}_i , \quad (6.4)$$

where  $\lambda_i$  is the scaling factor for site  $i$ . Such calculations were done via the SPRKKR code, using the approximate scheme [50] mentioned in the beginning of Sec 3.4.1.

If the magnetocrystalline anisotropy is described within second order perturbation theory, it scales with the square of the SOC-scaling parameter  $\lambda$ ,  $E_{\text{MCA}} \sim \lambda^2$  [114, 115, 125]. Inspecting the  $E_{\text{MCA}}(\lambda)$  dependence thus provides another criterion to what degree second order perturbation theory is sufficient to describe magnetocrystalline anisotropy of FePt. To get type-specific information, one should scale

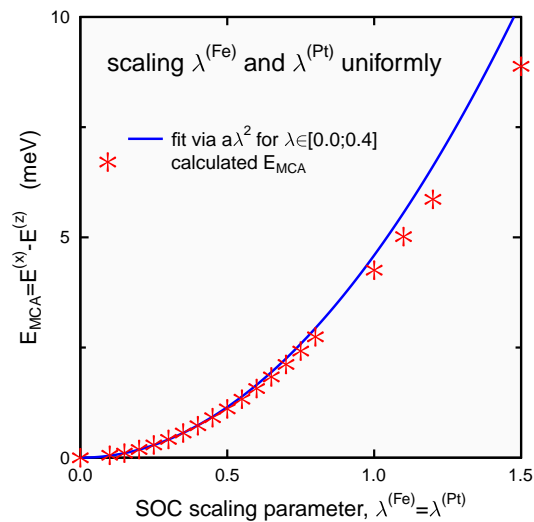


Figure 6.4: Dependence of  $E_{MCA}$  on the SOC scaling factor  $\lambda$ .

$\lambda_{Fe}$  and  $\lambda_{Pt}$  separately. In that case, however, the scaling of  $E_{MCA}$  with SOC takes a somewhat more complicated form [121]

$$E_{MCA}(\lambda_{Fe}, \lambda_{Pt}) = A \lambda_{Fe}^2 + B \lambda_{Fe} \lambda_{Pt} + C \lambda_{Pt}^2. \quad (6.5)$$

The scaling of  $E_{MCA}$  with SOC will thus retain a quadratic form only if the scaling is uniform ( $\lambda_{Fe}=\lambda_{Pt}$ ) or if SOC for one of the atomic types is zero (recovering thus the case of a single-component system [114, 115, 125]).

We start by calculating  $E_{MCA}$  for a uniform SOC scaling, i.e.,  $\lambda_{Fe}=\lambda_{Pt}$ . We vary  $\lambda$  from 0 to 1.5 to cover the non-relativistic as well as the relativistic regime: if  $\lambda$  is zero, there is no spin orbit coupling, if  $\lambda$  is 1, we recover the standard relativistic case. The calculations were done with the SPRKKR code, employing the scheme described in Sec. 6.1.4 and evaluating  $E_{MCA}$  by subtracting total energies. To reduce the computer requirements, we performed all the calculations in this section with  $\ell_{max}^{(KKR)}=3$  in the ASA mode; this enables us to use a fine  $\lambda$  mesh so that the curve fitting is reliable. The results are shown by points in Fig. 6.4. Employment of the ASA obviously leads to less accurate results than for full-potential calculations:  $E_{MCA}$  obtained within the ASA is by about 1 eV larger than  $E_{MCA}$  obtained for full potential. However, this does not affect our conclusions concerning the scaling of  $E_{MCA}$  with strength of the SOC.

To verify the predictions of the perturbation theory, we fit calculated  $E_{MCA}(\lambda)$  with the quadratic function,

$$E_{MCA}(\lambda) = a \lambda^2. \quad (6.6)$$

Perturbation theory should work well for small values of  $\lambda$  while it can be less appropriate for large values of  $\lambda$ . So the fit to the function (6.6) is performed in such a way that the  $a$  coefficient is sought only for  $\lambda$  in the range between zero

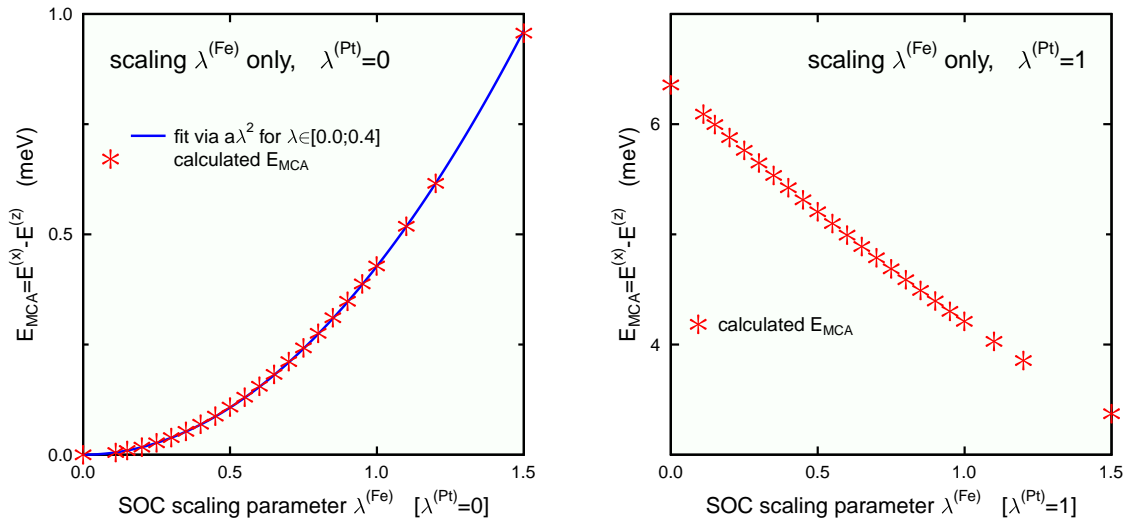


Figure 6.5: Dependence of  $E_{\text{MCA}}$  on the SOC scaling factor at the Fe sites  $\lambda^{(\text{Fe})}$ .

and 0.4 (the upper value was arbitrarily chosen just for convenience). One can see from Fig. 6.4 that while the fit describes the ab-initio data very well within the  $\lambda \in [0; 0.4]$  range, there are small but clear deviations for larger  $\lambda$ . This suggests that while second order perturbation theory accounts for the dominant mechanism of magnetocrystalline anisotropy of FePt, some effects beyond it are also present.

To learn more about atom-specific contributions to MCA, let us scale the SOC at the Fe and Pt sites separately. When varying  $\lambda_{\text{Fe}}$  or  $\lambda_{\text{Pt}}$  we further distinguish two cases — either the SOC at the remaining species is totally suppressed ( $\lambda=0$ ) or it is kept at its “normal” value ( $\lambda=1$ ). Results for scaling SOC at the Fe sites are shown in Fig. 6.5, results for scaling SOC at the Pt sites are shown in Fig. 6.6. Fits to the quadratic dependence of  $E_{\text{MCA}}$  on  $\lambda_{\text{Fe}}$  or on  $\lambda_{\text{Pt}}$  were done only in case that SOC at the other site is suppressed. Namely, if  $\lambda$  at the other atomic type is non-zero, the functional dependence is more complicated — see Eq. (6.5) — and fitting  $E_{\text{MCA}}(\lambda)$  with the simple Eq. (6.6) would not make sense. Similarly as in the case of the uniform scaling, the fits were attempted for  $\lambda$  in the  $[0; 0.4]$  interval.

Concerning the case when SOC is varied at the Fe sites, one can see that if  $\lambda_{\text{Pt}}=0$ , the dependence of  $E_{\text{MCA}}$  on  $\lambda_{\text{Fe}}$  is perfectly accounted for by second order perturbation theory: the quadratic fit describes the  $E_{\text{MCA}}(\lambda_{\text{Fe}})$  dependence very well also outside the  $[0; 0.4]$  interval in which the  $a$  coefficient was sought (left graph in Fig. 6.5). This suggests that it must be the strong SOC at Pt sites which makes the  $E_{\text{MCA}}(\lambda)$  curve in Fig. 6.4 to deviate from a perfect parabola. Indeed, if SOC at Pt sites is switched on (right graph in Fig. 6.5), the  $E_{\text{MCA}}(\lambda)$  functional dependence changes completely.

Let us turn now to the case of varying  $\lambda_{\text{Pt}}$ . If there is no SOC at the Fe sites, the  $E_{\text{MCA}}(\lambda_{\text{Pt}})$  dependence is described by the fitted parabola only for low values

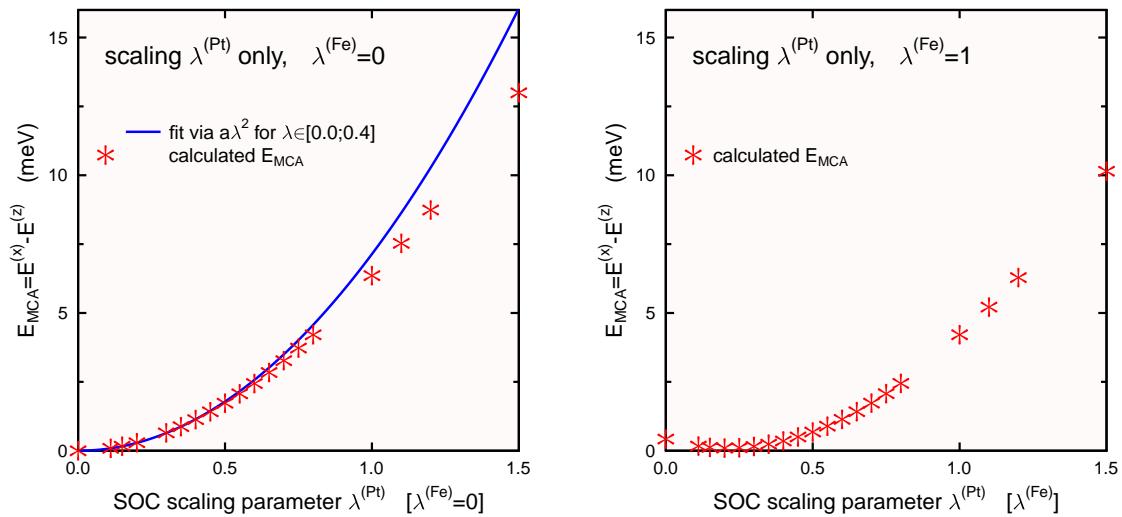


Figure 6.6: Dependence of  $E_{\text{MCA}}$  on the SOC scaling factor at the Pt sites  $\lambda^{(\text{Pt})}$ .

of  $\lambda_{\text{Pt}}$  (left graph in Fig. 6.6). If  $\lambda_{\text{Pt}}$  increases beyond the fitting interval of  $[0;0.4]$ , deviations of ab-initio data points from the fit by Eq. (6.6) are similar as for uniform SOC fit presented in Fig. 6.4. So it follows from our analysis that the effect of SOC at the Fe sites can be accounted for by second order perturbation theory while the effect of SOC at the Pt sites goes beyond it.

Concerning a more detailed view on the mechanism of MCA, we found that even though MCA of FePt is dominated by a second order perturbation theory mechanism (as found earlier by Kosugi *et al.* [82] by analyzing the dependence of  $E_{\text{MCA}}$  of FePt on  $c/a$ ), effects beyond it are clearly present as well. These effects could be identified (i) by analyzing the full angular dependence of the total energy and (ii) by inspecting how the MCA energy depends on the SOC strength. Separate scaling of SOC at Fe and Pt sites allows us to deduce that the deviations from a pure second order perturbation theory mechanism have their origin at the Pt sites. One possible mechanism that is beyond the standard second order perturbation theory is reoccupation of states close to the Fermi level [75, 126].

### 6.1.5 Dependence of the MCA energy on the LDA exchange-correlation functional

Usually the calculated properties of solids do not crucially depend on which form of the LDA exchange-correlation functional is used. However, as the MCA energy is a very sensitive quantity, it is useful to investigate how the  $E_{\text{MCA}}$  varies if different LDA exchange-correlation functionals are used. Apart from the VWN exchange-correlation functional used throughout this work we include in the comparison the

Table 6.4: The MCA energy of FePt (in meV) calculated by subtracting total energies for different exchange and correlation functionals.

	SPRKKR	WIEN2K
Vosko and Wilk and Nusair <sup>a</sup>	3.04	2.99
Perdew and Wang <sup>b</sup>	-	3.02
von Barth and Hedin <sup>c</sup>	3.29	3.18
Moruzzi, Janak and Williams <sup>d</sup>	2.97	-

a=[Ref.\[21\]](#), b=[Ref.\[22\]](#), c=[Ref.\[23\]](#), d=[Ref.\[24\]](#)

Perdew and Wang exchange-correlation functional [22] (the default for WIEN2k) and functionals suggested by von Barth and Hedin [23] and by Moruzzi, Janak and Williams [24].

We evaluated  $E_{\text{MCA}}$  by subtracting total energies for this test. The results are summarized in table 6.4. One can see that different LDA functionals lead to MCA energies that differ from each other by 0.1–0.2 meV.

When comparing our  $E_{\text{MCA}}$  with experiment (1.3–1.4 meV) [83], it is evident that the LDA result does not quite agree with it. Clearly one has to go beyond LDA for a quantitative description of MCA of FePt. It does not matter in this respect which specific form of the LDA functional is used. Nevertheless, as different LDA functionals lead to similar but still visibly different values of  $E_{\text{MCA}}$  (cf. table 6.4), each calculation of the MCA energy should be always accompanied by information which parametrization of the LDA functional was employed.

Employing the generalized gradient approximation (GGA) does not lead to substantial improvement with respect to the LDA. We obtained  $E_{\text{MCA}} = 2.73$  meV for the frequently used PBE-GGA form [127] (using the WIEN2k code and evaluating the MCA energy as a difference of total energies). It is worth to note in this respect that Shick and Mryasov were able to obtain the MCA energy of FePt as 1.3 meV by using the LDA+ $U$  approach and searching for suitable site-related values of the  $U$  parameter [80]. Interestingly, if many-body effects are described via the orbital polarization term of Brooks [128], calculated  $E_{\text{MCA}}$  is not significantly improved in comparison with the LDA [80, 72, 77, 78] — despite the fact that this approach proved to be useful when calculating orbital magnetic moments of transition metals [129, 130].

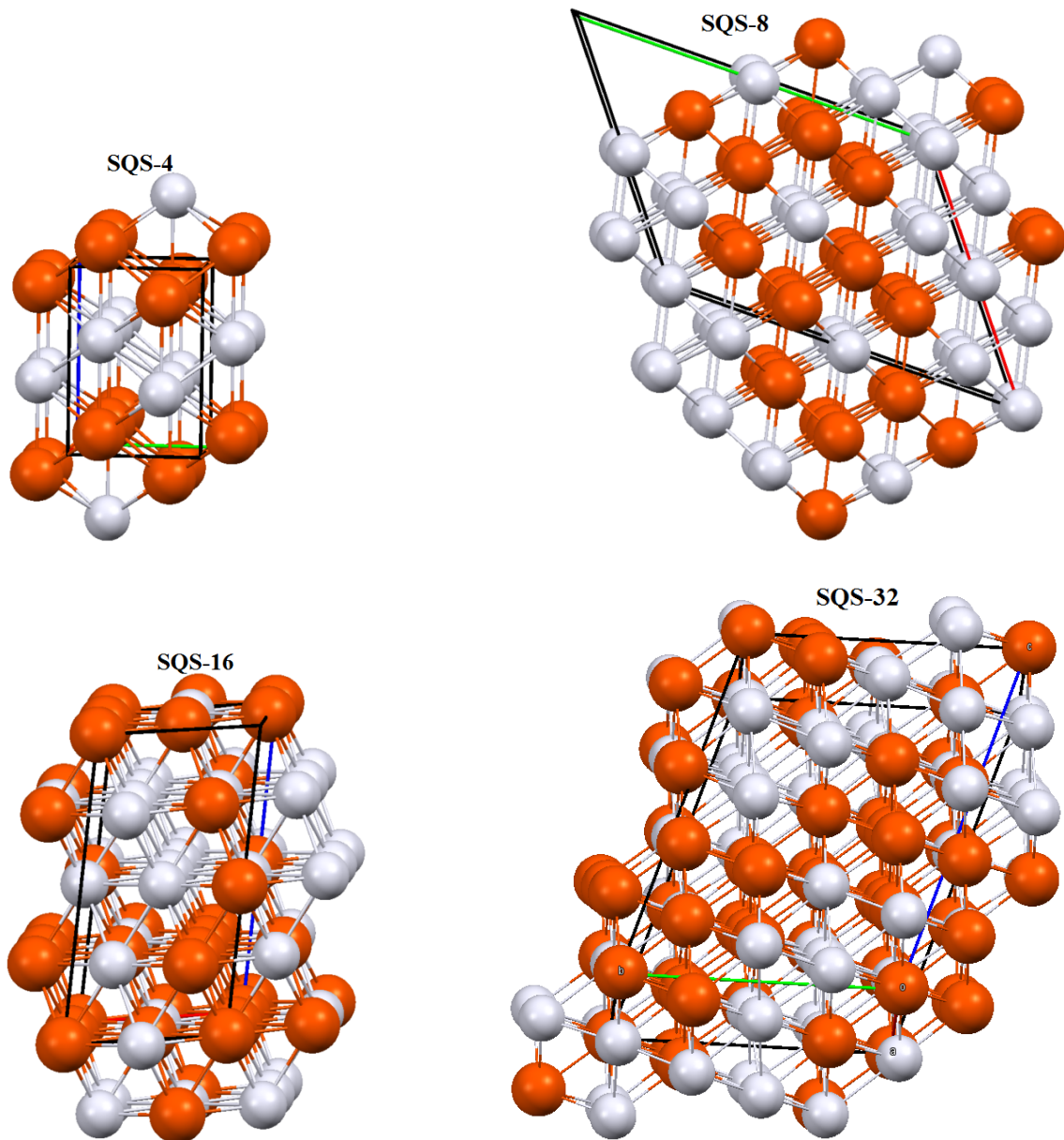


Figure 6.7: Packing structure of SQS- $N$ .

## 6.2 Disordered FePt: Local environment effects

The crystal structure of ordered FePt FCC ( $A1$ ) have lattice parameter of  $a=3.807 \text{ \AA}$ [17].

Substitutional FePt alloy (i.e., 50:50 concentration) is modeled by fcc SQS's with  $N = 4, 8, 16$  atoms per unit cell.  $L1_0$  structure with  $c/a=1$  is used for comparison. Crystallographic data for SQS-4 are taken from Zhenxing *et al.* [92], data for SQS-8 and SQS-16 are taken from Shang *et al.* [94]. Note that the present SQS-8 is equivalent to the SQS-8b structure of Lu *et al.* [131]. The structural diagrams for the SQS- $N$  systems are shown in figure 6.7.

Now we focus on the influence of coordination and nearest-neighbor distance on local magnetic moments in FePt alloy.



### 6.2.1 Average magnetic moments: comparison between supercell and CPA approach

Table 6.5 shows the average spin and orbital magnetic moments  $\langle\mu_{\text{spin}}\rangle$  and  $\langle\mu_{\text{orb}}\rangle$  for Fe and Pt atoms obtained by assuming SQS supercell geometries and by employing the CPA. No structural relaxation was performed at this stage. The magnetization is oriented along the [001] direction of the parental fcc lattice. The calculations were performed using the SPRKKR code, so a direct comparison between SQS and CPA results can be made. The data shown in table 6.5 were obtained for a full potential but we checked that using it was actually not necessary: when the atomic spheres approximation (ASA) was applied instead, the spin magnetic moments increased typically by 1 % and the orbital magnetic moments by 2-10 %.

The observed variation in  $\langle\mu_{\text{spin}}\rangle$  between different SQS's is quite small when going stepwise from  $N = 4$  to  $N = 32$ . This is especially true for the Fe atoms. For the Pt atoms, the relative deviations are a bit larger but still small. On the other hand, the variation in  $\langle\mu_{\text{orb}}\rangle$  is relatively large for the same sequence of SQS's. Again, this variation is larger for Pt atoms than for Fe atoms. Remarkably, even for the largest SQS we explore there remains a small but distinct difference in magnetic moments between the supercell and the CPA approaches. The same applies to the average taken over all SQS's.

### 6.2.2 Dependence of local magnetic moments on the chemical composition of nearest neighbourhood

In this section we focus on how local magnetic moments depend on the chemical composition of the nearest neighbourhood. All values presented here were obtained for non-relaxed structures via the SPRKKR code (as in section 6.2.1).

Table 6.6 and 6.7 show the local  $\mu_{\text{spin}}$  and  $\mu_{\text{orb}}$  for inequivalent sites in each of the SQS we explore. For each site we show also the number of nearest Fe atoms (the total number of nearest neighbors is always 12) and the multiplicity of the site in the corresponding SQS structures. Data for CPA are shown for comparison; here we “define” that there is an equal number of Fe and Pt neighbors for each atom as this corresponds to random occupation.

A better view can be obtained if local magnetic moments are plotted as a function of the number of nearest Fe atoms  $N_{\text{Fe}}$ . This is done in Fig. 6.8 for Fe sites and in Fig. 6.9) for Pt sites.

Figure 6.8 shows the local spin and orbital magnetic moments,  $\mu_{\text{spin}}$  and  $\mu_{\text{orb}}$ , respectively, for Fe sites in each of the SQS's as a function of the number of Fe

Table 6.5: Average spin and orbital magnetic moments (in  $\mu_B$  per formula unit) for Fe and Pt atoms in two ordered FePt systems and in four SQS's simulating disordered FePt alloy. Average values over all sites in all SQS's are also shown. The CPA results are presented at the bottom. The data were obtained using the SPRKKR code.

	type	$\langle\mu_{\text{spin}}\rangle$	$\langle\mu_{\text{orb}}\rangle$
L1 <sub>0</sub> ( $c/a = 0.965$ )	Fe	2.829	0.065
	Pt	0.337	0.044
L1 <sub>0</sub> ( $c/a = 1$ )	Fe	2.794	0.048
	Pt	0.322	0.044
SQS-4	Fe	2.840	0.051
	Pt	0.250	0.020
SQS-8	Fe	2.821	0.065
	Pt	0.284	0.055
SQS-16	Fe	2.828	0.072
	Pt	0.261	0.035
SQS-32	Fe	2.816	0.073
	Pt	0.264	0.043
SQS- $\langle 4, 8, 16, 32 \rangle$	Fe	2.821	0.070
	Pt	0.265	0.041
CPA	Fe	2.903	0.070
	Pt	0.239	0.039

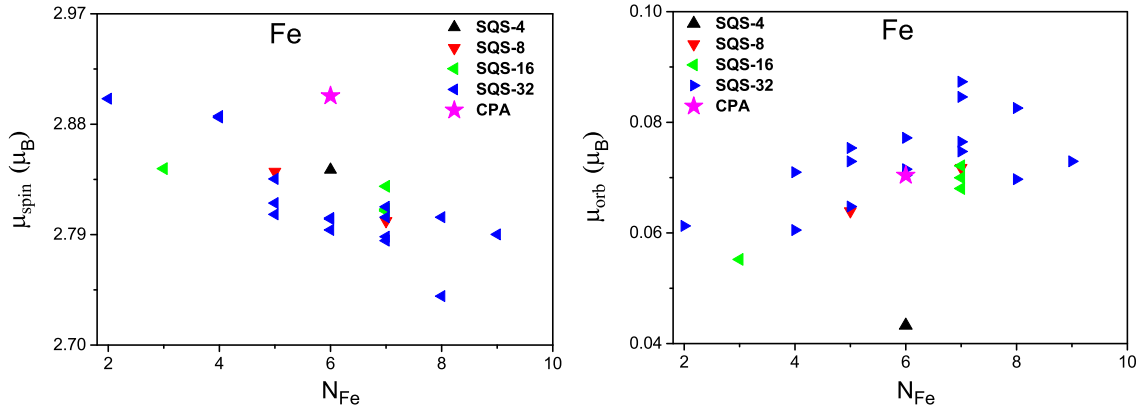


Figure 6.8: Spin and orbital magnetic moments for Fe sites in various SQS's shown as functions of the number of Fe atoms in their first coordination spheres. The CPA results are shown for comparison. The data were obtained via the SPRKKR code.

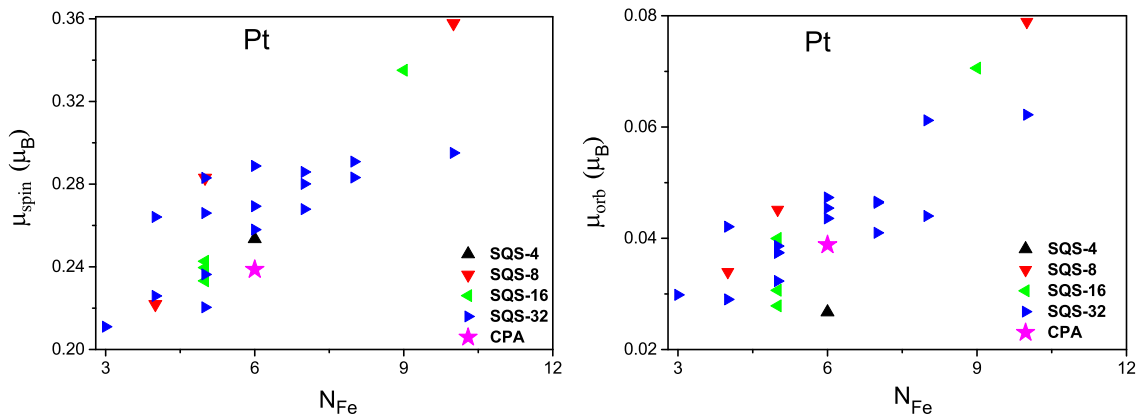


Figure 6.9: As Fig. 6.8 but for Pt sites.

atoms in their first coordinations spheres,  $N_{\text{Fe}}$ . As in the previous section, the magnetization is always parallel to the [001] direction of the parental fcc lattice.

The values of  $\mu_{\text{spin}}$  for the Fe sites are all very similar — they do not differ from each other by more than 1 %. There is a much larger spread for the local  $\mu_{\text{orb}}$  values (around 30 %). No apparent systematic trends in the dependence of  $\mu_{\text{spin}}$  or  $\mu_{\text{orb}}$  on  $N_{\text{Fe}}$  can be found in Fig. 6.8. Note that  $\mu_{\text{spin}}$  at any Fe site is always larger than  $\mu_{\text{spin}}$  for a pure Fe with the same fcc structure as the SQS's we employ ( $2.69 \mu_B$ ).

Our results can be compared with earlier work of Šipr *et al.* [132] for CoPt. We found the same trend for  $\mu_{\text{spin}}$  and as well as  $\mu_{\text{orb}}$ . The Fe  $\mu_{\text{spin}}$  is decreasing with  $N_{\text{Fe}}$  as shown in figure 6.8. This is due to the hybridization of Fe d-states. Usually in elemental Fe the  $\mu_{\text{orb}}$  show the same trend as that of  $\mu_{\text{spin}}$ , however the increasing trend the  $\mu_{\text{orb}}$  with  $N_{\text{Fe}}$  is due to the large spin orbit coupling (SOC) at the Pt atoms that effect the  $\mu_{\text{orb}}$  of Fe atoms via hybridization and induce on them an antiparallel contribution to the  $\mu_{\text{orb}}$ .

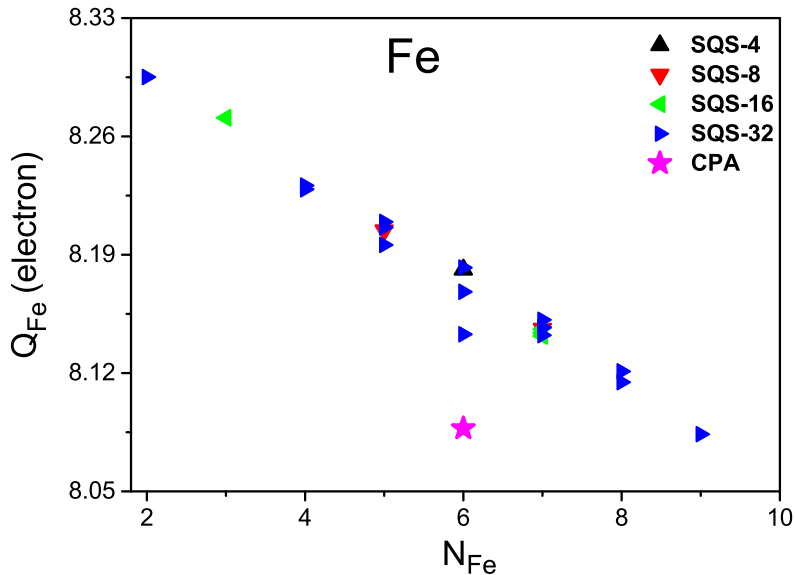


Figure 6.10: Electronic charge for Fe sites in various SQS's shown as a function of the number of Fe atoms in their first coordination spheres. The CPA result is shown for comparison. The data were obtained via the SPRKKR code.

The situation is different concerning  $\mu_{\text{spin}}$  and  $\mu_{\text{orb}}$  for Pt sites. Corresponding local and  $\mu_{\text{spin}}$  and  $\mu_{\text{orb}}$  as a function of  $N_{\text{Fe}}$  is shown in figure 6.9. One can see that when the number of Fe atoms near a Pt atom increases,  $\mu_{\text{spin}}$  and  $\mu_{\text{orb}}$  for this Pt atom increase as well. This is consistent with the fact that the magnetic moments for the Pt atoms are induced by the magnetic moments of the neighboring Fe atoms. If the number of neighboring Fe atoms increases, the induced magnetic moment increases as well.

The CPA leads to different  $\mu_{\text{spin}}$  than what is obtained for the supercells (figure 6.8). To find out more, we look at the dependence of the electronic charge at the Fe site ( $Q_{\text{Fe}}$ ) on  $N_{\text{Fe}}$ , again for various SQS's. The corresponding graph is given in figure 6.10. Here, a convincing quasi-linear relation between  $Q_{\text{Fe}}$  and  $N_{\text{Fe}}$  can be seen. The case of pure Fe with geometry of disordered FePt fits fairly well into the trend ( $Q_{\text{Fe}} = 8$ ,  $N_{\text{Fe}} = 12$ ). An analogous plot could be drawn also for electronic charge at the Pt sites (just with an opposite trend).

Let us note that figure 6.10 implies that the Fe atoms gain electrons when they are alloyed with Pt. Of course, this depends on the way the atomic regions are defined; in our case, we use Voronoi polyhedra, meaning that Fe and Pt atoms occupy identical volumes.

For a complete view we explore also the dependence of the magnetic moments at the Fe sites on the charge  $Q_{\text{Fe}}$  (figure 6.11). There is no convincing systematic trend in the data — similarly as in the case of the dependence of the magnetic moments on  $N_{\text{Fe}}$ .

Table 6.6: Local  $\mu_{\text{spin}}$  and  $\mu_{\text{orb}}$  for inequivalent sites in SQS-(4,8,16) systems. The number of nearest Fe atoms and the multiplicity (how many times the site occurs in appropriate SQS) are also shown for each site. These results were obtained for non-relaxed structures using SPRKKR . L1<sub>0</sub> structure with the  $c/a$  ratio modified so that an fcc geometry is obtained.

	type	multiplicity	$N_{\text{Fe}}$	$\mu_{\text{spin}}(\mu_B)$	$\mu_{\text{orb}}(\mu_B)$
L1 <sub>0</sub> ( $c/a = 1$ )	Fe	1	4	2.794	0.072
	Pt	1	8	0.322	0.048
SQS-4	Fe	2	6	2.840	0.051
	Pt	2	6	0.250	0.020
SQS-8	Fe	2	7	2.801	0.070
	Fe	2	5	2.841	0.060
	Pt	2	5	0.279	0.046
	Pt	1	4	0.216	0.027
	Pt	1	10	0.358	0.091
SQS-16	Fe	2	7	2.812	0.070
	Fe	2	7	2.812	0.080
	Fe	2	7	2.829	0.085
	Fe	2	3	2.844	0.054
	Pt	2	5	0.240	0.015
	Pt	2	5	0.231	0.020
	Pt	2	5	0.238	0.026
	Pt	2	9	0.336	0.078
CPA	Fe	1	6	2.903	0.070
	Pt	1	6	0.239	0.039

Table 6.7: As table 6.6 but in SQS-32 system.

	type	multiplicity	$N_{\text{Fe}}$	$\mu_{spin}(\mu_B)$	$\mu_{orb}(\mu_B)$
SQS-32	Fe	1	6	2.802	0.077
	Fe	1	5	2.807	0.073
	Fe	1	7	2.789	0.085
	Fe	1	4	2.887	0.061
	Fe	1	6	2.795	0.072
	Fe	1	4	2.887	0.071
	Fe	1	2	2.902	0.061
	Fe	1	5	2.818	0.075
	Fe	1	7	2.786	0.087
	Fe	1	9	2.792	0.073
	Fe	1	8	2.741	0.083
	Fe	1	7	2.814	0.075
	Fe	1	6	2.805	0.071
	Fe	1	8	2.806	0.070
	Fe	1	7	2.805	0.076
	Fe	1	5	2.837	0.065
	Pt	1	6	0.269	0.044
	Pt	1	5	0.283	0.032
	Pt	1	5	0.236	0.038
	Pt	1	7	0.286	0.047
	Pt	1	10	0.295	0.062
	Pt	1	5	0.266	0.037
	Pt	1	7	0.267	0.041
	Pt	1	8	0.291	0.044
	Pt	1	8	0.283	0.061
	Pt	1	5	0.219	0.037
	Pt	1	4	0.225	0.029
	Pt	1	7	0.280	0.046
	Pt	1	3	0.210	0.0298
	Pt	1	4	0.264	0.042
	Pt	1	6	0.289	0.045
	Pt	1	6	0.257	0.047
CPA	Fe	1	6	2.903	0.070
	Pt	1	6	0.239	0.039

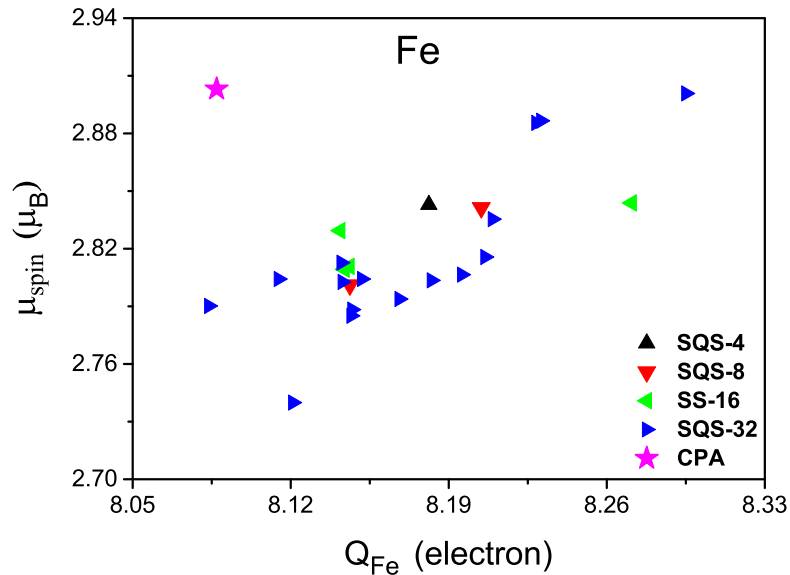


Figure 6.11: Spin magnetic moment for Fe sites in various SQS's shown as functions of the charge. The CPA result is shown for comparison. The data were obtained via the SPRKKR code.

### 6.2.3 Influence of the Madelung potential

The CPA leads to significantly different magnetic moment and charge than what would correspond to a Fe atom in a supercell with  $N_{\text{Fe}} = 6$  (Figs. 6.8 and 6.10). It appears thus that there is a small but distinct difference between the way magnetism in disordered FePt alloy is described via the CPA and via the supercell approach.

Possible reason for this difference is the single-site nature of the CPA. In particular, the standard CPA cannot account for the Madelung contribution to the potential. Therefore, we investigate how the electronic structure of the SQS's varies depending on whether the the Madelung potential is included or not. The influence of the Madelung potential on the charges at Fe sites is shown in Fig. 6.12. These calculations were done within the full potential mode. One can see immediately that neglecting the Madelung potential practically suppresses the dependence of the charge on the coordination number. The CPA result corresponds to the case when the Madelung potential is neglected. For the Pt sites the plot is analogous as for the Fe sites.

A similar comparison for the spin magnetic moments is presented in Fig. 6.14. Even though the difference between the situation with the Madelung potential and without it is not so striking as at Fig. 6.12, again we see that the data points split into two groups. Neglecting the Madelung potential increases  $\mu_{\text{spin}}$  by 0.05–0.10  $\mu_B$ , which is about the same as the difference between  $\mu_{\text{spin}}$  for Fe obtained by averaging over all SQS's and by the CPA (table 6.5). Interestingly, spin magnetic moments at

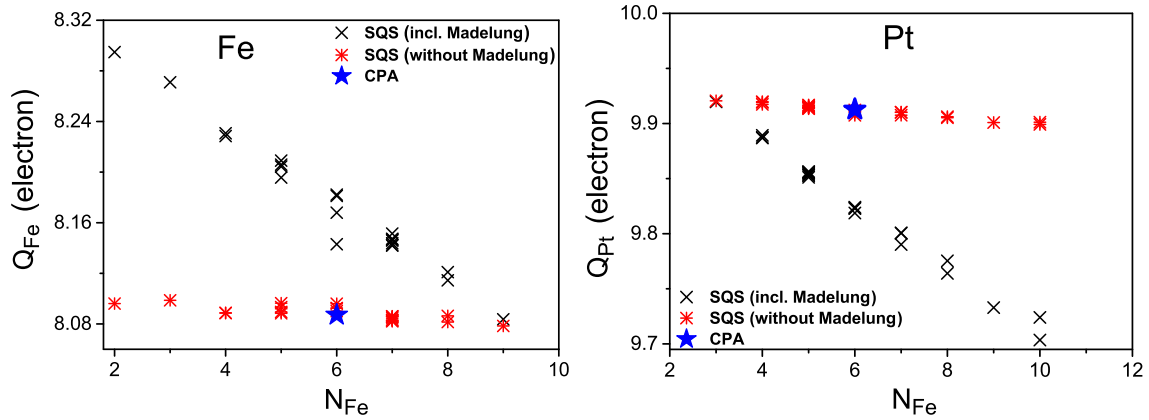


Figure 6.12: Charge at Fe and Pt sites as function of  $N_{\text{Fe}}$  for SQS-4, 8, 16 and 32 obtained with the Madelung potential either included or ignored. The result obtained within the CPA is also shown. These calculations were done by SPRKKR within the full potential mode.

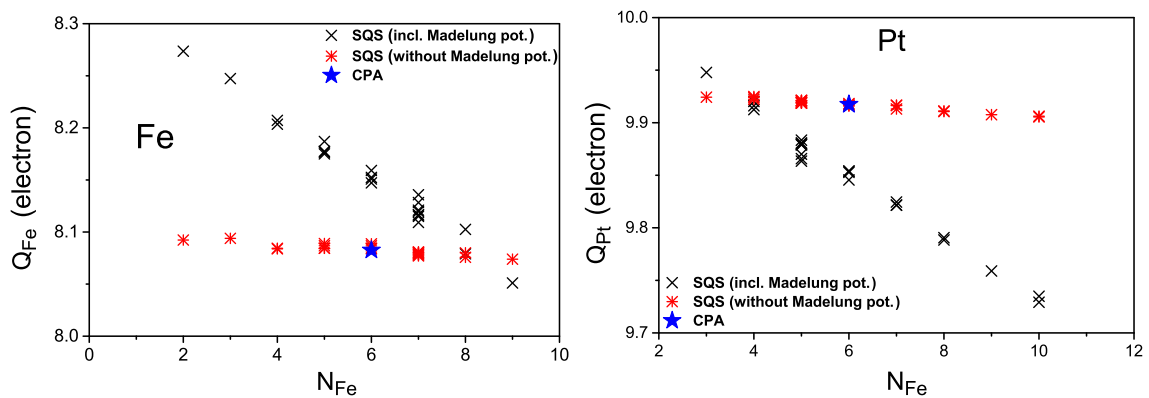


Figure 6.13: As figure 6.12 but within the ASA.



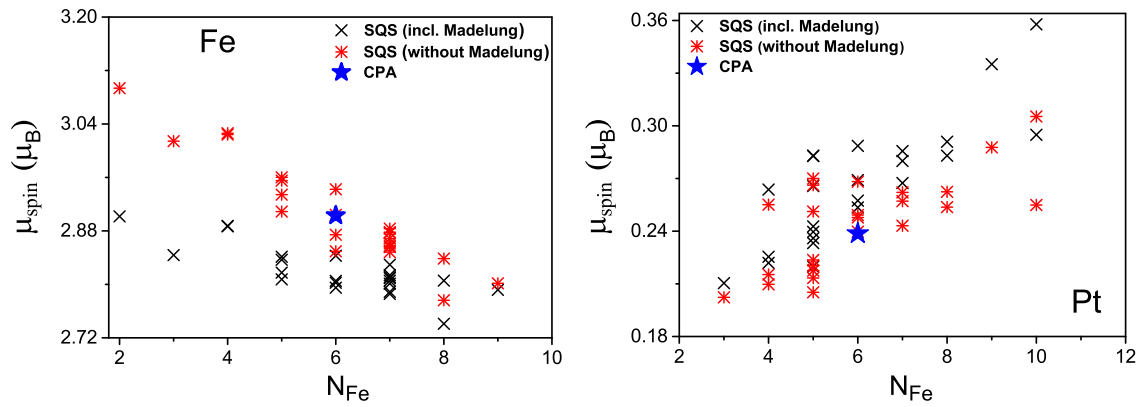


Figure 6.14: spin magnetic moments at Fe and Pt sites as function of  $N_{\text{Fe}}$  for SQS-4, 8, 16 and 32 obtained with the Madelung potential either included or ignored. The result obtained within the CPA is also shown. These calculations were done by SPRKKR within the full potential mode.

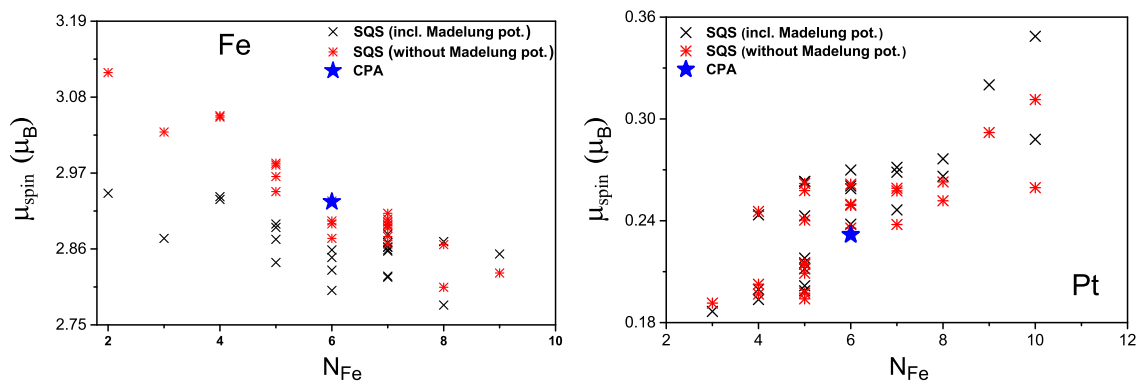


Figure 6.15: As figure 6.14 but within the ASA.

Table 6.8: Comparison of spin magnetic moment (in  $\mu_B$ ) and charge  $Q$  (in electron) obtain by averaging over supercell with CPA result. The upper part of the table contains ASA and lower part contains full potential results.

$\langle \text{SQS} \rangle$	Fe		Pt	
	$\mu_{\text{spin}}$	$Q_{Fe}$	$\mu_{\text{spin}}$	$Q_{Pt}$
ASA incl. Madelung	2.864	8.150	0.247	9.850
ASA without Madelung	2.929	8.083	0.240	9.917
ASA CPA	2.928	8.083	0.232	9.917
FP incl. Madelung	2.821	8.174	0.266	9.825
FP without Madelung	2.907	8.088	0.245	9.912
FP CPA	2.903	8.087	0.239	9.913

the Pt sites are not significantly affected by the presence or absence of the Madelung potential — the plot in Fig. 6.9 would look practically the same no matter whether the Madelung potential is included or not (also see table 6.8). This is probably linked to the fact that magnetic moments at Pt sites are induced by moments at Fe sites, so the effect of the Madelung potential is felt not only directly at the Pt sites themselves but also indirectly through change of the moments at the Fe sites.

Table 6.8 summaries the influence of the Madelung potential on average quantities, spin magnetic moment and charge in Voronoi polyhedra. There is systematic comparison between the ASA and full potential calculation. Figs. (6.12, 6.13, 6.14 and 6.15) also show the systematic comparison between ASA and full potential calculation of individual spin magnetic moment and charge in Voronoi polyhedra with respect to  $N_{Fe}$ . It seems that ASA calculations are consistent with full potential calculation.

Several modifications of the CPA method were proposed to account for the effect of the Madelung potential. A survey of these approaches would be beyond our scope but to make yet another assessment of the influence of the Madelung potential, we employ the screened impurity model for the Madelung contribution within the CPA (SIM-CPA) [133]. This model assumes that the Madelung potential can be modeled as the potential due to a screening charge which is spherically distributed at the nearest-neighbor distance. Using this approach, we obtain  $2.853 \mu_B$  for  $\mu_{\text{spin}}$  at Fe atom and  $0.244 \mu_B$  for  $\mu_{\text{spin}}$  at Pt atom. Comparing these values with table 6.5

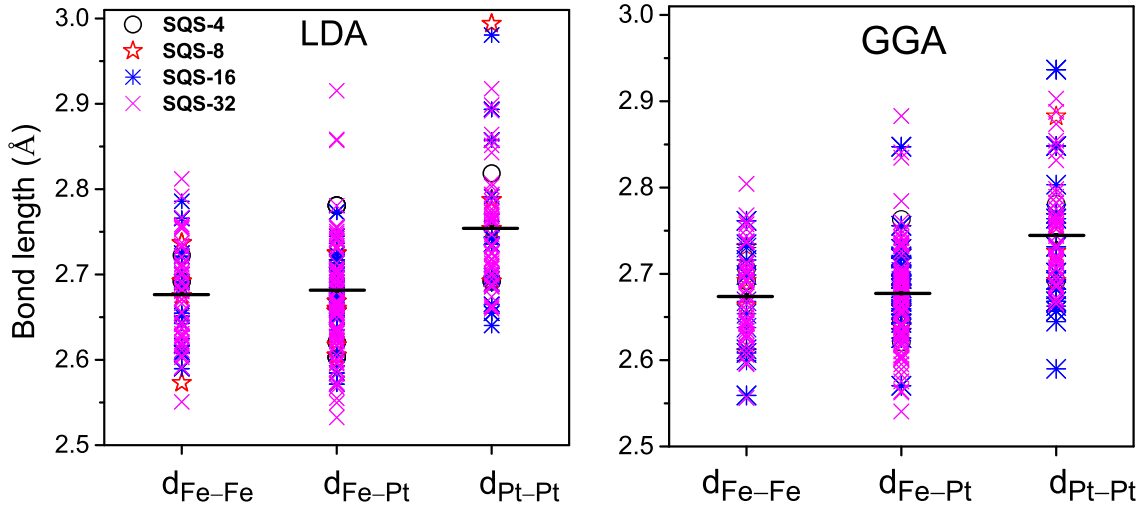


Figure 6.16: Optimized interatomic distances for the first coordination shell in SQS-4, 8, 16, and 32. Average values are shown by horizontal lines. Results were obtained via WIEN2k with the exchange-correlation potential parametrized within the LDA (left panel) and within the GGA (right panel).

we see that the SIM-CPA method pushes the standard CPA results in the desired direction. By optimizing model parameters of the SIM-CPA method [134] these values could be brought even closer to the values obtained by averaging over all SQS's. However, this would not bring any new insight for us. We conclude by summarizing that neglecting the Madelung potential by the CPA leads to small but distinct changes in magnetic moments in FePt alloy.

#### 6.2.4 Dependence of local magnetic moments on bond lengths

By optimising the positions of the atoms in the SQS, a variety of bond lengths is obtained. Here we study how variations in bond lengths affect magnetic moments. Respective calculations were performed via the WIEN2k code.

Generally, two different types of structural relaxations could be made for an SQS: relaxation of internal degrees of freedom and relaxation of external degrees of freedom. Relaxation of internal degrees of freedom means that atoms are allowed to move in the direction of a force while the lattice vectors are kept unchanged. Relaxation of external degrees of freedom means that the lengths of the lattice vectors and the angles between them are optimized. External degrees of freedom reflect whole manifold of possible configurations, it is thus reasonable to keep them fixed when using the supercell to model an alloy. To study local environment effects, we relax atomic positions only.

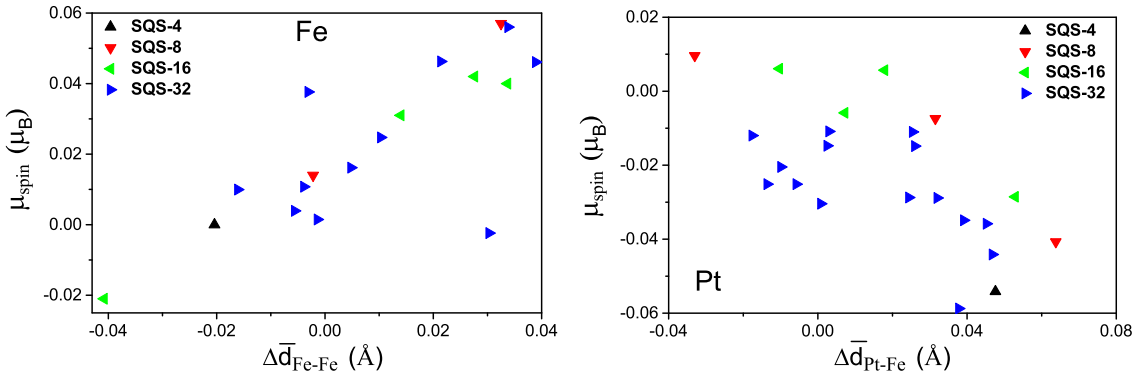


Figure 6.17: Change of the spin magnetic moment  $\Delta\mu_{spin}$  for an Fe atom (left graph) and for a Pt atom (right graph) plotted as a function of change of the average bond length  $\Delta\bar{d}_{\text{Fe-Fe}}$  or  $\Delta\bar{d}_{\text{Pt-Fe}}$ . The calculations were done by WIEN2k.

Bond-lengths  $d_{\text{Fe-Fe}}$ ,  $d_{\text{Fe-Pt}}$  and  $d_{\text{Pt-Pt}}$  resulting from the geometry optimization are shown in Fig. 6.16, both for the LDA and for the GGA. For a non-relaxed structure, all the lengths are 2.69 Å. One can see that  $d_{\text{Fe-Fe}}$  and  $d_{\text{Fe-Pt}}$  are on the average close to 2.69 Å, with  $d_{\text{Fe-Fe}}$  a bit smaller than  $d_{\text{Fe-Pt}}$ . The  $d_{\text{Pt-Pt}}$  distances are on the average larger than  $d_{\text{Fe-Fe}}$  or  $d_{\text{Fe-Pt}}$  distances. This is consistent with the fact that the interatomic distances in elemental Pt (2.77 Å) are significantly larger than the interatomic distances in elemental Fe (2.48 Å). The overall pictures provided by the LDA and by the GGA are similar. In the following only results for the LDA will be presented.

Changes in the interatomic distances cause corresponding changes in the magnetic moments. It is instructive to inspect how the change in the local spin moment  $\mu_{spin}$  is related to the change in the average distance of nearest Fe neighbours from the considered site ( $\Delta\bar{d}_{\text{X-Fe}}$ ). This is shown in Fig. 6.17. One can see that if Fe neighbours around a Fe site are pushed away (i.e.,  $\Delta\bar{d}_{\text{Fe-Fe}}$  increases),  $\mu_{spin}$  for that site increases as well. This is plausible, because increasing  $\Delta\bar{d}_{\text{Fe-Fe}}$  means that hybridization between states related to Fe atoms decreases, which leads to an enhancement of the magnetic moment. On the other hand, if Fe neighbors around a Pt site are pushed away (i.e.,  $\Delta\bar{d}_{\text{Pt-Fe}}$  increases),  $\mu_{spin}$  for this Pt atom decreases. This reflects the fact that magnetic moments at Pt atoms are induced by neighboring Fe atoms; with increasing Pt–Fe distance the effectiveness of this mechanism obviously decreases.

### 6.2.5 Density of states

Sections 6.2.1–6.2.2 contain a careful comparison between the CPA and the supercell approach as concerns integral quantities — charges and magnetic moments. Here

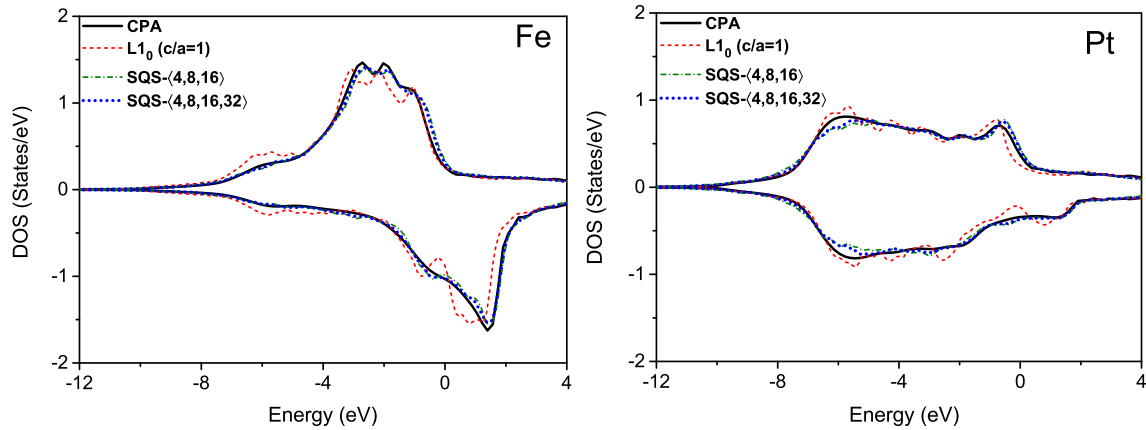


Figure 6.18: Spin-polarised density of states for Fe and Pt sites. The DOS for supercells was averaged over all sites of the SQS-4, over all sites of the SQS-4 and SQS-8, over all sites of the SQS-4, SQS-8 and SQS-16 and over all sites of the SQS-4, SQS-8, SQS-16 and SQS-32. The CPA results are shown for comparison. The calculations were performed by the SPRKKR.

we will investigate the average DOS at Fe and Pt sites as provided by the two approaches. In particular, we want to monitor how the DOS averaged over all sites of given chemical type develops if more and more inequivalent sites are included.

We present in Fig. 6.18 a sequence of the DOS curves so that we start with the DOS for the SQS-4 structure (separately for Fe and Pt atoms), then comes the DOS averaged over all sites of the SQS-4 and SQS-8 structures together, then over all sites of the SQS-4, SQS-8, SQS-16 and SQS-32 structures and finally comes the DOS averaged over all sites of the SQS- $\langle 4, 8, 16 \rangle$  and SQS- $\langle 4, 8, 16, 32 \rangle$  structures. These DOS curves are compared to the CPA results. All these calculations were performed by the SPRKKR code for non-relaxed structures.

One can see that the CPA limit is approach quite quickly. The DOS for Fe atoms approaches the CPA data more quickly than for the Pt atoms. The differences in magnetic moments between the CPA and the supercell descriptions (cf. sections 6.2.1–6.2.2) are too small to give rise to visible effects at this scale. The supercell and CPA results for the DOS become practically equivalent for SQS- $\langle 4, 8, 16, 32 \rangle$ . One can interpret this as indication that at this stage the supercell approach already presents a very good description of the disorder.

Our focus is on effects of local environment, therefore we present in Fig. 6.19 local DOS for each inequivalent site in SQS-4, 8, and 16 systems. For sake of simplicity we don't show the local DOS of SQS-32. The multiplicities of the sites as well as numbers of Fe atoms in the first coordination shells were given in table 6.6. It follows from Fig. 6.19 and table 6.6 that the most important factor is the chemical

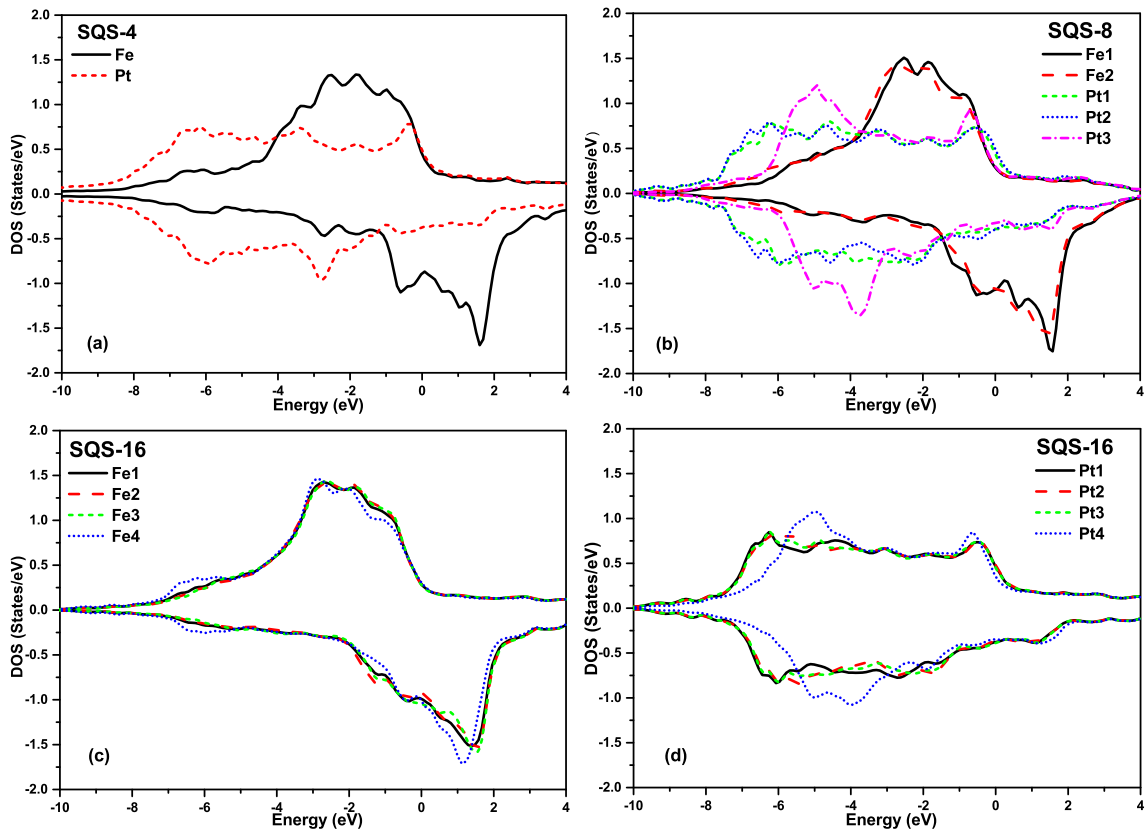


Figure 6.19: Local spin-resolved DOS for inequivalent Fe and Pt sites in SQS-4, 8, and 16. More detailed specification of the inequivalent sites is given in table 6.6.

composition of the nearest neighbourhood, i.e.,  $N_{\text{Fe}}$ . For example, Fig. 6.19b reveals that DOS at Pt sites in SQS-8 splits into two groups: Pt1 ( $N_{\text{Fe}}=5$ ) and Pt2 ( $N_{\text{Fe}}=4$ ) on the one side, Pt3 ( $N_{\text{Fe}}=10$ ) on the other side. For DOS at Fe sites in SQS-16 explored in Fig. 6.19c, one observes that data for Fe4 ( $N_{\text{Fe}}=3$ ) differs from data for Fe1, Fe2, and Fe3 ( $N_{\text{Fe}}=7$  for all of them). Likewise, DOS at Pt sites in SQS-16 explored in Fig. 6.19d shows that data for Pt1, Pt2, and Pt3 sites ( $N_{\text{Fe}}=5$ ) are similar while data for Pt4 ( $N_{\text{Fe}}=9$ ) are significantly different. Naturally, DOS curves for sites with the same  $N_{\text{Fe}}$  may also differ but in that case the differences are much smaller.

As a whole, it follows from Figs. 6.18–6.19 that deviations of local DOS from the average are smaller for Fe than for Pt. This may again be connected with the fact that states around Fe atom (a  $3d$  elements) are more localized than states around Pt atom (a  $5d$  elements).

### 6.2.6 Broadening of the core level energies due to disorder

Disorder-induced broadening of core levels cannot be investigated within the CPA because all atoms of a given type are equivalent there. However, this broadening can be studied within the supercell approach. An easy way to achieve it is inspecting ground state core level energies for inequivalent sites in the SQS's. In this way the core hole is ignored so one accounts only for initial-state effects [135].

The procedure we employ to determine the core level broadening is simpler than which was used in some earlier dedicated studies [136, 137, 138, 139, 135]. In particular, as we deal only with small supercells, we do not have enough different environments to deduce for each level a true full width at half maximum (FWHM) by a statistical analysis of the deviations of individual core levels from the average. We report just the maximum span of the core levels we obtain. Values presented below should thus be taken as estimates rather than true FWHM calculations. Nevertheless interesting information still can be obtained in this way.

We deal only with the SQS-8, SQS-16 and SQS-32 systems in this section (smaller SQS's have only one inequivalent site for each chemical type). The values presented here were obtained for non-relaxed structures, using the SPRKKR code. The core level widths (i.e., ranges of core level energies) were evaluated by analyzing core level energies for SQS-8, SQS-16 and SQS-32 systems together.

Our estimates of the broadening of core levels due to disorder are shown in table 6.9 and table 6.10. All core levels are covered by this study. For core levels split by the spin-orbit coupling (such as  $2p_{1/2}$  and  $2p_{3/2}$ ) the results are practically the same, so we only show the data for the level with larger total angular momentum. For comparison we show in table 6.9 and table 6.10 also natural core level widths due to finite core hole lifetime [136].

Table 6.9: Core level widths (in eV) of Fe SQS-N in K-M3 Levels.

	disorder broadening	life time broadening[136]
Fe $1s_{1/2}$	0.233	1.19
Fe $2s_{1/2}$	0.237	7.0
Fe $2p_{3/2}$	0.237	0.41
Fe $3s_{1/2}$	0.276	2.4
Fe $3p_{1/2}$	0.280	1.23
Fe $3p_{3/2}$	0.281	1.23

One can see from table 6.9 and table 6.10 that for most of the core levels related to given atomic type, the disorder-induced broadening is the same. This indicates that the dominant mechanism for the broadening is fluctuation in the Madelung (Coulombic) potential due to nearest neighbours [140, 139, 137]. However, for the least bound core levels, the disorder-induced broadening is larger than for the rest. This indicates that respective core level shifts are additionally affected also by other factors such as hybridization with states of neighbouring atoms.



Table 6.10: Core level widths (in eV) of Pt SQS-N in K-M3 Levels.

	disorder broadening	life time broadening[136]
Pt $1s_{1/2}$	0.191	49.5
Pt $2s_{1/2}$	0.201	8.8
Pt $2p_{3/2}$	0.203	5.39
Pt $3s_{1/2}$	0.211	14.9
Pt $3p_{3/2}$	0.218	8.3
Pt $3d_{5/2}$	0.216	2.08
Pt $4s_{1/2}$	0.229	8.25
Pt $4p_{3/2}$	0.230	4.9
Pt $4d_{5/2}$	0.231	3.95
Pt $4f_{7/2}$	0.237	0.31
Pt $5s_{1/2}$	0.285	-
Pt $5p_{1/2}$	0.303	-
Pt $5p_{3/2}$	0.326	-

# Chapter 7

## Conclusions

A detailed study involving more codes and methods yields new and reliable information about the electronic structure and magnetism of ordered and disordered FePt. In particular we found that if electronic structure calculations performed by means of FLAPW and KKR methods are properly converged, they yield the same results even for such sensitive quantities as the magnetocrystalline anisotropy energy. The proper LDA value of the MCA energy for FePt (3.0 meV for the VWN exchange-correlation functional) is significantly larger than in experiment (1.3 meV), meaning that the MCA of FePt can be described properly only if many-body effects beyond the LDA are included. As our value of  $E_{\text{MCA}}$  was obtained by two different methods and the convergence of both of them was carefully checked, it can be used as a benchmark in future calculations.

It is not really important whether relativistic effects for FePt are accounted for by solving the full Dirac equation or whether the spin-orbit coupling is treated as a correction to the scalar-relativistic Hamiltonian. The main mechanism of MCA in FePt can be described within the framework of second order perturbation theory. However, a small yet distant contribution not accountable for by the second order perturbation theory is present as well.

Our calculations for disordered FePt systems show that by increasing the number of atoms  $N$  in special quasirandom structures SQS- $N$ , the results for the magnetic moments and for the DOS approach the results obtained via the CPA. However, a small “residual difference” remains between magnetic moments obtained by both approaches. This is due to the neglect of the Madelung potential in the CPA.

The local magnetic moments associated with Fe atoms are more robust with respect to variations of the local environment than the magnetic moments associated with the Pt atoms. This reflects the fact that magnetism at Pt sites is induced by neighboring Fe atoms and that electronic states derived from the Pt atoms are more delocalized than states derived from the Fe atoms. If structural relaxation

is performed, the distances between the Pt atoms  $d_{\text{Pt-Pt}}$  are larger on the average than distances between the Fe atoms  $d_{\text{Fe-Fe}}$  or distances between the Fe and Pt atoms  $d_{\text{Fe-Pt}}$ . The magnetic moments at the Fe sites increase if the average  $d_{\text{Fe-Fe}}$  distance increases. The magnetic moments at the Pt sites decrease if the average  $d_{\text{Fe-Pt}}$  distance increases, in accordance with intuition.

Disorder induces broadening of core levels due to fluctuations in the chemical composition around atoms. This broadening is practically the same for all deep core levels associated with given chemical element, emphasizing that the mechanism of this broadening comes from fluctuations of the Madelung potential. Broadening of the least bound core levels differs from broadening of deep levels, suggesting that for these levels other factors (such as hybridization) also contribute.

# Appendix A

## Convergence tests

As we discussed in Sec. 6.1.2, the total energies and the MCA energy can differ by about eight or nine orders of magnitude. Therefore very well converged calculations are required for precise values of the MCA energy. In the following we check the influence of different technical parameters on the MCA energy if the WIEN2k or SPRKKR codes are used.

The  $E_{\text{MCA}}$  values presented in this appendix sometimes differ from the values presented in the Results section of this thesis. This is because in order to save computer resources, when studying the dependence of  $E_{\text{MCA}}$  on a particular convergence parameter, the other parameters were sometimes set to lower values than what would lead to the most accurate results. These circumstances do not influence the outcome of the convergence tests.

Unless explicitly stated otherwise, the setting of technical parameters in this Appendix is the following (cf. 5):  $\ell_{\text{max}}^{(\text{KKR})}=3$  (for SPRKKR),  $R_{\text{MT}}^{(\text{Fe})}=2.2$  a.u.,  $R_{\text{MT}}^{(\text{Pt})}=2.3$  a.u.,  $R_{\text{MT}}K_{\text{max}}=8$ ,  $\ell_{\text{max}}^{(\text{APW})}=10$ ,  $E_{\text{max}}=100$  Ry (for WIEN2k). Reciprocal space integrals were evaluated using a mesh of 100000  $\mathbf{k}$ -points in the full BZ (both codes). Based on the results presented below, we argue that the numerical accuracy of our  $E_{\text{MCA}}$  calculation is about 0.1 meV.

These convergence tests are source of strict and very helpful. Based on these convergence tests, we can make sure that our result for the disordered systems are also reliable.

Table A.1: Convergence of  $E_{\text{MCA}}$  obtained via the SPRKKR code with the angular momentum cutoff  $\ell_{\text{max}}^{(\text{KKR})}$ .  $E_{\text{MCA}}$  was evaluated by subtracting total energies.

$\ell_{\text{max}}^{(\text{KKR})}$	$E_{\text{MCA}}$ (meV)
2	1.289
3	3.101
4	3.437
5	3.423
6	3.217
7	3.039

## A.1 Convergence of SPRKKR calculations with $\ell_{\text{max}}^{(\text{KKR})}$

KKR calculations of total energies are quite sensitive to the  $\ell_{\text{max}}^{(\text{KKR})}$  cutoff. Therefore, we explore the dependence of our results on this parameter. The results are shown in table A.1. It follows from the table that cutting the angular momentum expansion at  $\ell_{\text{max}}^{(\text{KKR})}=3$  (as it is commonly done for transition metals) yields qualitatively correct value for the MCA energy.

One can see from table A.1 that even for  $\ell_{\text{max}}^{(\text{KKR})} = 7$ , a full convergence still has not been reached. However, increasing  $\ell_{\text{max}}^{(\text{KKR})}$  further would be computationally very demanding and, moreover, the issue of  $\ell_{\text{max}}^{(\text{KKR})}$  convergence would get intertwined with numerical problems in evaluating the Madelung potential and near-field corrections, so the real benefit of it would be dubious. We conclude that this limits the numerical accuracy of  $E_{\text{MCA}}$  calculations to about 0.2 meV.

Table A.2: Convergence of  $E_{\text{MCA}}$  obtained via the WIEN2k code with  $R_{\text{MT}}K_{\text{max}}$ .  $E_{\text{MCA}}$  was evaluated by means of the magnetic force theorem.

$R_{\text{MT}}K_{\text{max}}$	$E_{\text{MCA}}$ (meV)
6.0	2.851
7.0	3.046
8.0	3.051
9.0	3.081
10.0	2.993
11.0	3.013

## A.2 Convergence of WIEN2k calculations with $R_{\text{MT}}K_{\text{max}}$

An important parameter for the FLAPW calculations is the size of the basis set. It can be controlled by the  $R_{\text{MT}}K_{\text{max}}$  product. The value  $R_{\text{MT}}K_{\text{max}} = 7.0$  is set by default in WIEN2k. We increased the product  $R_{\text{MT}}K_{\text{max}}$  step by step from 6.0 up to 11.0 and calculated the MCA energy. The results are shown in table A.2. It is clear from this that reliable values for the MCA energy can be obtained for a basis set determined by the  $R_{\text{MT}}K_{\text{max}}=8.0$  condition.

## A.3 Stability of WIEN2k calculations with respect to $R_{\text{MT}}$ variations

Recently the stability of the results with respect to varying the muffin-tin radii was adopted as an informative test whether the FLAPW basis set is sufficient or not. Namely, in this way one changes the regions where the wave functions are expanded in terms of plane waves and where they are expanded in terms of atomic-like functions. Only if both expansions are appropriate the result will be stable against this variation. We adopted this test in our study, the results are summarized in ta-

Table A.3: Dependence of  $E_{\text{MCA}}$  obtained via the WIEN2k code on muffin-tin radii  $R_{\text{MT}}$ .  $E_{\text{MCA}}$  was evaluated by subtracting total energies.

$R_{\text{MT}}^{(\text{Fe})}$ (a.u.)	$R_{\text{MT}}^{(\text{Pt})}$ (a.u.)	$E_{\text{MCA}}$ (meV)
2.100	2.200	3.012
2.180	2.280	3.083
2.185	2.285	3.009
2.190	2.290	3.044
2.195	2.295	3.074
2.200	2.300	3.051
2.210	2.310	3.042
2.215	2.315	3.012
2.220	2.320	3.004
2.250	2.350	3.027
2.300	2.400	3.021

ble A.3. We can see from a good agreement between the MCA energies obtained for different muffin-tin radii settings that the basis we used for our WIEN2k calculations is appropriate for our purpose.

## A.4 Convergence of SPRKKR and WIEN2k calculations with the number of k-points

A very important parameter is the number of  $\mathbf{k}$ -points used in evaluating the integrals in the reciprocal space. We performed corresponding tests for both codes. The dependence of  $E_{\text{MCA}}$  on the number of  $\mathbf{k}$ -points in the full BZ is shown in table A.4. One can see that using about 100000  $\mathbf{k}$ -points in the full Brillouin zone is sufficient to get reliable results.

Table A.4: Convergence of  $E_{\text{MCA}}$  calculated by the SPRKKR and WIEN2k codes with the number of  $\mathbf{k}$ -points in the full BZ.  $E_{\text{MCA}}$  (in meV) was evaluated by subtracting total energies.

no. of $\mathbf{k}$ -points	$E_{\text{MCA}}(\text{SPRKKR})$	$E_{\text{MCA}}(\text{WIEN2k})$
1000	2.894	2.996
10000	3.174	3.052
60000	3.129	3.009
100000	3.061	3.051
140000	3.091	3.024
180000	3.092	2.944
220000	3.099	3.090
260000	3.103	3.001
500000	3.099	2.997
800000	3.096	2.989



Table A.5: Convergence of  $E_{\text{MCA}}$  obtained via the WIEN2k code with  $E_{\text{max}}$ .  $E_{\text{MCA}}$  was evaluated either by subtracting total energies (the second column) or by means of the magnetic force theorem (the third column).

$E_{\text{max}}$ (Ry)	$E_{\text{MCA}}$ (meV)	$E_{\text{MCA}}$ (meV)
	via $E_{\text{tot}}$	via force th.
2	3.117	2.955
5	3.071	2.961
10	3.064	2.965
100 (all states)	3.051	2.967

## A.5 Convergence of WIEN2k calculations with $E_{\text{max}}$

When including the SOC within the second variation step, the size of the new basis set is determined by the  $E_{\text{max}}$  parameter (see chapter 5 of the thesis). If  $E_{\text{max}}$  is sufficiently large, all scalar-relativistic eigenstates are involved. The effect of varying  $E_{\text{max}}$  on the MCA energy is shown in table A.5. One can see that if  $E_{\text{MCA}}$  is evaluated by means of the magnetic force theorem, it converges more quickly with  $E_{\text{max}}$  than if  $E_{\text{MCA}}$  is evaluated via subtracting the total energies. In both cases, nevertheless, the convergence is quite good.

# Bibliography

- [1] P. Hohenberg and W. Kohn. Inhomogeneous electron gas. *Phys. Rev.*, 136:B864–B871, 1964.
- [2] W. Kohn and L. J. Sham. Self-consistent equations including exchange and correlation effects. *Phys. Rev.*, 140:A1133, 1965.
- [3] R. G. Parr and Y. Weitao. *Density-Functional Theory of Atoms and Molecules*, page 352. Oxford University Press, Oxford, 1995.
- [4] M. Friák M. Šob, D. Legut, J. Fiala, and V. Vitek. The role of ab initio electronic structure calculations in studies of the strength of materials. *Materials Science and Engineering: A*, 387:148, 2004.
- [5] P. Lyman, H. R. Varian, K. Swearingen, P. Charles, N. Good, L. L. Jordan, and J. Pal. School of information management and systems, 2003.
- [6] <http://www.hitchigst.com/hdd/technolo/overview/chart02.html>.
- [7] Z. Z. Bandic and R. H. Victora. Advances in magnetic data storage technologies. volume 96, page 1749, IEEE, 2008.
- [8] B. D. Cullity. *Introduction to Magnetic Materials*. Addison-Wesley, 1972.
- [9] W. M. Bibby and D. Shoenberg. Spin properties of conduction electrons in the noble metals. *Physics Letters A*, 60:235, 1977.
- [10] H. Bethe and E. Salpeter. *Quantum Mechanics of One and Two-Electron Atoms*. Springer, New York, 1957.
- [11] P. Gambardella, S. Rusponi, M. Veronese, S. S. Dhesi, C. Grazioli, A. Dallmeyer, I. Cabria, R. Zeller, P. H. Dederichs, K. Kern, C. Carbone, and H. Brune. Giant magnetic anisotropy of single cobalt atoms and nanoparticles. *Science*, 300:1130, 2003.
- [12] J. Honolka, T. Y. Lee, K. Kuhnke, A. Enders, R. Skomski, S. Bornemann, S. Mankovsky, J. Minár, J. Staunton, H. Ebert, M. Hessler, K. Fauth,

- G. Schütz, A. Buchsbaum, M. Schmid, P. Varga, and K. Kern. Magnetism of fep surface alloys. *Phys. Rev. Lett.*, 102:067207, 2009.
- [13] J. C. Lodder and L. T. Nguyen. FePt thin films: Fundamentals and applications. In *Encyclopedia of Materials: Science and Technology*, page 1. Elsevier, Amsterdam, 2005.
- [14] S. N. Piramanayagam. Perpendicular recording media for hard disk drives. *J. Appl. Phys.*, 102:011301, 2007.
- [15] J.-M. Qiu and J.-P. Wang. Tuning the crystal structure and magnetic properties of FePt nanomagnets. *Adv. Mater.*, 19:1703, 2007.
- [16] K. Okhotnikov, T. Charpentier, and S. Cadars. Supercell program: a combinatorial structure-generation approach for the local-level modeling of atomic substitutions and partial occupancies in crystals. *J. Cheminform.*, 8:1, 2016.
- [17] J. V. Lyubina. *Nanocrystalline Fe-Pt alloys: phase transformations, structure and magnetism*. Cuvillier, Göttingen, 2007.
- [18] E. Wimmer, R. Najafabadi, G. A. Young Jr, J. D. Ballard, T. M. Angeliu, J. Vollmer, J. J. Chambers, H. Niimi, J. B. Shaw, C. Freeman, M. Christensen, W. Wolf, and P. Saxe. Ab initio calculations for industrial materials engineering: successes and challenges. *J. Phys.: Condens. Matter*, 22:384215, 2010.
- [19] J. P. Perdew and A. Zunger. Self-interaction correction to density-functional approximations for many-electron systems. *Phys. Rev. B*, 23:5048, 1981.
- [20] D. M. Ceperley and B. J. Alder. Ground state of the electron gas by a stochastic method. *Phys. Rev. Lett.*, 45:566, 1980.
- [21] S. H. Vosko, L. Wilk, and M. Nusair. Accurate spin-dependent electron liquid correlation energies for local spin density calculations: a critical analysis. *Can. J. Phys.*, 58:1200, 1980.
- [22] J. P. Perdew and Y. Wang. Accurate and simple analytic representation of the electron-gas correlation energy. *Phys. Rev. B*, 45:13244, 1992.
- [23] U. von Barth and L. Hedin. A local exchange-correlation potential for the spin polarized case. i. *J. Phys. C: Solid State Phys*, 5:1629, 1972.
- [24] V. L. Moruzzi, J. F. Janak, and A. R. Williams. *Calculated Electronic Properties of Metals*. Pergamon, New York, 1978.

- [25] J. P. Perdew K. Burke and M. Levy. *in Modern Density Functional Theory: A Tool for Chemistry edited by J. M. Seminario and P. Politzer.* Elsevier, Amsterdam, 1995.
- [26] R. O. Jones and O. Gunnarsson. The density functional formalism, its applications and prospects. *Rev. Mod. Phys.*, 61:689, 1989.
- [27] D. Porezag and M. R. Pederson. Density functional based studies of transition states and barriers for hydrogen exchange and abstraction reactions. *J. Chem. Phys.*, 102:9345, 1995.
- [28] D. R. Hamann. Generalized gradient theory for silica phase transitions. *Phys. Rev. Lett.*, 76:660, 1996.
- [29] G. Ortiz. Gradient-corrected pseudopotential calculations in semiconductors. *Phys. Rev. B*, 45:11328, 1992.
- [30] Max Petersen, Frank Wagner, Lars Hufnagel, Matthias Scheffler, Peter Blaha, and Karlheinz Schwarz. Improving the efficiency of FP-LAPW calculations. *Comput. Phys. Commun.*, 126:294, 2000.
- [31] K. H. J. Buschow. *Electronic and Magnetic Properties of Metals and Ceramics, Part I and II. (Materials Science and Technology: A Comprehensive Treatment, Volume 3A and 3B).* EWeinheim/New York : VCH, 1991.
- [32] J. Kubler and V. Eyert. *Electronic structure calculations in Materials Science and Technology. Vol. 3A.* EWeinheim/New York : VCH, 1992.
- [33] S. Blügel. *Density Functional Theory in Practice*, Institut für Festkörperforschung Forschungszentrum Jülich GmbH, A7.
- [34] P. Blaha, K. Schwarz, G. K. H. Madsen, D. Kvasnicka, and J. Luitz. *Wien2k, An Augmented Plane Wave plus Local orbital Program for Calculating the Crystal Properties.* <http://www.wien2k.at>, 2001.
- [35] S. Cottenier. *DFT and the Family of (L)APW-methods: a step-by-step introduction*, University of Ghent, Belgium, 2004.
- [36] A. H. MacDonald and S. H. Vosko. A relativistic density functional formalism. *J. Phys. C: Solid State Phys.*, 12:2977, 1979.
- [37] J. Korringa. On the calculation of the energy of a Bloch wave in a metal. *Physica*, 13:392, 1947.
- [38] W. Kohn and N. Rostoker. Solution of the Schrödinger Equation in Periodic Lattices with an Application to Metallic Lithium. *Phys. Rev.*, 94:1111, 1954.

- [39] T. H. Dupree. Electron scattering in a crystal lattice. *Ann. Phys.*, 15:63, 1961.
- [40] J. L. Beeby. The density of electrons in a perfect or imperfect lattice. *Proc. Roy. Soc. London Ser. A*, 302:113, 1967.
- [41] G. J. Morgan. Bloch waves and scattering by impurities. *Proc. Phys. Soc.*, 89:365, 1966.
- [42] N. Papanikolaou, R. Zeller, and P. H. Dederichs. Conceptual improvements of the KKR method. *J. Phys.: Condens. Matter*, 14:2799, 2002.
- [43] V. Popescu, H. Ebert, B. Nonas, and P. H. Dederichs. Spin and orbital magnetic moments of  $3d$  and  $4d$  impurities in and on the (001) surface of bcc Fe. *Phys. Rev. B*, 64:184407, 2001.
- [44] S. Lounis, P. Mavropoulos, P. H. Dederichs, and S. Blügel. Noncollinear Korringa-Kohn-Rostoker Green function method: Application to  $3d$  nanostructures on Ni(001). *Phys. Rev. B*, 72:224437, 2005.
- [45] R. Zeller, J. Deutz, and P. H. Dederichs. Application of complex energy integration to selfconsistent electronic structure calculations. *Solid State Commun.*, 44:993, 1982.
- [46] J. S. Faulkner. The modern theory of alloys. *Prog. Mater Sci.*, 27:1, 1982.
- [47] P. Weinberger. *Electron Scattering Theory for Ordered and Disordered Matter*, Oxford University Press, Oxford, 1990.
- [48] A. Gonis. *Green functions for ordered and disordered systems*, North-Holland, Amsterdam, 1992.
- [49] A. Gonis and W. H. Butler. *Multiple scattering in solids, Graduate Texts in Contemporary Physics*, Springer, Berlin, 1999. Springer, Berlin, 1999.
- [50] H. Ebert, H. Freyer, A. Vernes, and G.-Y. Guo. Manipulation of the spin-orbit coupling using the dirac equation for spin-dependent potentials. *Phys. Rev. B*, 53:7721, 1996.
- [51] O. Šipr, S. Bornemann, H. Ebert, and J. Minár. Magnetocrystalline anisotropy energy for adatoms and monolayers on non-magnetic substrates: where does it come from? *J. Phys.: Condens. Matter*, 26(19):196002, 2014.
- [52] A. Zunger, S.-H. Wei, L. G. Ferreira, and J. E. Bernard. Special quasirandom structures. *Phys. Rev. Lett.*, 65:353, 1990.
- [53] S.-H. Wei, L. G. Ferreira, J. E. Bernard, and A. Zunger. Electronic properties of random alloys: Special quasirandom structures. *Phys. Rev. B*, 42:9622, 1990.

- [54] P. Soven. Coherent-potential model of substitutional disordered alloys. *Phys. Rev.*, 156:809, 1967.
- [55] D. W. Taylor. Vibrational properties of imperfect crystals with large defect concentrations. *Phys. Rev.*, 156:1017, 1967.
- [56] T. Rauch, J. Henk S. Achilles, and I. Mertig. Spin Chirality Tuning and Topological Semimetals in Strained  $\text{HgTe}_x\text{S}_{1-x}$ . *Phys. Rev. Lett.*, 114:236805, 2015.
- [57] R. Masrour and E. K. Hlil. Correlation of electronic structure and magnetic moment in  $\text{Ga}_{1-x}\text{Mn}_x\text{N}$  : First-principles, mean field and high temperature series expansions calculations. *Physica A: Statistical Mechanics and its Applications*, 456:215, 2016.
- [58] H. Akai, P. H. Dederichs, and J. Kanamori. Magnetic properties of ni- and co-alloys calculated by kkr-cpa-bsd method. *J. Physique. Coll.*, 49:C8–23, 1988.
- [59] A. E. Kissavos, S. I. Simak, P. Olsson, L. Vitos, and I. A. Abrikosov. Total energy calculations for systems with magnetic and chemical disorder. *Comp. Mater. Science*, 35:1, 2006.
- [60] J. Kudrnovský, V. Drchal, I. Turek, and P. Weinberger. Electronic, magnetic, and transport properties and magnetic phase transition in quaternary (Cu,Ni)MnSb heusler alloys. *Phys. Rev. B*, 78:054441, 2008.
- [61] S. Lowitzer, D. Ködderitzsch, H. Ebert, and J. B. Staunton. Electronic transport in ferromagnetic alloys and the slater-pauling curve. *Phys. Rev. B*, 79:115109, 2009.
- [62] Y. Yin, F. Pan, M. Ahlberg, M. Ranjbar, P. Dürrenfeld, A. Houshang, M. Haidar, L. Bergqvist, Y. Zhai, R. K. Dumas, A. Delin, and J. Åkerman. Tunable permalloy-based films for magnonic devices. *Phys. Rev. B*, 92:024427, 2015.
- [63] J. Hu, J. Chen, and G. Ju. *L10 FePt for Magnetic Recording Media Application*, page 223. John Wiley and Sons, Inc., 2011.
- [64] K. R. Coffey, M. A. Parker, and J. K. Howard. High anisotropy  $L_{10}$  thin films for longitudinal recording. *IEEE Trans. Magn.*, 31:2737, 1995.
- [65] A. R. Mackintosh and O. K. Andersen. The electronic structure of transition metals, in electrons at the fermi surface. volume 3, Cambridge University Press, 1980.

- [66] T. Burkert, O. Eriksson, S. I. Simak, A. V. Ruban, B. Sanyal, L. Nordström, and J. M. Wills. Magnetic anisotropy of  $L1_0$  FePt and  $\text{Fe}_{1-x}\text{Mn}_x\text{Pt}$ . *Phys. Rev. B*, 71:134411, 2005.
- [67] K. Lejaeghere, V. Van Speybroeck, G. Van Oost, and S. Cottenier. Error estimates for solid-state density-functional theory predictions: an overview by means of the ground-state elemental crystals. *Rev. Solid State Mater. Sci.*, 39:1, 2014.
- [68] Comparing solid state DFT codes, basis sets and potentials. <http://molmod.ugent.be/deltacodesdft>, 2015.
- [69] K. Lejaeghere, G. Bihlmayer, T. Björkman, P. Blaha, S. Blügel, V. Blum, D. Caliste, I. E. Castelli, S. J. Clark, A. Dal Corso, S. de Gironcoli, T. Deutsch, J. K. Dewhurst, I. Di Marco, C. Draxl, M. Duak, O. Eriksson, J. A. Flores-Livas, K. F. Garrity, L. Genovese, P. Giannozzi, M. Giantomassi, S. Goedecker, X. Gonze, O. Grånäs, E. K. U. Gross, A. Gulans, F. Gygi, D. R. Hamann, P. J. Hasnip, N. A. W. Holzwarth, D. Iuan, D. B. Jochym, F. Jollet, D. Jones, G. Kresse, K. Koepf, E. Küçükbenli, Y. O. Kvashnin, I. L. M. Locht, S. Lubeck, M. Marsman, N. Marzari, U. Nitzsche, L. Nordström, T. Ozaki, L. Paulatto, C. J. Pickard, W. Poelmans, M. I. J. Probert, K. Refson, M. Richter, G.-M. Rignanese, S. Saha, M. Scheffler, M. Schlipf, K. Schwarz, S. Sharma, F. Tavazza, P. Thunström, A. Tkatchenko, M. Torrent, D. Vanderbilt, M. J. van Setten, V. Van Speybroeck, J. M. Wills, J. R. Yates, G.-X. Zhang, and S. Cottenier. The kohn-sham equation of state for elemental solids: a solved problem. *Science*, 351:aad3000, 2016.
- [70] M. Asato, A. Settels, T. Hoshino, T. Asada, S. Blügel, R. Zeller, and P. H. Dederichs. Full-potential kkr calculations for metals and semiconductors. *Phys. Rev. B*, 60:5202, 1999.
- [71] J. G. Gay and R. Richter. Spin anisotropy of ferromagnetic films. *Phys. Rev. Lett.*, 56:2728, 1986.
- [72] P. Ravindran, A. Kjekshus, H. Fjellvåg, P. James, L. Nordström, B. Johansson, and O. Eriksson. Large magnetocrystalline anisotropy in bilayer transition metal phases from first-principles full-potential calculations. *Phys. Rev. B*, 63:144409, 2001.
- [73] H. J. F. Jansen, G. S. Schneider, and H. Y. Wang. Calculation of magnetocrystalline anisotropy in transition metals. In D. J. Singh and D. A. Papaconstantopoulos, editors, *Electronic Structure and Magnetism of Complex Materials*, page 57. Springer, Berlin, 2003.

- [74] O. Šipr, S. Bornemann, J. Minár, and H. Ebert. Magnetic anisotropy of Fe and Co adatoms and monolayers: Need for a proper treatment of the substrate. *Phys. Rev. B*, 82:174414, 2010.
- [75] G. H. O. Daalderop, P. J. Kelly, and M. F. H. Schuurmans. Magnetocrystalline anisotropy and orbital moments in transition-metal compounds. *Phys. Rev. B*, 44:12054, 1991.
- [76] A. Sakuma. First principle calculation of the magnetocrystalline anisotropy energy of FePt and CoPt ordered alloys. *J. Phys. Soc.*, 63:3053, 1994.
- [77] I. V. Solovyev, P. H. Dederichs, and I. Mertig. Origin of orbital magnetization and magnetocrystalline anisotropy in TX ordered alloys (where T=Fe, Co and X=Pt, Pd). *Phys. Rev. B*, 52:13419, 1995.
- [78] P. M. Oppeneer. Magneto-optical spectroscopy in the valence-band energy regime: relationship to the magnetocrystalline anisotropy1. *J. Magn. Magn. Mater*, 188:275, 1998.
- [79] I. Galanakis, M. Alouani, and H. Dreysse. Perpendicular magnetic anisotropy of binary alloys: A total-energy calculation. *Phys. Rev. B*, 62:6475, 2000.
- [80] A. B. Shick and O. N. Mryasov. Coulomb correlations and magnetic anisotropy in ordered  $L1_0$  CoPt and FePt alloys. *Phys. Rev. B*, 67:172407, 2003.
- [81] S. Ostanin, S. A. Razee, J. B. Staunton, B. Ginatempo, and E. Bruno. Magnetocrystalline anisotropy and compositional order in  $Fe_{0.5}Pt_{0.5}$ : Calculations from an ab initio electronic model. *J. Appl. Phys*, 93:453, 2003.
- [82] T. Kosugi, T. Miyake, and S. Ishibashi. Second-order perturbation formula for magnetocrystalline anisotropy using orbital angular momentum matrix. *J. Phys. Soc. Jpn.*, 83:044707, 2014.
- [83] O. A. Ivanov, L. V. Solina, V. A. Demshira, and L. M. Magat. *Phys. Met. Metallogr.*, 35:92, 1973.
- [84] H. Ebert, D. Ködderitzsch, and J. Minár. Calculating condensed matter properties using the kkr-green's function method recent developments and applications. *Rep. Prog. Phys.*, 74:096501, 2011.
- [85] H. Ebert. *The Munich SPR-KKR package, version 7*. <http://olymp.cup.uni-muenchen.de>, 2012.
- [86] O. N. Mryasov, U. Nowak, K. Y. Guslienko, and R. W. Chantrell. Temperature-dependent magnetic properties of FePt: Effective spin hamiltonian model. *Europhys. Lett.*, 69:805, 2005.



- [87] J. B. Staunton, S. Ostanin, S. S. A. Razee, B. Gyorffy, L. Szunyogh, B. Ginatempo, and E. Bruno. Long-range chemical order effects upon the magnetic anisotropy of FePt alloys from an ab initio electronic structure theory. *J. Phys. C: Solid State Phys.*, 16:5623, 2004.
- [88] O. Hovorka, S. Devos, Q. Coopman, W. J. Fan, C. J. Aas, R. F. L. Evans, X. Chen, G. Ju, and R. W. Chantrell. The curie temperature distribution of FePt granular magnetic recording media. *Appl. Phys. Lett.*, 101:052406, 2012.
- [89] P. V. Lukashev, N. Horrell, and R. F. Sabirianov. Tailoring magnetocrystalline anisotropy of FePt by external strain. *J. Appl. Phys.*, 111:07A318, 2012.
- [90] R. Cuadrado, Timothy J. Klemmer, and R. W. Chantrell. Magnetic anisotropy of  $Fe_{1-y}X_yPt-L1_0$  [X=Cr, Mn, Co, Ni, Cu] bulk alloys. *Appl. Phys. Lett.*, 105:152406, 2014.
- [91] M. H. F. Sluiter, C. Colinet, and A. Pasturel. *Ab initio* calculation of the phase stability in Au-Pd and Ag-Pt alloys. *Phys. Rev. B*, 73:174204, 2006.
- [92] Z. Su, Y. Wang, S. Wang. Structural, vibrational, and thermodynamic properties of ordered and disordered  $Ni_{1-x}Pt_x$  alloys from first-principles calculations. *Acta Metallurgica Sinica*, 46:623, 2010.
- [93] R. Hayn and V. Drchal. Invar behavior of disordered fcc –  $Fe_xPt_{1-x}$  alloys. *Phys. Rev. B*, 58:4341, 1998.
- [94] S. L. Shang, Y. Wang, D. E. Kim, C. L. Zacherl, Y. Du, and Z. K. Liu. Structural, vibrational, and thermodynamic properties of ordered and disordered  $Ni_{1-x}Pt_x$  alloys from first-principles calculations. *Phys. Rev. B*, 83:144204, 2011.
- [95] Y. Perlov, H. Ebert, A. N. Yaresko, V. N. Antonov, and D. Weller. Influence of disorder on the magneto-optical properties of FePt. *Solid State Commun.*, 105:273, 1998.
- [96] M. Kharoubi, A. Haroun, and M. Alouani. Origin of the polar Kerr rotation in ordered and disordered FePt multilayers. *Comput. Mater. Sci*, 73:24, 2013.
- [97] D. Paudyal, T. Saha-Dasgupta, and A. Mookerjee. Magnetic properties of X-Pt (X = Fe,Co,Ni) alloy systems. *J. Phys.: Condens. Matter*, 16:2317, 2004.
- [98] C. J. Sun, G. M. Chow, G. H. Fecher, J. S. Chen, H.-J. Lin, and Y. Hwu. Spin and Orbital Magnetic Moments of FePt Thin Films. *Jpn. J. Appl. Phys.*, 45:2539, 2006.

- [99] J. Kuneš, P. Novák, R. Schmid, P. Blaha, and K. Schwarz. Electronic structure of fcc th: Spin-orbit calculation with  $6p_{1/2}$  local orbital extension. *Phys. Rev. B*, 64:153102, 2001.
- [100] P. Pyykko and J. P. Desclaux. Relativity and the periodic system of elements. *Acc. Chem. Res.*, 12:276, 1979.
- [101] R. Zeller. Projection potentials and angular momentum convergence of total energies in the full-potential koringakohnrostoker method. *J. Phys.: Condens. Matter*, 25:105505, 2013.
- [102] A. Alam, S. N. Khan, A. Smirnov, D. M. Nicholson, and D. D. Johnson. Green's function multiple-scattering theory with a truncated basis set: An augmented-kr formalism. *Phys. Rev. B*, 90:205102, 2014.
- [103] A. Alam, B. G. Wilson, and D. D. Johnson. Accurate and fast numerical solution of poisson's equation for arbitrary, space-filling voronoi polyhedra: Near-field corrections revisited. *Phys. Rev. B*, 84:205106, 2011.
- [104] R Kovačik and R Zeller. private communication.
- [105] M. Ogura, C. Zecha, M. Offenberger, H. Ebert, and H. Akai. Near-field correction in the first-principles calculations by the exact two-center expansion for the inverse of the distance. *J. Phys.: Condens. Matter*, 27:485201, 2015.
- [106] A. Alam, S. N. Khan, B. G. Wilson, and D. D. Johnson. Efficient isoparametric integration over arbitrary space-filling voronoi polyhedra for electronic structure calculations. *Phys. Rev. B*, 84:045105, 2011.
- [107] R. Zeller. The koringakohnrostoker method with projection potentials: exact result for the density. *J. Phys.: Condens. Matter*, 27:306301, 2015.
- [108] X. Wang, D-S. Wang, R. Wu, and A. J. Freeman. Validity of the force theorem for magnetocrystalline anisotropy. *J. Magn. Magn. Materials*, 159:337, 1996.
- [109] X. Wang, R. Wu, D-S. Wang, and A. J. Freeman. Torque method for the theoretical determination of magnetocrystalline anisotropy. *Phys. Rev. B*, 54:61, 1996.
- [110] K. Nakamura, R. Shimabukuro, Y. Fujiwara, T. Akiyama, T. Ito, and A. J. Freeman. Giant modification of the magnetocrystalline anisotropy in transition-metal monolayers by an external electric field. *Phys. Rev. Lett.*, 102:187201, 2009.

- [111] D. Li, A. Smogunov, C. Barreteau, F. Ducastelle, and D. Spanjaard. Magnetocrystalline anisotropy energy of Fe(001) and Fe(110) slabs and nanoclusters: A detailed local analysis within a tight-binding model. *Phys. Rev. B*, 88:214413, 2013.
- [112] P. Błóński and J. Hafner. Density-functional theory of the magnetic anisotropy of nanostructures: an assessment of different approximations. *J. Phys.: Condens. Matter*, 21:426001, 2009.
- [113] P. Błóński, A. Lehnert, S. Dennler, S. Rusponi, M. Etzkorn, G. Moulas, P. Benck, P. Gambardella, H. Brune, and J. Hafner. Magnetocrystalline anisotropy energy of Co and Fe adatoms on the (111) surfaces of Pd and Rh. *Phys. Rev. B*, 81:104426, 2010.
- [114] P. Bruno. Tight-binding approach to the orbital magnetic moment and magnetocrystalline anisotropy of transition-metal monolayers. *Phys. Rev. B*, 39:865, 1989.
- [115] G. van der Laan. Microscopic origin of magnetocrystalline anisotropy in transition metal thin films. *J. Phys.: Condens. Matter*, 10:3239, 1998.
- [116] F. Gimbert and L. Calmels. First-principles investigation of the magnetic anisotropy and magnetic properties of Co/Ni(111) superlattices. *Phys. Rev. B*, 86:184407, 2012.
- [117] S. Assa Aravindh, S. Mathi Jaya, M. C. Valsakumar, and C. S. Sundar. Compositional variation of magnetic moment, magnetic anisotropy energy and coercivity in  $Fe_{(1-x)}M_x$  ( $M = Co/Ni$ ) nanowires: an ab initio study. *Appl. Nanosci.*, 2:409, 2012.
- [118] Y. Miura, S. Ozaki, Y. Kuwahara, M. Tsujikawa, K. Abe, and M. Shirai. The origin of perpendicular magneto-crystalline anisotropy in L1<sub>0</sub>-FeNi under tetragonal distortion. *J. Phys.: Condens. Matter*, 25:106005, 2013.
- [119] M. Kotsugi, M. Mizuguchi, S. Sekiya, M. Mizumaki, T. Kojima, T. Nakamura, H. Osawa, K. Kodama, T. Ohtsuki, T. Ohkochi, K. Takanashi, and Y. Watanabe. Origin of strong magnetic anisotropy in L1<sub>0</sub>-FeNi probed by angular-dependent magnetic circular dichroism. *J. Magn. Magn. Materials*, 326:235, 2013.
- [120] T. Ueno, J. Sinha, N. Inami, Y. Takeichi, S. Mitani, K. Ono, and M. Hayashi. Enhanced orbital magnetic moments in magnetic heterostructures with interface perpendicular magnetic anisotropy. *Sci. Reports*, 5:14858, 2015.

- [121] C. Andersson, B. Sanyal, and L. Nordström O. Eriksson, O. Karis, D. Arvanitis, T. Konishi, E. Holub-Krappe, and J. Hunter Dunn. Influence of ligand states on the relationship between orbital moment and magnetocrystalline anisotropy. *Phys. Rev. Lett.*, 99:177207, 2007.
- [122] Y. Kota and A. Sakuma. Relationship between magnetocrystalline anisotropy and orbital magnetic moment in L1<sub>0</sub>-type ordered and disordered alloys. *J. Phys. Soc.*, 81:084705, 2012.
- [123] J. W. Davenport, R. E. Watson, and M. Weinert. Linear augmented-slater-type-orbital method for electronic-structure calculations. v. spin-orbit splitting in Cu<sub>3</sub>Au. *Phys. Rev. B*, 37:9985, 1988.
- [124] O. Šipr, J. Minár, S. Mankovsky, and H. Ebert. Influence of composition, many-body effects, spin-orbit coupling, and disorder on magnetism of Co-Pt solid-state systems. *Phys. Rev. B*, 78:144403, 2008.
- [125] G. Autès, C. Barreteau, D. Spanjaard, and M-C. Desjonquères. Magnetism of iron: from the bulk to the monatomic wire. *J. Phys.: Condens. Matter*, 18:6785, 2006.
- [126] O. Šipr, S. Mankovsky, S. Polesya, S. Bornemann, J. Minár, and H. Ebert. Illustrative view on the magnetocrystalline anisotropy of adatoms and monolayers. *Phys. Rev. B*, 93:174409, 2016.
- [127] J. P. Perdew, K. Burke, and M. Ernzerhof. Generalized gradient approximation made simple. *Phys. Rev. Lett*, 77:3865, 1996.
- [128] M. S. S. Brooks. Calculated ground state properties of light actinide metals and their compounds. *Physica B+C*, 130:6, 1985.
- [129] O. Eriksson, B. Johansson, R. C. Albers, A. M. Boring, and M. S. S. Brooks. Orbital magnetism in Fe, Co, and Ni. *Phys. Rev. B*, 42:2707, 1990.
- [130] O. Hjortstam, J. Trygg, J. M. Wills, B. Johansson, and O. Eriksson. Calculated spin and orbital moments in the surfaces of the 3d metals Fe, Co, and Ni and their overlayers on Cu(001). *Phys. Rev. B*, 53:9204, 1996.
- [131] Z. W. Lu, S.-H. Wei, and A. Zunger. Electronic structure of random Ag<sub>0.5</sub>Pd<sub>0.5</sub> and Ag<sub>0.5</sub>Au<sub>0.5</sub> alloys. *Phys. Rev. B*, 44:10470, 1991.
- [132] O. Šipr, J. Minár, S. Mankovsky, and H. Ebert. Influence of composition, many-body effects, spin-orbit coupling, and disorder on magnetism of co-pt solid-state systems. *Phys. Rev. B*, 78:144403, 2008.

- [133] A. V. Ruban and H. L. Skriver. Screened coulomb interactions in metallic alloys. I. universal screening in the atomic-sphere approximation. *Phys. Rev. B*, 66:024201, 2002.
- [134] A. V. Ruban, S. I. Simak, S. Shallcross, and H. L. Skriver. Local lattice relaxations in random metallic alloys: Effective tetrahedron model and supercell approach. *Phys. Rev. B*, 67:214302, 2003.
- [135] T. Marten, W. Olovsson, S. I. Simak, and I. A. Abrikosov. *Ab initio* study of disorder broadening of core photoemission spectra in random Cu – Pd and Ag – Pd alloys. *Phys. Rev. B*, 72:054210, 2005.
- [136] J. L. Cambell and T. Papp. Widths of the atomic K-N7 levels. *Atomic Data and Nuclear Data Tables*, 77:1, 2001.
- [137] C. S. Fadley, S. B. M. Hagstrom, M. P. Klein, and D. A. Shirley. Chemical effects on core electron binding energies in iodine and europium. *J. Chem. Phys.*, 48:3779, 1968.
- [138] U. Gelius. Binding energies and chemical shifts in esca. *Phys. Scripta*, 9:133, 1974.
- [139] R. J. Cole, N. J. Brooks, and P. Weightman. Madelung potentials and disorder broadening of core photoemission spectra in random alloys. *Phys. Rev. Lett.*, 78:3777, 1997.
- [140] R. J. Cole and P. Weightman. Disorder broadening of core levels: Insights into alloy electronic structure. *J. Electron. Spectrosc. Relat. Phenom.*, 178:112, 2010.

# Appendix B

## Curriculum vitae

**SALEEM AYAZ KHAN**

Date Of Birth: April 12th 1982

Email: sayaz\_usb@yahoo.com



---

### PRESENT ADDRESS

New Technologies - Research Center,  
University of West Bohemia,  
Univerzitni 8, 306 14 Pilsen,  
Czech Republic,  
(+420) 777083956

### PERMANENT ADDRESS

Village and post office Bachai,  
District Swabi, 23430, Tehsil  
Razar, Khyber Pakhtunkhwa,  
Pakistan,  
(+92) 3459454721

### RESEARCH AREA

Ab initio calculations of electronic structure, optical and thermoelectric properties of technologically interesting materials.

### CURRENT RESEARCH INTEREST

- Magneto-crystalline anisotropy (MCA) of bulk FePt: effect of spin orbit coupling.
- Magnetic properties of  $\text{Fe}_{0.5}\text{Pt}_{0.5}$  substitutional alloys: local environment effect.
- Study of Fe embedded surface layer of Pt(111) in order to explain

the experimental data.

- Ab initio x-ray absorption spectroscopy of B doped Si(111) in order to study interesting experimental data.

## EDUCATION

2011	M.Phil.	Hazara University
2008	M.Sc.	University of Malakand
2003	B.Sc.	University of Peshawar
2000	F.Sc.	BISE Peshawar
1998	S.S.C.	BISE Peshawar

Master in Philosophy thesis title (M. Phil):

Critical radii of cubic perovskites: A theoretical study.

## EXPERIENCE

Teaching; Teaching experience in different graduate and undergraduate institutes during 2007-2011.

## PROFICIENCIES

- Wien2k code
- BoltzTraP Code
- Elastic Code
- Gibbs Code
- SPRKKR Code
- Quantum espresso

SUBJECTS STUDIED (in M.phil and Master):

Quantum mechanics, Mathematical method of physics, Classical mechanics, Statistical mechanics, Plasma physics, Optical properties, Solid state,

Quantum optics, Modern physics, Electro dynamics, Magnetism, Electronics, Nuclear physics, Electro magnetic theory.

#### RESEARCH STAYS:

- Autumn School on dynamical mean field approach with predictive power for strongly correlated Electrons FZ, Jülich, Germany, 2014.
- Short term scientific visit (15 days) to Institute of Materials Chemistry, TU Vienna, Austria “Collaboration with Prof. Peter Blaha on advance properties of WIEN2K for FePt bulk and nanostructures”, 2015.
- Hands-on course Introduction to the application of ab-initio methods in spectroscopy, New Technologies Research Centre, University of West Bohemia Czech Republic, 2015.
- Short term scientific visit (10 days) to Institute of Materials Chemistry, TU Vienna, Austria, “Collaboration with Prof. Peter Blaha on Fe/Pt(111) low dimensional nanostructures”, 2016.
- Winter school on the fundamentals and applications of ab-initio methods in spectroscopy, Applied Physics Faculty of the University of Nova Gorica, Ajdovščina, Slovenia, 2016.



# Appendix C

## List of publications

Saleem Ayaz Khan

Publications: 40

Citations 141

h-index 7

website: [https://www.researchgate.net/profile/Saleem\\_Khan11](https://www.researchgate.net/profile/Saleem_Khan11)

### Publications in 2013

1. S. A. Khan, A. H. Reshak: *First Principle Study of Electronic Structure, Chemical Bonding and Optical Properties of 5-azido-1H-tetrazole*. Int. J. Electrochem. Sci., 8 (2013) 9459.
2. A. H. Reshak, S. A. Khan: *Density of electronic states and dispersion of optical functions of defect chalcopyrite  $CdGa_2X_4$  ( $X = S, Se$ ): DFT study*. Mater. Res. Bull. 48 (2013) 4555.
3. A. H. Reshak, S. A. Khan: *Electronic structure and optical properties of  $In_2X_2O_7$  ( $X = Si, Ge, Sn$ ) from direct to indirect gap: An ab initio study*. Comput. Mater. Sci. 78 (2013) 91.

**Publications in 2014**

1. A. H. Reshak, S. A. Khan: *NaAuS chicken-wire-like semiconductor: Electronic structure and optical properties*. J. Alloys Compd. 582 (2014) 6.
2. A. H. Reshak, S. A. Khan: *Thermoelectric properties, electronic structure and optoelectronic properties of anisotropic  $Ba_2Tl_2CuO_6$  single crystal from DFT approach*. J. Magn. Magn. Mater. 354 (2014) 216.
3. A. H. Reshak, S. A. Khan: *Dispersion of the second harmonic generation from  $CdGa_2X_4$  ( $X = S, Se$ ) defect chalcopyrite: DFT calculations*. J. Alloys. Compd. 595 (2014) 125.
4. A. H. Reshak, S. A. Khan: *Electronic band structure and specific features of AA- and AB-stacking of carbon nitride ( $C_3N_4$ ): DFT calculation*. RSC Advances, 4 (2014) 6957.
5. S. A. Khan, A. H. Reshak, Z. A. Alahmed: *Electronic band structure and optoelectronic properties of  $SrCu_2X_2$  ( $X = As, Sb$ ): DFT calculation*. J. Mater. Sci. 49 (2014) 5208.
6. S. A. Khan, A.H. Reshak: *Optoelectronic and transport properties of Zintl phase  $KBa_2Cd_2Sb_3$  compound*. Comput. Mater. Sci. 95 (2014) 328.
7. A. H. Reshak, S. A. Khan: *Thermoelectric properties of a single graphene sheet and its derivatives*. J. Mater. Chem. C, 2 (2014) 2346.
8. A. H. Reshak, S. A. Khan: *Linear and nonlinear optical properties for AA and AB stacking of carbon nitride polymorph ( $C_3N_4$ )*. RSC Adv. 4 (2014), 11967.
9. A. H. Reshak, S. A. Khan, *Investigation of electronic structure and optical properties of  $MgAl_2O_4$ : DFT approach*. Opt. Mater. 37 (2014) 322.
10. H. Ud Din, S. Azam S. A. Khan, R. Khenata: *Optoelectronic behavior of Quaternary Uranium Chalcogenides  $Rb_2Pd_3UM_6$  ( $M = S, Se$ ): A first principle*

- study*. J. Alloys Compd. 615 (2014) 507.
11. A. H. Reshak, Y. Al-Douri, R. Khenata, W. Khan, S. A. Khan, S. Azam: *Electronic structure, Fermi surface topology and spectroscopic optical properties of LaBaCo<sub>2</sub>O<sub>5.5</sub> compound*. J. Magn. Mater. 363(2014) 133.
  12. S. Azam, S. A. Khan, F. A. Shah, S. Muhammad, H. Ud Din, R. Khenata: *Electronic, optical and thermoelectric properties of Ce<sub>3</sub>PdIn<sub>11</sub> and Ce<sub>5</sub>Pd<sub>2</sub>In<sub>19</sub>: An ab initio study*. Intermetallics 55 (2014) 184.

### Publications in 2015

1. S. A. Khan, A. H. Reshak: *Linear, nonlinear optical susceptibilities, hyperpolarizability, and space electronic charge density of meso silver(I) histidinate [Ag(D-his)]<sub>n</sub> (Hhis = histidine)*. Polyhedron 85 (2015) 962.
2. A. H. Reshak, S. A. Khan: *First principle investigation of electronic structure and optical behaviors of 2-amino-4-fluorododec-4-encarboic acid*. Mater. Sci. Semicond. Process. 31 (2015) 302.
3. M. Ullah, S. A. Khan, G. Murtaza, R. Khenata, N. Ullah, S. Bin Omran: *Electronic, thermoelectric and magnetic properties of La<sub>2</sub>NiMnO<sub>6</sub> and La<sub>2</sub>CoMnO<sub>6</sub>*. J. Magn. Mater. 377(2015)197.
4. S. A. Khan, S. Azam: *First principle investigation of electronic structure, chemical bonding and optical properties of tetrabarium gallium trinitride oxide single crystal*. Mater. Res. Bull. 70 (2015) 436.
5. S. A. Khan, S. Azam, F. A. Shah, B. Amin: *Electronic structure and optical properties of CdO from bulk to nanosheet: DFT approach*. Opt. Mater. 47 (2015) 372.

6. S. Azam, S. A. Khan, S. Goumri-Said: *Exploring the electronic structure and optical properties of the quaternary selenide compound,  $Ba_4Ga_4SnSe_{12}$ : For photovoltaic applications.* J. Solid State Chem. 229 (2015) 260.
7. A. Bendjedid, T. Seddik, R. Khenata, H. Baltache, G. Murtaza, A. Bouhemadou, S. Bin Omran, S. Azam, S. A. Khan: *GGA+U study on phase transition, optoelectronic and magnetic properties of  $AmO_2$  with spin-orbit coupling.* J. Magn. Magn. Mater. 396 (2015) 190.
8. S. Azam, S. A. Khan, R. Khenata, G. Murtaza, S. Bin Omran, S. Muhammad: *Optoelectronic and Magnetic Properties of  $Eu_2Si_5N_8$ : An Ab-initio Study.* Zeitschrift für Naturforschung A, 70 (2015) 187.
9. S. Azam, S. A. Khan, S. Goumri-Said: *Engle-Vosko GGA Approach Within DFT Investigations of the Optoelectronic Structure of the Metal Chalcogenide Semiconductor  $CsAgGa_2Se_4$ .* J. Electron. Mater. 45 (2015) 1.
10. S. Azam, S. A. Khan, S. Goumri-Said: *Modified Becke-Johnson (mBJ) exchange potential investigations of the optoelectronic structure of the quaternary diamond-like semiconductors  $Li_2CdGeS_4$  and  $Li_2CdSnS_4$ .* Mater. Sci. Semicond. Process. 39 (2015) 606.
11. S. Azam, S. A. Khan, W. Khan, S. Muhammad, H. Udin, G. Murtaza, R. Khenata, F. A. Shah, J. Minar, W. K. Ahmed: *Detailed DFT studies of the electronic structure and optical properties of  $KBaMSe_3$  ( $M = As, Sb$ ).* J. Alloys Compd. 644 (2015) 91.
12. S. Azam, S. A. Khan, J. Minar, S. Goumri-Said: *Exploring the electronic structure and optical properties of new inorganic luminescent materials  $Ba(Si, Al)_5(O, N)_8$  compounds for light-emitting diodes devices.* Curr. Appl. Phys. 15 (2015) 1160.

13. S. Azam, S. A. Khan, S. Goumri-Said: *Revealing the optoelectronic and thermoelectric properties of the Zintl quaternary Arsenides  $ACdGeAs_2$  ( $A = K, Rb$ )*. Mater. Res. Bull. 70 (2015) 847.
14. S. Azam, S. A. Khan: *A first principles study of electronic and optical properties of the polar quaternary chalcogenides  $\beta-A_2Hg_3Ge_2S_8$  ( $A = K$  and  $Rb$ )*. Mater. Sci. Semicond. Process. 34 (2015) 250.
15. F. A. Shah, S. A. Khan, S. Arif, S. Azam, R. Khenata, S. Bin-Omran: *Theoretical investigation of electronic structure and optical response and their interrelation with the transport properties of  $Ga_{1-x}In_xN$  ( $x = 0, 0.25, 0.50, 0.75$ )*. Curr. Appl. Phys. 15 (2015) 608.
16. S. Azam, S. A. Khan, J. Minar, W. Khan, H. Ud Din, R. Khenata, G. Murtaza, S. Bin-Omran, S. Goumri-Said: *Coulomb interaction and Spin-orbit coupling calculations of thermoelectric properties of the quaternary chalcogenides  $Tl_2PbXY_4$  ( $X = Zr, Hf$  and  $Y = S, Se$ )*. Semicond. Sci. Technol. 30 (2015) 105018.

### Publications in 2016

1. M. Faizan, G. Murtaza, S. Azam, S. A. Khan, A. Mahmood, A. Yar: *Elastic and optoelectronic properties of novel  $Ag_3AuSe_2$  and  $Ag_3AuTe_2$  semiconductors*. Mater. Sci. Semicond. Process. 52 (2016) 8.
2. S. Azam, S. A. Khan, H. Ud Din, R. Khenata, S. Goumri-Said: *Exploring the thermoelectric and magnetic properties of uranium selenides:  $Tl_2Ag_2USE_4$  and  $Tl_3Cu_4USE_6$* . J. Magn. Magn. Mater. 413 (2016) 57.
3. S. Azam, S. A. Khan, S. Goumri-Said: *DFT combined to Boltzmann transport theory for optoelectronic and thermoelectric properties investigations for monoclinic metallic selenide:  $Cu_5Sn_2Se_7$* . Optik 127 (2016) 5472.

4. A. Basit, S. A. Khan, G. Murtaza, A. Mehmood, R. Khenata, S. Bin Omran, M. Yaseen: *Electronic, optical and thermoelectric properties of  $XNMg_3$  ( $X = P, As, Sb, Bi$ ) compounds*. Mater. Sci. Semicond. Process. 43 (2016) 69.
5. S. A. Khan, S. Azam, O. Šipr: *Interrelationship between structural, optical and transport properties of  $InP_{1-x}Bi_x$ : DFT approach*. Mater. Sci. Semicond. Process. 41 (2016) 45.
6. K. C. Bhamu, R. Khenanta, S. A. Khan, M. Singh, K. R. Priolkar: *Electronic, Optical and Thermoelectric Properties of  $2H - CuAlO_2$ : A First Principles Study*. J. Electron. Mater. 45 (2016) 615.
7. S. A. Khan, P. Blaha, H. Ebert, J. Minár, O. Šipr: *Magnetocrystalline anisotropy of  $FePt$ : a detailed view*. <http://arxiv.org/abs/1604.00176>.
8. S. A. Khan, P. Blaha, H. Ebert, J. Minár, O. Šipr: *Local environment effects in magnetic properties and electronic structure of disordered  $FePt$* . In preparation.
9. S. A. Khan, M. Vondráček, P. Blaha, K. Horáková, O. Šipr, V. Cháb: *Local geometry around B atoms in  $B/Si(111)$  from polarized x-ray absorption spectroscopy*. In preparation.